Characterization and modeling of the mechanical properties of wound oxide ceramic composites

Zur Erlangung des akademischen Grades
Doktor der Ingenieurwissenschaften
der Fakultät für Maschinenbau
des Karlsruher Institut für Technologie (KIT)

genehmigte Dissertation

von
Dipl.-Ing. Yuan Shi
aus Yunnan, China

Datum der Einreichung: 24.02.2017
Hauptreferent: Herr Prof. Dr. Dietmar Koch
Korreferent: Herr Prof. Dr. Hans Jürgen Seifert
Tag der mündlichen Prüfung: 12.05.2017

Vorwort

Die vorliegende Arbeit entstand im Rahmen meiner Tätigkeit als wissenschaftlicher Mitarbeiter am Institut für Bauweisen und Strukturtechnologie am Deutschen Zentrum für Luft- und Raumfahrt e.V. (DLR).

An erster Stelle danke ich meinem Doktorvater und Betreuer Prof. Dietmar Koch für die Bereitstellung des Themas, das entgegengebrachte Vertrauen und die Übernahme des Hauptreferats.

Ich möchte weiterhin Prof. Hans Jürgen Seifert vom Karlsruher Institut für Technologie (KIT) für die Übernahme des Korreferats danken.

Mein Dank geht an Prof. Heinz Voggenreiter und Prof. Dietmar Koch, die diese Arbeit ermöglicht haben.

Weiter möchte ich mich bei allen Mitarbeitern des Instituts für Bauweisen und Strukturtechnologie und besonders bei den Kollegen der Abteilung Keramische Verbundstrukturen für die Diskussionen und die Unterstützung der Arbeit bedanken. Besonderer Dank gilt hierbei Dr. Severin Hofmann und Neraj Jain für den wissenschaftlichen Diskurs und die wertvollen Hinweise während der Zeit meiner Arbeit.

Bei Prof. Dietmar Koch möchte ich mich darüber hinaus bedanken, der mich durch zahlreiche Diskussionen stets unterstützt, inspiriert und gefordert hat.

Mein Dank gilt weiterhin Dr. Stefan Hackemann für die Bereitstellung des Probenmaterials und Herrn Raouf Jemmali für die Computer Tomographie Messungen der Proben sowie Herrn Matthias Scheiffele für die Bearbeitung der Proben.

Ich danke weiterhin den Studenten Ayan Haldar, Harish Kalyan Ram Pothukuchi, Florian Jäckel und Marwa Oueslati für ihre Beiträge zu dieser Arbeit.

Abschließend gilt meine tiefe Dankbarkeit meiner Frau und meiner Familie für die emotionale und uneingeschränkte Unterstützung, die mir jederzeit als Antrieb und Haltepunkt diente.

Stuttgart, im Februar 2017

Yuan Shi

Abstract

In the present work, an oxide/oxide Ceramic Matrix Composite WHIPOX™ (Wound Highly Porous Oxide Ceramic) that was manufactured via the filament winding technique was investigated. The aim of the work was the characterization and modeling of the mechanical properties of wound oxide ceramic composites with varied fiber orientations. For this purpose, the characteristics of a virtual equivalent unidirectional layer (UD-layer) were calculated and applied through the Inverse Laminate Theory and modified Tsai-Wu failure criterion.

All modeling approaches developed in this study are dependent on experimental determination and microstructure analysis. The mechanical properties of the investigated material in different wound orientations, including initial stiffness, strength, strain, elastic and inelastic behavior, were completely evaluated with in-plane experimental tests at room temperature. Based on the microstructural analysis through Micro Computed Tomography, the modeling of the properties of WHIPOX™ was divided into two classes: WHIPOX™ with matrix cracks (WC) and WHIPOX™ without matrix cracks (NC).

Due to the lack of the required matrix and fiber properties within the composite and by the unavailable representative characteristics of CMC UD-materials, the traditional modeling methods and classic failure criterion cannot be directly adapted to describe the material behavior of wound CMCs. Therefore, advanced modeling approaches with virtual equivalent UD-layer properties are created for the evaluation and prediction of the material properties of the investigated material WHIPOX™. As the core component of the modeling chain, complete material properties of the equivalent UD-layer were calculated and evaluated: elastic properties through the Inverse Laminate Theory; strength properties by fitting different test results to modified Tsai-Wu criterion; failure strain using the inelastic deformation behavior factor Δ. All the values are discussed and calculated with consideration given to different microstructures with or without matrix cracks. Through the stacking of these equivalent UD-layers with any desired fiber orientation, e.g. non-orthogonal, orthogonal and asymmetrical (off-axis), an equivalent layered composite is created and its material constants can be predicted by using the modified stiffness matrix.

In order to predict the mechanical properties with more accuracy, particular features of the investigated materials have to be taken into consideration. For the investigated composite WHIPOX™, four distinctive features are implemented in the modeling approaches: identification of inhomogeneity of the investigated plate; interaction between failure strength and strain through inelastic deformation; division of material modeling groups based on the analysis of microstructure; update of analytical model of different batches with inhomogeneities created due to the manufacturing process.

Based on the good correlation between the experiments and the modeling results, it can be shown that modeling approaches factoring in the above mentioned particular material features allow a very accurate prediction of the in-plane mechanical properties for CMC laminates. The present work has identified a general modus operandi going from experimental determination and microstructure analysis to the prediction of the mechanical behavior of wound CMCs with varied fiber orientations. The results of this work are of great value for the future design and development of this class of composites. In this way the application of CMC-components in new fields like aerospace and civil engineering may be enhanced.

Kurzfassung

In der vorliegenden Arbeit wurde ein durch Wickeltechnik hergestellter, Oxid/Oxid-Keramikverbundwerkstoff (Ceramic Matrix Composite-CMC) mit poröser Matrix (WHIPOX™) untersucht. Ziel der Arbeit war die Charakterisierung und Modellierung der mechanischen Eigenschaften von gewickelten Faserverbundkeramiken mit unterschiedlichen Faserorientierungen. Hierfür wurden die Kenndaten einer virtuellen äquivalenten unidirektionalen Schicht (UD-layer) zuerst berechnet und anschließend durch die Inverse-Laminat-Theorie und ein modifiziertes Tsai-Wu Versagenskriterium angewendet.

Alle in dieser Arbeit angewendeten Modellierungsansätze werden auf der Basis von den mechanischen Untersuchungen und der Analyse der Mikrostrukturen entwickelt. Die vollständige Erfassung der Materialeigenschaften von WHIPOX™ bei unterschiedlichen Wickelwinkeln bzw. Faserorientierungen, einschließlich Steifigkeit, Festigkeit, Dehnung, elastischen und inelastischen Verhalten, erfolgt anhand von experimentellen „in-plane“ Untersuchungen. Nach der Mikrostrukturanalyse durch Micro-Computertomographie wird die Modellierung der mechanischen Eigenschaften in zwei Gruppen eingeteilt: WHIPOX™ mit Matrix-Schrumpfrissen (kurz auch WC für with cracks) und WHIPOX™ ohne Matrix-Schrumpfrisse (kurz auch NC für no cracks).

Eine besondere Schwierigkeit bei der Modellierung des mechanischen Verhaltens gewickelter CMCs, wie z. B. bei WHIPOX™, besteht in den fehlenden Daten der Matrix- bzw. Fasereigenschaften nach der Fertigung des Verbundwerkstoffs. Die Herstellung von ausschließlich unidirektional verstärkten Laminaten (UD-Schicht) ist bei CMCs kritisch wegen des unbehinderten Schrumpfens der Matrix quer zur Faserverstärkung während der Abkühlphase. Damit stehen für die traditionellen Modellierungsmethoden und die klassischen Versagenskriterien keine repräsentativen experimentellen UD-Messdaten zur Verfügung. Alternativ werden fortgeschrittene Modellierungsansätze mit Hilfe von virtuellen äquivalenten UD-Schichten für die Beschreibung und die Vorhersage der Materialeigenschaften des untersuchten WHIPOX™-Materials erstellt. Als Kernkomponente der Modellierungskette wurden die vollständigen Materialeigenschaften der äquivalenten UD-Schicht berechnet und ausgewertet: elastische Eigenschaften durch den inversen Ansatz auf Basis der klassischen Laminattheorie (CLT); Festigkeiten durch Anpassung der verschiedenen Testergebnisse zum modifizierten Tsai-Wu Versagenskriterium; Bruchdehnung unter Verwendung des inelastischen Verformungsfaktors Δ. Alle Werte werden unter Berücksichtigung der unterschiedlichen Mikrostrukturen mit oder ohne Matrixrisse diskutiert und ermittelt. Durch das Stapeln dieser äquivalenten UD-Schichten mit beliebiger Faserorientierung, z. B. nicht-orthogonal, orthogonal und asymmetrisch (off-axis), wird ein äquivalenter Schichtverbund erzeugt und dessen Materialkonstanten können mittels der modifizierten Steifigkeitsmatrix vorhergesagt werden.

Um die mechanischen Eigenschaften mit mehr Genauigkeit vorherzusagen, müssen einige Besonderheiten der untersuchten Materialien berücksichtigt werden. Für den Verbundwerkstoff WHIPOX™ sind vier besondere Merkmale in den Modellierungsansätzen implementiert: Identifizierung der Inhomogenität der untersuchten Platten; Aufteilung der Modellierungsgruppen auf Basis der Analyse von Mikrostrukturen; Interaktion zwischen Festigkeit und Bruchdehnung mit Berücksichtigung der inelastischen Verformung;

Fortschreibung des analytischen Modells für die verschiedenen Chargen mit der durch Herstellungsprozess bedingten Inhomogenität.

Aufgrund der guten Korrelation zwischen den Untersuchungs- und Modellierungsergebnissen konnte gezeigt werden, dass die Modellierungsansätze mit Berücksichtigung der oben genannten Materialbesonderheiten eine sehr genaue Vorhersage der „in-plane“ mechanischen Eigenschaften für CMC-Materialien ermöglichen. In der vorliegenden Arbeit konnte eine allgemeine Vorgehensweise zur Vorhersage der mechanischen Eigenschaften von gewickelten CMCs mit unterschiedlichen Faserorientierungen anhand der experimentellen Ergebnisse und der Mikrostrukturanalyse entwickelt werden. Die Ergebnisse dieser Arbeit sind sehr wertvoll für das zukünftige Design und die Entwicklung dieser Verbundwerkstoffe. Hierdurch wird das Anwendungspotential von CMC-Komponenten in Bereich wie der Luft- und Raumfahrttechnik und der Maschinenbau verbessert.

Content

List of figures

List of tables

Nomenclature

Abbreviations:

CLT	Classic Laminate Theory
CMC	Ceramic Matrix Composite
CT	Computer Tomography
DLR	German Aerospace Centre
FE	Finite Element
FF	Fiber Failure
FPF	first-ply-failure
FVC	Fiber Volume Content
IFF	Inter Fiber Fracture
ILT	Inverse Laminate Theory
LPF	last-ply-failure
NC	No Cracks
NDI	Non Destructive Inspection
RVE	Representative Volume Element
UD-layer	Uni-Directional layer
US	Ultrasonic
WC	With Cracks
WHIPOX™	Wound Highly Porous Oxide Ceramic
WIC	Weak Interface Composites
WMC	Weak Matrix Composites
wt. %	Weight Percent

Symbols:

Δ	Inelastic deformation factor
ε_{ij}, ε_{kl}	Strain component
θ	Fiber orientation
σ_i, σ_{ij}	Stress component
Ω	Manufacturing factor with fiber volume content and porosity
ρ_F	Density of the fibers
e'	Porosity
F_i, F_{ij},	Strength parameters of Tsai-Wu failure criteria
G_k, G_{kl}	Strain parameters of Tsai-Wu failure criteria
$\sum_{ij}$	Corresponding failure indices
k	Inverse value of strength ratio R
t_k	Thickness of each layer
z_k	Distance between the middle surface of the laminate to the top or bottom of each layer
$\bar{z}_k$	Distance between the middle surface of the laminate to the middle surface of each layer
$\bar{Q}_{ij}$	Stiffness of each layer in global coordinate system
Q_{ij}	Stiffness of each layer in local coordinate system
S_{ij}	Strain stiffness
C_{ij}	Coupling stiffness
B_{ij}	Bending stiffness
$E_{x,y}^{T,C}$	Young's modulus in x or y direction and T for tensile test and C for compression test
ν_{xy}	Poisson's ratio
G_{xy}	Shear modulus
$\sigma_{x,y}^{T,C}$	Strength in x or y direction and T for tensile test and C for compression test
$\varepsilon_{x,y}$	Failure strain in x or y direction
R	Strength ratio of Tsai-Wu failure criteria

V_C	Volume of the component
W_F	Weight of the fibers
W_{dry}	Weight of the component
W_{water}	Weight of the component when submerged in water
W_{wet}	Weight of the component after being taken out from water
S_{ij}	Strain stiffness
C_{ij}	Coupling stiffness
B_{ij}	Bending stiffness

1 Introduction

Nowadays, composite materials can be found in almost any product imaginable. As some of the most important representatives of composites, Ceramic Matrix Composites (CMCs) have become the focus of attention of material development researchers in recent years, because of their favorable mechanical properties at high temperature and comparatively low density. By using the excellent high temperature properties of ceramic fiber and ceramic matrix, the CMC materials exceed all materials in that field of interest. Therefore, the CMCs are predestinated for aerospace and other applications that require stability in mechanical behavior at high temperatures [1-4]. However, the potential of CMCs for application in varied technologies has been partly limited due to their complicated manufacturing process. Thanks to its high flexibility, net shape fabrication and relatively low cost, the winding technique for the production of complex CMC components, especially the production with stress-oriented fiber alignment and rotational symmetry axis, has been rapidly adapted in aviation and aerospace technology and some other industrial areas [5-9].

Fundamental material models have to be established and applied in order to optimize the newly developed CMC materials and to design the CMC structure for high-performance applications. Since the winding angle of each layer can be adjusted in any desired direction (from 0° to 90°) during the manufacturing process, the wound CMC components with pronounced anisotropic mechanical properties may be designed and optimized with stress-optimized fiber arrangements. Due to the complex anisotropic in-plane material behavior, the accurate prediction and assessment of the material properties of CMC components, such as the material WHIPOX™ (Wound HIghly Porous OXide Ceramic) investigated in this work, has to be supplemented by advanced modeling approaches. Several analytical and numerical approaches have been developed and implemented for the prediction of the mechanical behavior of wound and braided materials, especially for the fiber reinforced composites with polymeric matrices. As being based on the material homogenization techniques, meso- and microscopic methods by using Representative Volume Unit (RVU), Classical Laminate Theory (CLT) and classic failure criterion allow for a good estimation of elastic properties [10-15], maximal loading capacity [16-18] and progressive damage [19-21].

In comparison with the fiber reinforced polymeric composites, the main problem of modeling wound CMCs is the lack of data concerning fiber and matrix properties within the composite material, especially with regards to the matrix. After the complex manufacture processing the microstructure of matrix, such as micro-crack density and specific matrix-porosity, are totally different from pure matrix properties and depend on the fiber orientation. On the other hand, the material properties of fibers within the composite are unknown since they may differ from their original state as a result of the thermal load sustained during the fabrication of the composite. Another concept is the modeling with unit cell which includes the mixed properties of the fiber, the matrix and the repeatable in- and out-plane tow architecture within a representative volume unit. Due to the required redefinition of varied fiber orientations, the use of the unit cell model is not efficient in the case of continuous variation of in-plane architecture (e.g. the winding angle) of the laminates within the composite. Furthermore, modeling of mechanical properties by direct implementation of the Classical Laminate Theory and classic failure criterion (e.g. Tsai-Wu criteria and Puck criteria) is very sensitive concerning wound CMCs. These approaches are based on the mechanical constants of individual Uni-Directional-layers (UD-layer) and the stacking sequence of the UD-layer. However, the production and characterization of characteristic CMC UD-materials is almost impossible because of the non-typical unhindered shrinkage of matrix transverse to the fibers during the production process. This prevents the UD-material from being considered as a representative material for modeling approaches for CMCs.

Due to the above mentioned problems, advanced modeling approaches, on the basis of the complete mechanical characterization of material properties, shall be created for the evaluation and prediction of the material behavior of wound CMC components. A chain from testing to modeling is presented in this work (see section 5.6). As the core component of the modeling chain, complete material properties of a virtual equivalent UD-layer were calculated and evaluated. It was shown that the Classical Laminate Theory (CLT) and the Inverse Laminate Theory (ILT) can be used to calculate the elastic properties of equivalent UD-layer with different microstructures. By using the strength ratio R of Tsai-Wu failure criteria the strength values of the laminate with different fiber orientations can be predicted. A modified stiffness matrix with an inelastic deformation factor Δ leads to a precise calculation of failure strain and has been used to describe the inelastic stress-strain behavior. All the values of the equivalent UD-layer are discussed and calculated with consideration given to different microstructures with or without matrix cracks. Through the stacking of these equivalent UD-layers with any desired fiber orientation, e.g. non-orthogonal, orthogonal and asymmetrical (off-axis), an equivalent layered composite is created and its material constants can be predicted by using the modified stiffness matrix. In order to predict the mechanical properties with more accuracy, the chain from testing to modeling was created with consideration of distinctive features of the investigated composite WHIPOX™: identification of inhomogeneity of the investigated plate; interaction between failure strength and strain through inelastic deformation; division of material modeling groups based on the analysis of microstructure; update of analytical model of different batches with inhomogeneities created due to the manufacturing process. This modeling chain based on the material WHIPOX™ can be applied to predict the mechanical properties of other CMCs. The results of modeling are compared with the experimental results of other CMCs and presented in this study.

2 State of the art

2.1 Bases of oxide/oxide CMCs

The term “Ceramic Matrix Composites (CMC)” refers to the composites in which ceramic fibers are embedded in oxide or non-oxide ceramic matrices. Due to the similar failure strain and the brittle fracture behavior of both fiber and matrix, the reinforcement of ceramic fibers, in contrast with “carbon fiber reinforced polymer (CFRP)”, cannot be seen being as equivalent to “fiber reinforced ceramics”, because the strength of fiber reinforced ceramic cannot be higher than the maximum value of monolithic ceramic. For example, the flexural strength of monolithic aluminium oxide ceramic is approx. 500 MPa (99.8 % Al_2O_3 in [22]) and the value of the in this study investigated Ox/Ox CMC WHIPOX™ is approx. 80-350 MPa (ranges of data obtained for WHIPOX™ with different fiber types and processing parameters in [23]). Therefore, in comparison with the strength enhancement by CFRP materials, the great potential of CMCs lies in the fact that the advantages of high-performance monolithic ceramic can be obtained with enhanced toughness as the seriously disadvantageous brittle fracture behavior is eliminated by the introduction of fibers. Although both compositions of CMCs, i.e. ceramic fibers and ceramic matrices, are brittle, the composite shows quasi-ductile deformation behavior due to mechanisms such as fiber pull-out, multiple matrix cracking and crack bridging [24]. A prerequisite for these mechanisms is the relatively weak bond between ceramic fibers and the matrix. In general, there are two approaches that can be applied to accomplish weak fiber/matrix bonding: either suitable fiber coatings or the use of a weak matrix e.g. with highly porous matrix [25, 26]. The toughness enhancing mechanisms of these two concepts are discussed in section 2.2.1.

A possible division of CMC materials can be performed according to the chemical characters of fiber and matrix (oxide or non-oxide): CMCs consisting of non-oxide fiber (e.g. C-fiber and SiC-fiber) embedded in non-oxide ceramic matrix (e.g. C, SiC and SiCN) can be called a non-oxide/non-oxide CMC; an oxide combination with oxide fiber (e.g. Al_2O_3-fiber and Al_2O_3/mullite-fiber) and oxide matrix (e.g. Al_2O_3 and mullite) exists for oxide/oxide CMCs. In addition to pure oxide and pure non-oxide CMCs, a further uncommon CMC group with oxide-fiber in a non-oxide matrix or non-oxide fiber in an oxide matrix, “semi-oxide CMCs” can be produced through directed metal oxidation process [27, 28]. The non-oxide/non-oxide CMCs obtain usually high strength and good creep resistance at high temperature as a result of their predominant covalent atomic bonding. However, compared to oxide/oxide CMCs, non-oxide/non-oxide CMCs are susceptible to oxidation due to their chemical characters. Therefore, for many years numerous investigations have been conducted to improve the oxidation resistance of non-oxide ceramics with the addition of external protective coatings (e.g. [29]). The thermal expansion of the coating materials is usually higher than the non-oxide substrates (e.g. [30, 31]). This results in cracking and spallation of the coatings under thermal loading. Therefore, long-term stability against oxidation for non-oxide/non-oxide CMCs is difficult to achieve. By comparison, oxide/oxide CMCs offer good stability against corrosive and oxidative environments. This makes them promising candidate for use in structural materials, thermal protection and as applications aiming at high temperatures such as combustion chambers, components of aircraft and gas turbine, e.g. in [8, 32-36]. Thus, in this section the bases of oxide/oxide CMCs are introduced.

As mentioned above, the mechanisms used for reducing the brittleness of CMC materials, e.g. oxide/oxide CMCs, require a relatively weak fiber-matrix bonding. In order to prevent a very strong adhesion between fiber and matrix, ceramic fibers are frequently treated with suitable coatings. Thus, oxide ceramic matrix composites consist of three components: oxide fiber, fiber coating and oxide matrix.

Oxide ceramic fibers

First, an overview on the oxide fibers is given. Oxide fibers for CMCs are typically polycrystalline. They were first developed in order to use their excellent oxidation stability for high temperature applications [37, 38]. They are mainly composed of alumina (α- or γ-Al_2O_3) or mullite (mixed oxides of Al_2O_3 and SiO_2), and sometimes of additional zirconia (ZrO_2) or amorphous silica (SiO_2). The micro structure of these fibers is thermodynamically non-stable. In the case of alumina, the thermodynamically non-stable γ-Al_2O_3 phase can react with other consistencies (e.g. γ-Al_2O_3 + SiO_2 → mullite), which decreases the final stiffness and creep resistance of the oxide fibers. Only small amounts of SiO_2 prevent unexpected grain growth [39]. Furthermore, a clear grain growth phase of α-Al_2O_3 within the fibers at high temperatures (e.g. 1200 °C to 1300 °C) can be observed, which leads to a significant reduction in the strength of the oxide fibers [39-41]. The high-strength oxide fibers are commercially available: 3M from the USA ([41]); NITIVY from Japan ([42]) and CeraFib from Germany ([43]). Nowadays, two typical continuous oxide fibers developed by company 3M dominate the commercial market: pure alumina Nextel™ 610 (N610) and mullite-alumina Nextel™ 720 (N720). An overview of the mechanical properties of N610 and N720 are listed in Table 2.1 and the data were obtained from [41]. While the tensile strength and stiffness of filament N610 are high (Table 2.1), its creep resistance is rather poor compared to the fiber N720. This is because the grain size of N610 (approx. 90 nm in [44]) is clearly finer than the mullite based fiber N720 (grain size of mullite is approx. 300 nm in [44]). The oxide/oxide CMC WHIPOX™ in this work investigated was manufactured using the oxide fiber N610 as roving.

Table 2.1: Overview of the mechanical properties of oxide fiber N 610 and N720 [41].

Fiber	N610	N720
Chemical composition [wt. %]	> 99 Al_2O_3	85 Al_2O_3 and 15 SiO_2
Crystal Phase	α-Al_2O_3	α-Al_2O_3 + mullite
Filament diameter [µm]	10 - 12	10 - 12
Density [g/cm^3]	3.9	3.4
Filament tensile strength [MPa]	3100	2100
Filament tensile stiffness [GPa]	380	260

Oxide/oxide CMCs with dense matrix

For oxide/oxide CMCs with dense matrix, the improvement of toughness is related to crack bridging/deflection at fiber-matrix interface and further fiber pull-out [45, 46], which is typically accomplished by modifying the fiber-matrix bonding through the use of fiber coating. Several methods have been developed for the deposition of coating material onto oxide ceramic fibers. Some comprehensive reviews of ceramic fiber coatings are available, e.g. [47, 48]. A few typical examples are introduced here. The choice of a coating process usually depends on the coating material. The chemical vapor deposition (CVD) has been successfully applied to deposit fiber coatings with carbon (C) and boron nitride (BN) in desired orientations [49]. However, due to their chemical character, C and BN are susceptible to oxidation and thus not suitable for long-term application in oxidizing atmospheres. Although the oxidation resistance of single-layer coating can be significantly improved by double-layer fiber coating, e.g. BN/SiC, long-term oxidation stability at high temperature (e.g. above 1200 °C – 1300 °C) is not achieved ([50]) and the procedure of multi-layer coating is very complex. Liquid precursor coating techniques with slurry/sol/solution allow the immiscible floating of multi-component oxides (e.g. monazite) to deposit on the individual ceramic filaments [51]. Due to the relatively low efficiency of this method several coating passes are needed for fiber coating with certain thickness (e.g. > 50 nm) and sufficient density. Furthermore, in order to prevent the strength degradation of fiber through surface active decomposition products during the liquid precursor coating, the floating chemistry must be carefully controlled [52]. A major problem by fiber coating technique is the bridging and crusting of the coating materials, which decreases their capacity to improve the toughness of CMCs. As compared to dense fiber-matrix interfaces, some studies about porous coating ([53]) and fugitive coating ([54]) have been reported. Several coating materials for porous coating have been examined, e.g. mixed carbon/zirconia (ZrO_2) slurry was deposited on sapphire fibers. After the embedment of coated fibers in an alumina matrix, the carbon was removed by oxidation [53]. The term fugitive coating is used for fiber coating that is totally removed (fugitive interface) after the manufacturing of CMCs ([54]). The ceramic fibers with these weak interfaces would easily pull away from the fractured matrix and corresponding pull-out lengths are long [53, 54].

In order to make the best use of coated oxide fibers, procedures to manufacture oxide/oxide CMCs with highly dense matrices must be developed. The production of oxide/oxide CMCs with high matrix density is complicated to achieve. On the one hand, the preparation of dense and defect free crystalline matrix is challenging because the matrix shrinkage within a rigid fiber network at high temperatures typically leads to a high amount of cracks. On the other hand, the temperatures and pressures are strongly limited by the need to prevent damage to the fibers during the process. It has been demonstrated that dense oxide/oxide CMCs can be fabricated using hot pressing ([55, 56]) and hot isostatic pressing ([57]). However, the potential for damage to the fiber is significant. To avoid a reduction in the mechanical properties of oxide fibers [39-41], the temperature should not exceed 1300 °C, which is needed for manufacturing a matrix of full density. Therefore, most oxide/oxide CMCs are sintered without pressure at relatively lower temperatures and then re-infiltrated with e.g. slurry or sol oxide precursors to increase the matrix density (Polymer Infiltration Pyrolysis process PIP in [58]). Since only small increments in densification can be achieved in each step, the re-infiltrated method typically requires a number of infiltrated steps ([59, 60]). UMOX™ and OXIPOL® are two typical oxide based CMCs with fiber coating (fugitive interface) and manufactured by PIP process. Material UMOX™ was developed and manufactured at EADS Innovation Works (Munich, Germany). The fiber of UMOX™ is Nextel 610 and matrix is based on a commercial micron-sized mullite powder and polysiloxane precursor. Typical fiber volume content is 48-50 % with 10-12 % porosity and density of 2.4-2.5g/cm^3. More details about the manufacturing process and mechanical properties of UMOX™ was pursued in a PhD thesis [61]. Material OXIPOL® was developed and manufactured at DLR Institute of Structures and Design (Stuttgart, Germany). This oxidic CMC is built up by oxide ceramic fabrics and a SiOC matrix derived from polysiloxane. Typical fibre volume content was about 42.5 % and open porosity of approximately 10 % after five PIP cycles. The manufacturing process and mechanical properties of OXIPOL® can be found in [62].

Oxide/oxide CMCs with porous matrix

In order to engineer the intensity of the fiber-matrix interface as an alternative concept to CMCs with dense matrix and fiber coatings, oxide composites with a porous matrix and without fiber-matrix interphases have been successfully developed since the mid-1990s [26]. A significant advantage of these materials is that they eliminate the need for fiber coating, which affects the ease and cost of experimentation and the ultimate cost of the CMC materials.

In comparison with CMCs with a dense matrix, the oxide/oxide CMCs with a porous matrix consist of only two components: oxide fiber and porous oxide matrix. The porous matrix plays a similar role as the above mentioned fiber-matrix bonding with porous coating. The bonding between the incorporated fibers and the porous matrix is typically weak to allow for matrix crack deflection in the matrix near the fiber-matrix interface. Moreover, the strength of the porous matrix should be sufficiently high to transfer a certain amount of load from one fiber to another. At the same time, it should be low enough to enable a quasi-ductility fracture by crack branching within the matrix and debonding the fibers and matrix.

The same oxide fibers discussed above (e.g. in Table 2.1) are combined with various matrix materials to produce porous oxide/oxide CMCs. Table 2.2 gives an overview of typical activities observed in oxide/oxide CMCs with porous matrix. Some important research and development concerning these materials are conducted by the Germany Aerospace Center (DLR, Germany), the University of California (USA), the University of Bayreuth (Germany) and General Electrics (USA). In addition, porous oxide/oxide CMCs are commercially available, inter alia, from Composite Optics, Inc. (COI Ceramics, USA) and Pritzkow Spezialkeramik (Germany). The latter closely cooperated with Fraunhofer ISC / Center for High Temperature Materials and Design (Germany) in recent years ([34, 63]). The processing techniques for porous oxide/oxide CMCs are similar [34, 64-66]. First, ceramic textile preforms, e.g. woven fabrics with N610 or N720, are infiltrated by a matrix slurry which bonds the fibers together by a so-called CSI process (Ceramic Slurry Infiltration). Next, the prepregs can be stacked to form laminate with the required fiber orientations. Then the laminates are molded and sintered in air at a high temperature (e.g. 1000 °C – 1300 °C). A typical microstructure of porous oxide/oxide CMCs is shown in Figure 4.2.

Table 2.2: Overview of typical activities on oxide/oxide CMCs with porous matrix through Ceramic Slurry Infiltration (CSI).

Institution and company	Fibers	Matrix	Typical composite	Shaping of components	Reference
DLR (Germany)	N610 N720	Alumina, Alumino -Silicate	e.g. WHIPOX™ (N610/Alumina)	Filament winding	[67]
University of California (USA)	N610, N720	Mullite -Alumina	e.g. N610/Mullite -Alumina	Lamination of woven fabrics	[68]
University of Bayreuth (Germany)	N610, N720	Mullite -Alumina	e.g. N610/Mullite	Lamination of woven fabrics	[64]
General Electric (USA)	N610,	Alumino -Silicate	e.g. GEN-IV (N610/ Alumino -Silicate)	Lamination of woven fabrics	[65]
COI Ceramics (USA)	N312, N610, N720	Alumina, Alumino -Silicate	e.g. COI 720/AS (N720/Alumino -Silicate)	Filament winding, Lamination of woven fabrics	[66]
Pritzkow Spezialkeramik (Germany)	N610, N720	Alumina, Mixtures (e.g. Al_2O_3-SiO_2, Al_2O_3–ZrO_2)	e.g. FW12 (N610/Alumina +Zirconia)	Lamination of woven fabrics	[34]

As compared to the other CMCs with lamination of woven fabrics, the porous oxide/oxide CMC WHIPOX™ in this work investigated is manufactured using a filament winding technique. The manufacturing process and production parameters for the plate material are presented in section 4.1. The fabrication of composites via the winding process brings a number of benefits:

- The winding angle can be adjusted in any desired direction (from 0° to 90°) for load optimized fiber orientation.
- Different and complex shapes are possible using suitable plastic mandrels.
- Grid structures can be achieved by variation of the winding pattern.
- The fiber volume content can be adjusted by modification of particle size distribution within the slurry [69].

Because of the high flexibility of fiber orientation created by winding technique, the variability of the fiber arrangement requires advanced models for the modeling and prediction of the mechanical properties of CMC components. Detailed descriptions of the developed advanced modeling approach for wound CMCs are introduced in section 7.

2.2 State-of-the-art in mechanics of CMCs

2.2.1 Concept of toughness enhancing mechanisms for CMCs

As mentioned in section 2.1, there are two concepts which can be applied to enhance the toughness of CMCs, either suitable fiber coatings for Weak Interface Composites (WICs) or weak matrices for Weak Matrix Composites (WMCs).

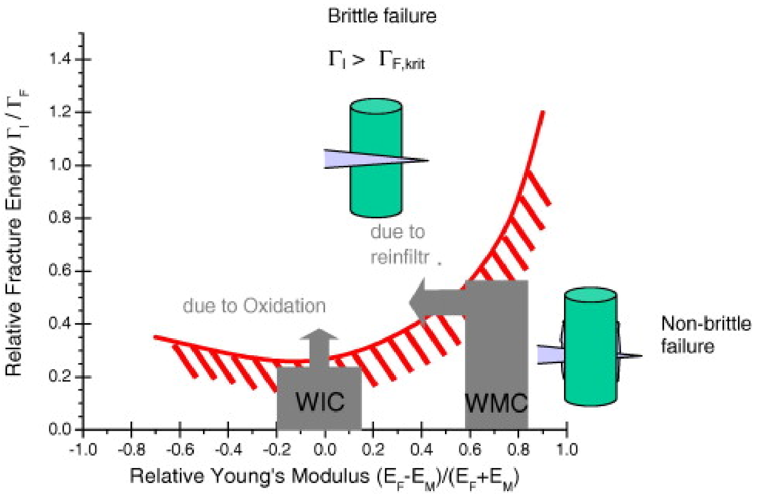

Figure 2.1: Explanation of brittle and non-brittle CMC behavior with respect to the relative fracture energy of interface and fiber and the relative stiffness of fiber and matrix [70] (Adapted with permission from Elsevier).

WIC materials typically have a dense matrix but a weak fiber-matrix interface in order to allow debonding between fibers and matrix. This increases the fracture toughness of the composites [25, 70]. In contrast, WMC materials have a weak and soft matrix, which enables a crack deflection to occur within itself while preventing the brittle failure of CMCs [26, 70]. Based on the initial works concerning crack deflecting mechanisms in [25, 71], a direct connection between the failure mode and the relative fracture energy of interface and fiber (Γ_I/Γ_F) as well as the relative stiffness of fiber and matrix $((E_F - E_M)/(E_F + E_M))$ can be plotted in Figure 2.1 ([70]). Generally, non-brittle failure with debonding effects occurs if the ratio of fracture energies is low. In the case of WICs, the Young's modulus of matrix and fiber are similar, therefore the fracture energy of the interface relative to the fibers must be rather low $(\Gamma_I/\Gamma_F < 0.25)$ to prevent brittle failure. With WMCs, the stiffness of the matrix is usually much lower compared to the fibers, thus the properties of the interface will play a minor role (Figure 2.1). According to the analysis of the microstructure in Figure 4.2, the investigated material WHIPOX^{TM} typically shows a porous alumina matrix. A defined interface between the fiber and matrix, e.g. due to fiber coating, does not exist for WHIPOX^{TM}. Therefore, WHIPOX^{TM} should be classified as a WMC material from a microstructural point of view.

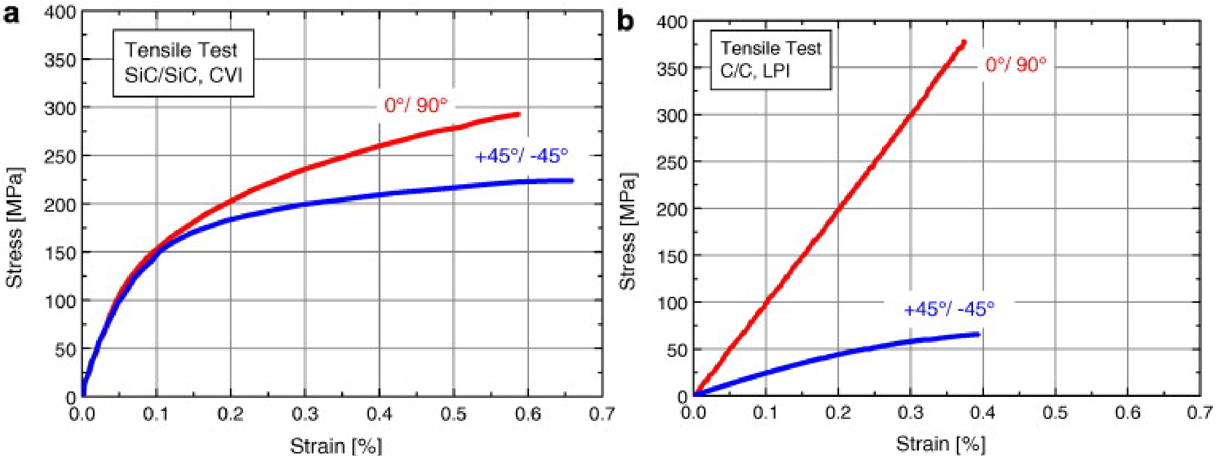

Figure 2.2: Representative tensile stress-strain curves in axial (0°/90°) and diagonal (+45°/-45°) directions of (a) a WIC composite SiC/SiC by Chemical Vapor Infiltration (CVI) and (b) a WMC composite C/C by Polymer Infiltration and Pyrolysis (PIP) [70] (Adapted with permission from Elsevier).

However, the tensile stress-strain curves of typical WICs and WMCs in Figure 2.2 [70] show that it is difficult to classify WHIPOX^{TM} according to its macroscopic mechanical behavior. The weak matrix with low stiffness leads to a significantly different stress-strain behavior in a WMC (C/C in Figure 2.2b) in comparison with a WIC (SiC/SiC in Figure 2.2a). The typical WMC material in Figure 2.2b shows strong differences between the 0°/90° and the ±45° directions: in the axial direction (0°/90°) the behavior is almost linear elastic and in the diagonal direction (±45°) it is strongly non-linear. The strengths and the initial stiffnesses of both directions are totally different. In the case of WHIPOX^{TM}, the tensile stress-strain curve in 0°/90° shows a slight non-linear behavior (see test results in Figure 7.17a) and the ratios of the failure strength and tensile moduli of both test directions (0°/90° and ±45°) are around 1 (see test results in Table 6.1 and Table 6.2). Therefore, as compared to the classification system according to microstructure, the porous WHIPOX^{TM} at a macrostructure level tends more towards a WIC-like behavior even though no fiber coating is used in the material. It should be noted that although a classification of CMCs makes sense to describe and even predict their behavior, a careful and complete inspection for that particular material is necessary.

Moreover, although some reports showed that for WICs (e.g. SiC/SiC by Chemical Vapour Infiltration) a micromechanical approach is applicable ([20, 21]), macroscopic modeling of WMCs mechanical behavior is also possible ([19, 70]). Because of its microstructure and macroscopic mechanical behavior, WHIPOX^{TM} is neither a typical WMC nor a WIC material. Throughout the course of this work, it will be shown that the material behavior of WHIPOX^{TM} can be modeled through macroscopic homogenization with the use of an equivalent UD-layer model. These modeling approaches are presented in section 7.

2.2.2 Modeling of the mechanical properties of CMCs

With a fiber reinforced composite material with variable fiber orientations and different structure parameters (e.g. the material of fiber and matrix and interface, the amount and sequence and thickness of the layers) it is desirable to be able to model the mechanical properties with only few basic data. This helps to minimize the effort required for experimental determination. Several modeling approaches and finite element analysis have been developed and implemented for the prediction of the mechanical behaviors of fiber reinforced materials, especially for composites with polymeric matrices. However, due to their complex nature, a complete and validated methodology for modeling the mechanical behavior of the composite has not yet been fully achieved.

Based on the relationship between models and the physical behavior of composites, modeling approaches can be classified as either implicit or explicit. The implicit models describe the behavior of materials using only a mathematical form of inputs and outputs without representing any underlying physics. Usually an optimum approximation function is used to define the mathematical relationship between experimental data (inputs) and material behavior (outputs). The accuracy of the approximation is strongly dependent on the reliability of the input-output data setting. The implicit models can be developed for any material, for example material with inelastic behaviors [72] and fiber reinforced composites [73]. A significant drawback of implicit models is the limitation of application beyond the range for which they were developed.

Explicit models are classical modeling approaches used to define the constitutive material system by connecting physically based theories with behavior of material. The mechanical behavior of composites is normally defined as constitutive stress-strain relationship, which can be accomplished with scales of different lengths: microscopic, mesoscopic and macroscopic. A further scale at nanolevel was reported in a few publications for CMCs [74]. It should be noted that, by some publications, a distinct division between micro- and mesoscales were not presented. Instead, a general micromechanical approach was defined with mixed micro- and mesoscopic structures. On the basis of the so-called "equivalent inclusion method", which was originally proposed in the 1950s by Eshelby [75], homogenization techniques are performed to define the Representative Volume Element (RVE) for each hierarchy level. The RVE has a suitably small volume, which is large enough to be a good representative of the microstructure of material, was initially defined by Hill [76]. For heterogeneous material, e.g. continuous fiber reinforced composites, the RVE at microlevel is a single long fiber with or without fiber coating. At mesolevel the RVE consists of a number of unidirectional long fibers (with or without coating) surrounded by matrix and other inclusions, e.g. pores within matrix. On a macroscopic scale the RVE presents usually the individual plies (e.g. UD-layer) or laminate (e.g. 0°/90° laminate).

The micro- and mesoscopic methods based on homogenization techniques and on RVE allow for a good prediction of composite properties. At these levels the properties of the RVE consist of its fiber and matrix constituents along with its micro- and mesostructures. The well-known Mori-Tanaka model ([77]) is widely used for modeling the mechanical properties of different composite materials. This is an inclusion model, where fibers are considered to be inclusions embedded in a homogeneous medium (matrix). Another well-known model is the self-consistent model which has been proposed by Hill [78] to be useful in the modeling of the elastic properties of composite materials. By using continuum damage mechanics with factoring in the development of matrix cracking and fiber failures based upon fracture statistics, the prediction of progressive damage can be achieved for CMCs, especially for WICs e.g. SiC/SiC by Chemical Vapour Infiltration [20, 21]. More complex models may also include the interface and interphase region between fiber and matrix [79]. The numerical evaluation of these models can be accomplished by means of the Finite Element

Method (FEM) [80, 81]. Due to the required redefinition of RVEs for varied fiber orientations of wound CMCs, the use of micro- and mesoscopic models is not efficient.

The modeling approach at the macroscopic level usually involves analyses at a range of scales that includes the UD-layer. Similar to the RVE, the UD-layer model can be considered as identical repetitive elements for prediction of mechanical behavior of CMCs. Ideally, the available stiffness parameters of fibers and matrix as well as their respective contents can be used to evaluate the properties of UD composites through the so-called mixing rule. Based on the properties of individual UD-layers and the stacking sequence, the Classic Laminate Theory (CLT, see section 5.1) can be adapted for composites. The initial rule of mixture models was proposed by Voigt in [82]. Several models with more factors emerged later to correct the Voigt-model. This was especially the case when is came to the results of young's modulus in transverse direction and shear modulus, e.g. Halpin-Tsai model in [83] and Chamis-model in [84]. However, due to the lack of data concerning the fiber and matrix properties after composite manufacturing, the determination of engineering constants through fiber and matrix and the law of mixtures is particularly difficult. Furthermore, in comparison with fiber reinforced polymer composites, the manufacture and characterization of representive UD-CMC-materials is almost impossible due to the non-typical unhindered shrinkage of matrix transverse to the fibers during the production process. This prevents the UD-material from being considered as representative material for CLT. In order to solve these problems, an inverse approach for CLT using an equivalent UD-layer to determine the material behavior is presented in this work and some results have been reported in [85-88].

2.2.3 Failure criterion

Usually, the individual strengths determined from simple specimens under tensile, compression and shear testing are used to measure the mechanical load capacity of a material. However, because of the complicated multi-axial load, the dimensions of the components with practically oriented designs and constructions require a guaranteed failure criterion. This should connect the loads in the components and the individual strengths determined from single tests. Such failure criterions for isotropic materials have been long in theoretical development. They reduce the multi-axial stress in components down to a single so-called equivalent stress, which is then compared with a single strength, usually the tensile strength. The prerequisite for the application of most classical failure criteria is that the material must be able to be considered to be a homogeneous, isotropic continuum with direction independent failure behavior. However, these assumptions are not suitable in the case of fiber reinforced composites: anisotropic properties with direction dependent strength; different tensile and compressive strengths; anisotropy of fracture types, e.g. fracture of the component A (e.g. fiber) under load in one direction and fracture of component B (e.g. matrix) or interfacial fracture between component A and B under load in the other direction. On the other hand, due to the large number of possible design parameters (e.g. the material of fiber and matrix, the amount and sequence of the layers, the fiber orientation and thickness of each layer) it is not possible to achieve a failure criterion for all cases through mechanical experiments. Therefore, similar to stiffness modeling in section 2.2.2, most approaches for the failure analyses are performed on the basic element of a laminate, the UD-layer. Above all, there are a number of theories concerning failure criterion for composites (e.g. compiled in [89-91] and reviewed in [92-94]), but a fully satisfying solution is not yet available. A rough briefing of the commonly applied failure criteria is presented in this section.

Failure criteria can be formulated as strain or stress criteria. In principle, both forms are identical because stress and strain are causally related through the stiffness matrix. Thus, one form can be converted in the other form. However, it is hampered by significant practical difficulties with non-linear stress-strain relationships. Stress failure criteria for isotropic and brittle materials were based on the works of Mohr [95]. Von Mises and Tresca complemented this hypothesis by developing a criteria named after von Mises with implementation of yield stress for plastic deformable materials [96]. Based on the von Mises yield criteria, Hill developed one of the first anisotropic failure criteria, which is suitable for use with ductile metallic material with slight anisotropic homogeneous properties [97]. However, the condition needed for the application of this criterion is an equal tensile and compressive strength in the respective axis direction, which is usually not the case with fiber reinforced composites. Following yield conditions for orthotropic materials, numerous authors, e.g. Goldenblat-Kopnow in [98], Hoffman in [99], Tsai-Hill in [100] and Wu-Scheublein in [101], proposed quadratic fracture conditions with interpolation functions for laminates. Based on those ideas, a polynomial tensor can be used to describe the failure surface. The most commonly applied hypothesis is the Tsai-Wu failure criteria ([16]). This uses a similar approach by considering interactions between different components of the stress and strain tensor. It is argued that the difference between fiber breakage and matrix cracks cannot be distinguished by the Tsai-Wu criteria. However, it has been improved by using the modified definition of the directional failure indices by the work of Paepegem in [18]. Therefore, it appears that it is now possible to predict which stress component is mainly responsible for failure. An approach for the material WHIPOX™ based on the statistical criteria has been reported recently in [102]. A correlation between the experiment and computed results can be observed for few different fiber orientations. A significant drawback of this approach is the limitation of practical applicability for other winding angles. An overview of some typical non-physically based failure criteria for composite with anisotropic properties is summarized in Table 2.3.

Table 2.3: Overview of some typical non-physically based failure criteria for composite with anisotropic properties.

Non-physically based failure criteria K_{1-5}, C_{1-5} and $F_{i,j,ijk}$: strength parameters; $\sigma_{i,j,k}$ and τ_{12}: stress component			
Hill (1948)	$K_1\sigma_1^2 + K_2\sigma_2^2 + K_3\sigma_1\sigma_2 + K_4\tau_{12}^2 = 1$	Equal tensile and compressive strength in the respective axis direction	[97]
Goldenblat-Kopnow (1965)	$(F_i\sigma_i)^\alpha + \left(F_{ij}\sigma_i\sigma_j\right)^\beta + \left(F_{ijk}\sigma_i\sigma_j\sigma_k\right)^\gamma + \cdots = 1 \qquad (i,j,k = 1,2,6)$	General formulation of failure criterion in the form of polynomial tensor	[98]
Hoffman (1967)	$C_1(\sigma_1^2 - \sigma_1\sigma_2) + C_2\sigma_2^2 + C_3\sigma_1 + C_4\sigma_2 + C_5\tau_{12}^2 = 1$	Different tensile and compressive strength in fiber and transverse directions	[99]
Tsai-Hill (1968)	$K_1\sigma_1^2 + K_2\sigma_2^2 + K_5\sigma_1\sigma_2 + K_4\tau_{12}^2 = 1$	Particular case from Hill-criterion for transverse isotropic strength	[100]
Tsai-Wu (1971)	$F_i\sigma_i^2 + F_{ij}\sigma_i\sigma_j = 1 \quad (i,j = 1,2,6)$	Detailed description of Tsai-Wu criterion is shown in this work	[16]
Wu-Scheublein (1974)	$F_i\sigma_i + F_{ij}\sigma_i\sigma_j + F_{ijk}\sigma_i\sigma_j\sigma_k = 1 \qquad (i,j,k = 1,2,6)$	Cubic failure criterion from Goldenblat-Kopnow with $\alpha = \beta = \gamma = 1$	[101]
Paepegem (2003)	$f_{Paepegem}\left(\sum_{ij}\right) = 1 \quad (i,j = 1,2)$	Extension of Tsai-Wu criterion with directional failure indices $\sum_{ij}$ (section 5.3.4)	[18]
T. Becker (2016)	$P_{f.comp.} = 1 - exp\left[-\int_{V_{comp.}} g(\sigma)dV\right]$	$P_{f.comp.}$: Probability of failure $g(\sigma)$.: stress dependency of failure probability in the whole volume of the component V_{comp}	[102]

Several physically based criteria have been developed in the last years. One of the most important is the work of Puck in [17]. According to the hypothesis, two basically independent criteria are applied: one for fiber failure (FF) and the second for inter-fiber failure (IFF). The latter one includes the matrix cracks and interface failure between fiber and matrix. In this model, the stresses in the fracture surface are responsible for IFF. In the case of positive normal stress on the fracture plane, all the stress components foster failure.

In contrast negative stress increases the strength because of internal friction. Based on Puck's model, an engineering guideline for strength analysis of the fiber reinforced plastics components was released by the association of German Engineers (VDI) [103]. By adding the influence of the layer thickness and layer angles of the neighboring laminate, the Puck theory was improved in regards to prediction of the initial failure stress [104]. Furthermore, based on the stress invariants, the behavior of five different failure modes (two FF and three IFF) can be calculated by Cuntze model with consideration of probability of failure ([105]). Generally, to evaluate the inclination of the fracture surface at zero normal stress using the Puck failure criterion or Cuntze model, strength values and additional material parameters are required. Due to the lack of recommendations for these inclination parameters (e.g. in [106]) for CMCs, it is particularly difficult to apply the physically based failure criterion for the investigated WHIPOX™ material or other CMCs. Furthermore, due to the fact that the Puck failure criteria were developed on the basic structure element of fiber reinforced polymeric composites, the UD-layer, identification of the failure mechanism through Puck method may not be suitable for CMCs with braided, wound or woven structure. For example, fiber failure (FF) instead of inter fiber fracture (IFF) can be observed in Carbon/Carbon ceramic composites with woven structures under transverse pressure, which is not expected when using the Puck analysis of failure mechanism [107]. The above mentioned physically based failure criteria are summarized in Table 2.4.

Table 2.4: Overview of some typical physically based failure criteria for composite with anisotropic properties

Physically based failure criteria			
Puck (2002)	$f_{Puck}(\sigma_n, \tau_{nt}, \tau_{n1}) = 1$	σ_n: normal stress on the fracture plane τ_{nt}: normal/transverse shear stress on the fracture plane τ_{n1}: normal/longitudinal shear stress on the fracture plane Tow basically independent failure: FF and IFF	[17]
Cuntze (2004)	$f_{Cuntze}(I_1, I_2, I_3, I_4, I_5) = 1$	I_{1-5}: Invariants of the transversally-isotropic UD-material Five different failure modes: two FF and three IFF	[105]
Dong (2014)	$f_{Dong}(\sigma_n, \tau_{nt}, \tau_{n1}, N, \theta) = 1$	Improvement of Puck criteria with consideration of layer thickness (N) and layer angles (θ)	[104]

Considerable effort has been put into the development of suitable models to reliably predict the failure of fiber reinforced composites. It should be noticed that the attempt to develop a universal failure criteria for all fiber composites with any desired laminate structures has resulted in a confusingly large number of failure criteria for the composite design engineer. No recommendation for a choice can be given because none of the criteria is substantiated by sufficient experiments. Furthermore, the commonly discussed failure criteria were designed for fiber reinforced polymer matrix and not for CMCs. The production and characterization of the representative UD-layer is a challenge for CMC materials. Therefore, instead of a real UD-layer, a virtual equivalent UD-layer was implemented in the Tsai-Wu quadratic failure criterion. The modified Tsai-Wu method with directional failure indices for the modeling of the mechanical properties of wound CMCs has been developed and is presented in this work.

2.3 Motivation and procedure

A key advantage of wound CMCs is their in-plane anisotropic material behavior, which strongly depends on the winding angle θ. Since the winding angle of each layer can be adjusted to any desired direction (from 0° to 90°) during the manufacturing process, the wound CMC components can be designed and optimized with stress-optimized fiber arrangement. Due to the variability of the fiber orientation and the complex material behavior, the design of CMC components, such as WHIPOX™, which represents one variant of an oxide fiber reinforced ceramic matrix composite, has to be supplemented with an advanced modeling approach for the prediction and assessment of the material properties of wound CMCs. In this way, experimental efforts towards mechanical characterization with any desired fiber alignment can be minimized to a great extent.

To find the mechanical constants of a laminate from the individual properties of the fiber and the matrix is a challenge for CMCs. This can be explained by the lack of required properties within the composite, especially the ones of matrix. The microstructure of the matrix, considering micro-cracks and specific matrix-porosity after the complex manufacture process, for example, sintering at temperature more than 1000 °C, is totally different from pure matrix properties and depends on the fiber orientation. Therefore, the use of the law of mixture with individual fiber and matrix (see section 2.2.2) is not possible. Two more concepts based on material homogenization techniques, either with the unit cell model or with the UD-layer model, can be used to build up geometrically-identical repetitive elements for the prediction of mechanical properties of the composites. The modeling approach with respective volume units at the micro- and mesostructure level has been discussed in section 2.2.2, which includes the mixed properties of the fiber, the matrix and the microstructure in a representative volume unit (RVU). Due to the requirement of a redefinition of varied fiber orientations (e.g. winding angle), the use of RVU is not efficient. Furthermore, the production and characterization of CMC UD-layers is also critical because of non-typical unhindered shrinkage of matrix transverse to the fibers during processing. This prevents the UD material from being considered as the representative material. Therefore, modeling of the mechanical properties and prediction of failure by classic failure criteria with UD-layers, which has been discussed in sections 2.2.2 and 2.2.3, cannot be directly implemented for wound CMCs.

The main aim of this dissertation is to discuss the characterization and modeling of the mechanical properties of wound oxide ceramic composites. The framework of this thesis involves the calculation and application of the properties derived from a virtual equivalent UD-layer used for the modeling of material behavior of wound CMCs. At first, the mechanical properties of the investigated wound oxide ceramic composite WHIPOX™ with different winding angles is characterized through in-plane mechanical testing. Then, the engineering properties of the equivalent UD-layer are calculated using an inverse operation of classic laminate theory and Cartesian transformation. After that, the values of maximum stress, maximum strain and the inelastic deformation of the virtual UD-layer are evaluated using the mechanical test results. Finally, through the stacking of these equivalent UD-layers with any desired layer structure (fiber orientation, thickness and number of layers), an equivalent layered composite is created. Its in-plane material behavior can be predicted and described with the help of modified CLT and modified Tsai-Wu failure criteria. It should be noted that the damage mechanism for the investigated material WHIPOX™ is beyond the scope of this study. Therefore, the initial cracks caused by first-ply-failure (FPF) and further distribution or development of cracks until last-ply-failure (LPF) are not discussed in this dissertation. Instead, the modeling approach with successive ply failure will be used for the determination of the stress and strain values of the material WHIPOX™. The reduction of the effective stiffness after the FPF will be discussed in section 7. Furthermore, a point-by-point modeling of material behavior up to its failure is not the aim of this study. Based on the analysis of different microstructures (see section 4.2), two models were used to describe composite behavior and to predict failure strength and strain. Firstly, the linear model was used for the group with linear elastic behavior up to its failure. Secondly, the bilinear/multi model was used for the group with non-linear behavior beyond the virtual yield stress, as well as for the situation with successive ply failures of laminate after the failure of first layer group. Moreover, by using the modified definition of the directional failure indices it is possible to predict which stress component is mainly responsible for failure. A detailed explanation of the procedure of modeling approaches will be configured and represented in section 7.

2.4 Specifications of the investigated topic

As mentioned in section 2.3, advanced modeling approaches with UD-layer properties are created for the evaluation and prediction of the material properties of wound CMC components. Compared to fiber reinforced polymer composites, the modeling of mechanical properties by direct implementation of CLT is very difficult for wound CMCs because of the challenge of the manufacture and the characterization of their representative UD-layer. Therefore, instead of using actual UD-layer, a virtual equivalent UD-layer was implemented in the proposed approach. As the core component of the modeling chain, the complete material properties of the equivalent UD-layer including elastic properties, strength, strain and inelastic deformation were calculated and evaluated. Through the stacking of these equivalent UD-layers with any desired fiber orientation, e.g. non-orthogonal, orthogonal and asymmetrical (off-axis), an equivalent layered composite is created and its material constants can be predicted.

The modeling approaches developed in this study may be applied to other fiber reinforced composites manufactured by the winding process. However, particular features of the investigated material have to be taken into consideration in order to predict mechanical properties with more accuracy. Based on the investigation results four distinctive features of material WHIPOX™ are implemented in the modeling approaches:

- Identification of inhomogeneity in the investigated plate through Non Destructive Inspection.
- Interaction between failure strength and strain through inelastic deformation.
- Division of material modeling groups based on the analysis of microstructure.
- Update of the analytical models for different batches with inhomogeneities created due to the manufacturing process.

A modified stiffness matrix with consideration of these particular features leads to a precise prediction of material properties. Detailed description of the modeling approach with consideration of the particular features of WHIPOX™ is introduced in the following sections.

3 Experimental Set-Up

3.1 Non Destructive Inspection Set-Up

Non Destructive Inspection (NDI) techniques are important tools used to provide the necessary information needed to understand the microstructure of materials and to identify the failure relevant defects that may occur during manufacturing. Air-coupled ultrasonic (US) testing and Lock-in thermography testing were used to investigate plates and micro-Computer Tomography (CT) to sample materials.

Air-coupled ultrasonic testing

Air-coupled ultrasonic testing is a non-destructive and contactless inspection technique. The test technique that was used here is a through transmission mode using a device from Second Wave System Corp. in Figure 3.1. The emitting transducer (emitter) above the test sample sends an ultrasound signal of approx. 180 kHz frequency which enters the sample and transmits through the thickness of the laminate structure. The attenuation of the signal is detected with the receiver at the lower end of the specimen. The ultrasound signal is absorbed, reflected or simply scattered. A strongly attenuated or nonexistent of signal is detected by the receiver if a material defect (pore and delamination) is encountered by the transducer couple. To scan the whole specimen, both transducer (emitter and receiver) move synchronously line by line with step size of 2 mm. More details about the physical background of air-coupled ultrasonic testing are described by Stößel [108].

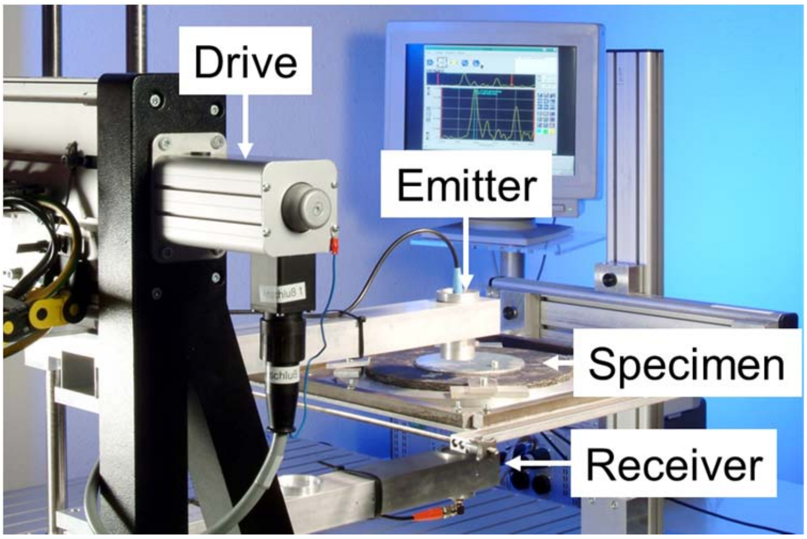

Figure 3.1: Set-up of air-coupled ultrasonic testing.

Lock-in thermography testing

Lock-in thermography inspection was used as a reference test method in order to confirm the results of the air-coupled ultrasonic measurements. Similar to air-coupled ultrasonic, lock-in thermography testing is a non-destructive and contactless inspection technique, which is based on the propagation and reflection of thermal waves. With modulated external heaters, e.g. synchronized halogen lamps from different directions (Figure 3.2), the surface of the specimen is illuminated. The generated thermal wave propagates through the CMC material and can be reflected by any kind of internal defects. The interference of incoming and reflected waves generate a harmonic oscillating radiation pattern on the specimen's surface which can be detected by an infrared camera over a certain period of time [109].

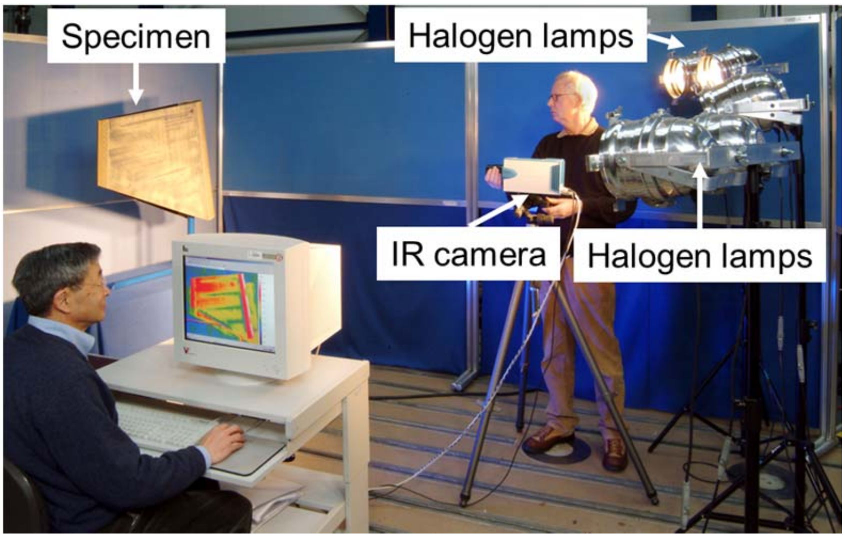

Figure 3.2: Set-up of lock-in thermography testing in a laboratory [109].

Micro-Computer Tomography

Micro Computed Tomography (μCT) scans of CMC samples have been performed using a high resolution μCT-System in Figure 3.3 (nanotom, GE Sensing & Inspection Technologies GmbH, Wunstorf, Germany) consisting of a microfocus x-ray tube (source) with a maximum of 180 kV accelerating voltage and a 12-bit flat panel detector with an active area of 2300 x 2300 pixels at 50 microns per pixel. The CT scans were realized at the x-ray parameters 80 kV/200 μA and at an exposure time 3000 ms. A voxel size of 1.16 μm could be achieved. During a complete rotation (360°) of the specimen, 2000 x-ray projections were acquired and afterwards reconstructed with a special algorithm known as Filtered Back Projection.

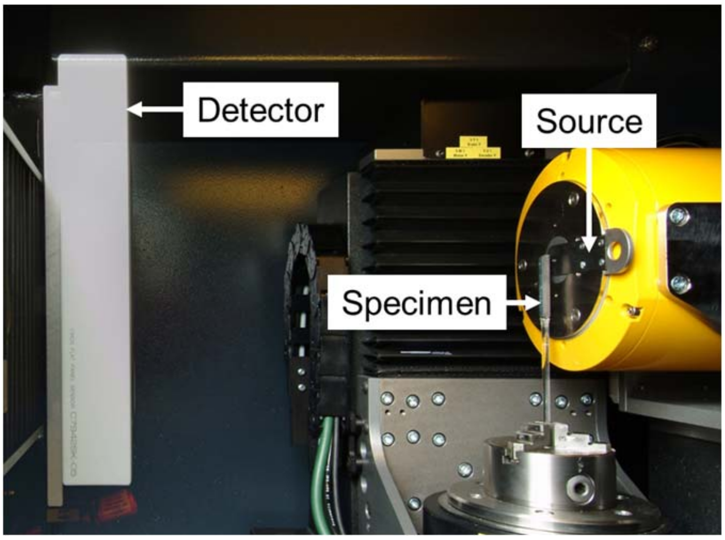

Figure 3.3: Set-up of Micro-Computer Tomography testing.

3.2 Fiber volume content and porosity

Fiber volume content (FVC) and porosity (e') are important elements in composite engineering used to assure quality of the laminate and component. Depending on different requirements, they could be varied within a certain range. A different FVC can be realized through varying amounts of wound fiber filaments or the thickness of layers. Porosity can be adjusted through different parameters of manufacturing or re-handling, e.g. the matrix porosity of WHIPOX™ is reduced through multiple infiltration of the as-sintered components [67]. On the other hand, the uncertainties from manufacturing result in variation in the FVC and porosity of the as processed CMCs. A manufacturing factor Ω which considers these uncertainties is introduced in section 5.5 to adapt the analytical. The determination of FVC and porosity is described in this section.

The FVC of the composites is calculated through the measurement of the initial weight of the fibers and the total volume of the finished component. It can be given by

$$FVC = \frac{\left({}^{W_F}/_{\rho_F}\right)}{V_C} 100 = \frac{\left({}^{W_F}/_{\rho_F}\right)}{(V_M + V_F)} 100$$

3.1

where W_F is the weight of the fibers, ρ_F is the density of the fibers, V_M is the volume of matrix, V_F is the volume of fibers and V_C is the total volume of the finished component.

The porosity of the composites is measured using Archimedes method [110]. The dry component is first weighed under normal atmospheric conditions and then weighed while submerged in water. Finally, it is weighed wet after being taken out of the water. Using the Archimedes principle the following equation used to determine porosity is obtained

$$e' = \frac{W_{wet} - W_{dry}}{W_{wet} - W_{water}} 100 \tag{3.2}$$

where W_{dry} is the weight of the component under normal atmospheric conditions, W_{water} is the component submerged in water and W_{wet} is the component after being taken out from water.

3.3 Mechanical testing

The essential material properties were determined and evaluated using mechanical in-plane testing. The samples for the experiments were cut from flat plates with varied fiber orientations. All the tests were performed at room temperature in air under quasi-static loading. Table 3.1 gives an overview of the performed mechanical tests and the investigated orientations relative to the specimen's longitudinal axis. The experiments were performed up to failure of sample on an universal testing machine (Zwick 1494) at a controlled cross head speed of 1 mm/min. The failure stress was calculated from the maximum load. For statistical confirmation at least three to six tensile, shear and compression samples per series were tested.

Table 3.1: Specimen geometry and dimensions, loading direction and the investigated orientations.

Test	Test geometries, dimensions and loading direction	Investigated orientations θ
Tensile	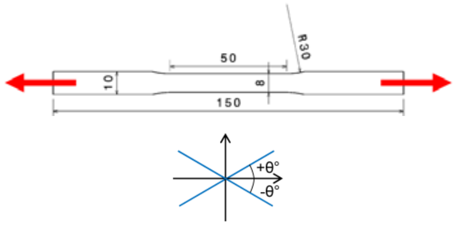	±3°/±87°[1], ±15°/±75°, ±22.5°/±67.5°, ±30°/±60°, ±45°, 0°/90° and 0°/60°
Compression	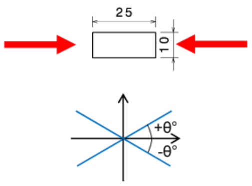	±15°/±75°, ±22.5°/±67.5°, ±30°/±60° ±45° and 0°/90°
Iosipescu -Shear	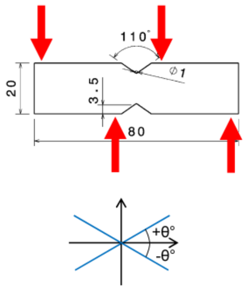	±3°/±87°[1], ±15°/±75°, ±22.5°/±67.5°, ±30°/±60° ±45° and 0°/90°

---

[1] The experimental tensile and shear tests for the investigated orientation ±3°/±87° in this study were conducted in Institute of Materials Research, German Aerospace Center Cologne.

Tensile specimens with the dimensions of 150*10(8)*5 mm^3 in Table 3.1 were produced with a reduced cross section in their gauge areas in order to prevent failure in the clamping section and to assure failure in their center regions. For the tensile test, the longitudinal and the transverse strains were measured with strain gauges. The experimental tensile tests for the investigated orientation ±3°/±87° in this study were conducted at Institute of Materials Research, German Aerospace Center Cologne. Strain gauges for longitudinal strains were glued for compression tests. During shear tests, the strain was evaluated using strain gauges in the +45° and in the -45° directions relative to the shear loading direction.

4 Investigated material WHIPOX

4.1 Processing of plate material

The investigated material WHIPOX™ is a continuous fiber reinforced oxide/oxide ceramic composite, which represents one variant of an oxide fiber reinforced ceramic matrix composite. It was developed and produced in the Institute of Materials Research, German Aerospace Center Cologne. WHIPOX™ components are manufactured by a computer controlled filament winding process with slurry infiltration of ceramic fiber bundles. The winding process allows a variable shape with regards to the core, thereby forming the component and the architecture of the fiber reinforcement. Figure 4.1a shows an initial stage of WHIPOX™ winding with angles of ±45°. A key advantage of wound CMCs is its in-plane anisotropic material behavior, which strongly depends on the winding angle $\pm\theta°$, defined between the longitudinal axis X of the wound preforms and the fiber tows direction (see Figure 4.1b).

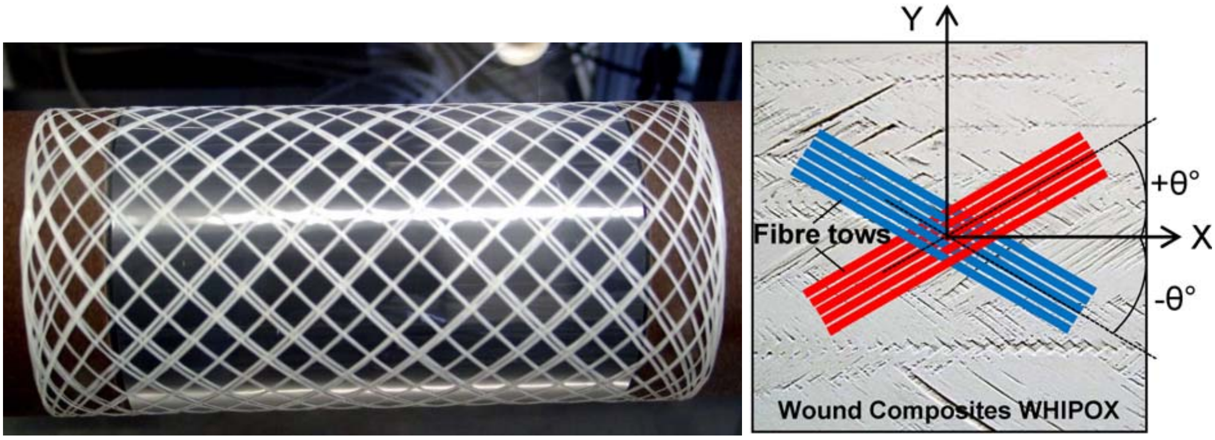

a)

b)

Figure 4.1: (a) Initial stage of winding process for WHIPOX™ material [111] and (b) WHIPOX™ plate with schematic representation of winding structure and winding angle $\pm\theta°$.

The manufacturing process for even plates is carried out in five steps: matrix infiltration of fiber tows, winding with angles defined to the cylindrical preform (green body), cutting and flat lay-up, drying and then sintering for about 1 h at 1300 °C [8, 23]. Although the green body is quite flexible in the wet state, the flattening and the forming of the laminate may lead to rearrangement of the filament bundles and therefore microstructural inhomogeneity. Moreover, the fiber crossing point, which is a typical feature of the winding process, creates local zones of increased porosity. The intermediate pore sizes of these zones and the periodic shifting of the crossing points across the laminate's thickness are strongly influenced by the winding angle and the thickness of the fiber rovings [23, 112]. A WHIPOX™ plate with a schematic representation of the winding structure and winding angle $\pm\theta°$ has been shown in Figure 4.1b The following Table 4.1

lists the material composition of WHIPOX™. The fiber volume content and the porosity fluctuate in a wide range. The individual values of the respective WHIPOX™ plates have been measured and summarized in section 6. The description of the measuring methods can be found in section 3.2.

Table 4.1: Material composition of WHIPOX™

Fiber type	Nextel™ 610 (Al_2O_3)
Fiber diameter	Approx. 12 µm
Fiber bundles	3000 DEN
Fiber Volume Content	34.0 - 43.0 %
Matrix	Al_2O_3
Porosity of composite	18.0 – 32.0 %

4.2 Microstructural investigation: shrinkage cracks

The highly porous matrix of WHIPOX™ (see Figure 4.2 and the value of porosity in Table 4.1) is aimed to a possible notch insensitive and damage tolerant behavior (see sections 2.1 and 2.2.1).

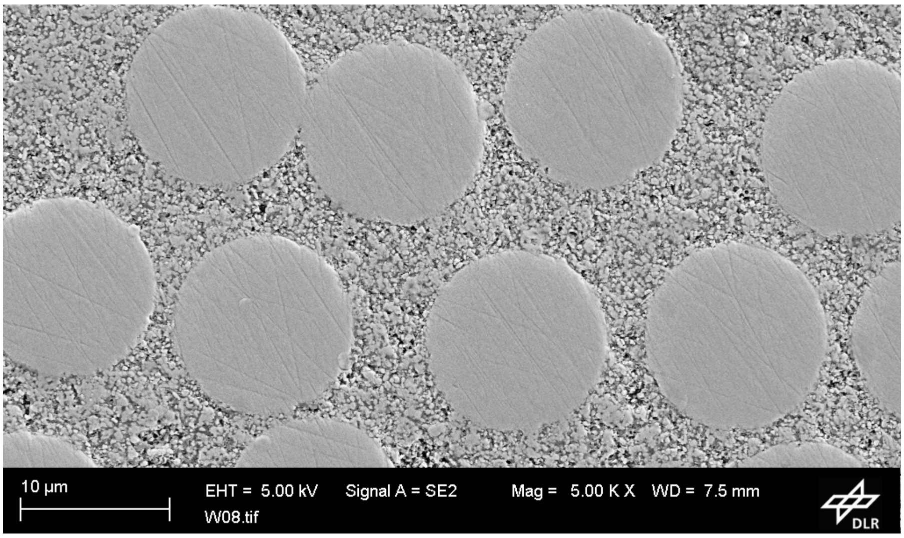

Figure 4.2: Microstructure of WHIPOX™ with fiber cross section and highly porous matrix.

Due to the microstructure of WHIPOX™, the calculation and modeling of material behavior encounter two challenges. The majority of WHIPOX™ structure has a layer-like design, however, the winding processing induces crossing lines where the fiber bundle crosses are to be found in WHIPOX™ structure (see the schematic representation of winding structure in Figure 4.1b). The relationship between the structure of these areas and the mechanical properties of WHIPOX™ is presented in [113]. In this work, an equivalent unidirectional layer with the mixed characteristics of layer-like design and crossing lines has been presented and used for the modeling of WHIPOX™ mechanical behavior. Another challenge of WHIPOX™ microstructure for modeling is that the experimentally determined transverse stiffness (perpendicular to the fiber direction) of the "quasi" UD-material (e.g. ±3°) does not reflect the circumstance in a layer structure with alternating fiber orientations. This is especially true for fiber architectures with increasingly vertical sloping of the two fiber directions, particularly 0°/90° (winding angle ±45°). The reason for this difference is the shrinkage cracks in the WHIPOX™ matrix. As mentioned before, during the sintering process of WHIPOX™, shrinkage of the matrix is blocked by the stiff fibers of adjacent layers. The maximum hindering of shrinkage is reached at high winding angles, e.g. ±45° (0°/90°) winding. This leads to cracking of the matrix during sintering and thus the reduction of Young's moduli in the transverse direction.

Micro Computed Tomography (µCT) was applied for the analysis of shrinkage cracks (section 3.1) for different winding angles and batches. Image processing techniques such as median filtering were applied to the CT volume images in order to reduce the noise. This step contributed to increase the reliability of image calibration based on gray scale methods. The purpose of the so called calibration or segmentation is to define both material and background allowing the quantitative analysis of CT data through the evaluation of features such as shrinkage cracks, open and closed porosity, inclusions, etc. The software VGStudioMax 2.2 (Volume graphics GmbH, Heidelberg, Germany) was used for this purpose. The following results have been published in [88].

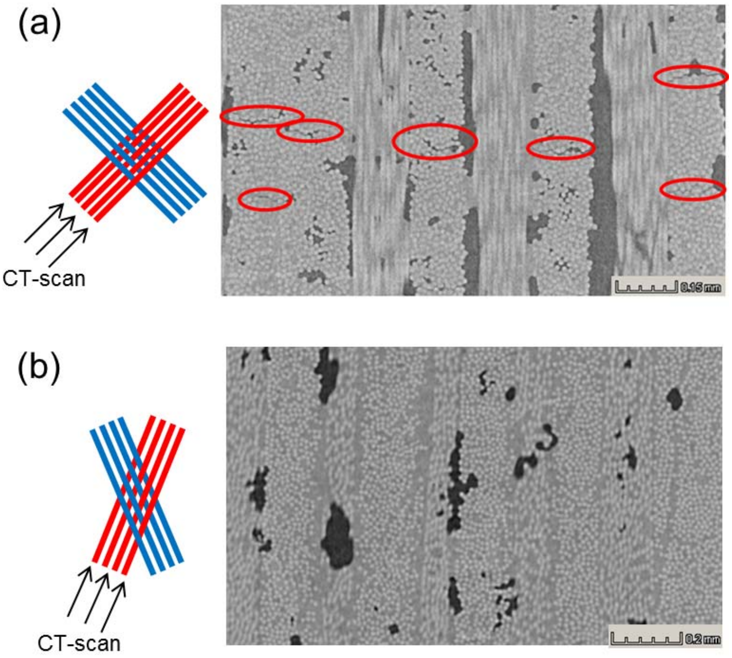

Figure 4.3: CT-images of the WHIPOX™ material with different fiber orientations: (a) Winding angle ±45°. Red marked areas show shrinkage cracks, which are perpendicular to the fiber's orientation; (b) Winding angle ±22.5. There are no shrinkage cracks visible.

In Figure 4.3a fiber parallel matrix cracks are clearly visible for the sample with a fiber orientation of ±45°. In order to quantify the difference, crack density will be calculated for different winding angles. In the case of ±45° the density of the cracks equals approx. 7 per mm^2. In contrast, no shrinkage cracks are visible for the ±22.5°-orientation in Figure 4.3b.

Further microstructure analysis results through µCT for different batches with the same winding angle of ±30° are shown in Figure 4.4. Samples from batch BT30 in Figure 4.4a have a similar distribution and crack density (approx. 6 per mm^2) as ±45° in Figure 4.3a. At the same time, no shrinkage cracks are observed in Figure 4.4c in batch WF30 with the same winding angle of ±30°. Sample BR30 with a crack density of approx. 3 pro mm^2 lies between these two cases as its CT-analysis shows in Figure 4.4b. WHIPOX™ material with the same fiber orientation (±30°) but a different microstructure can be explained as the effect of manufacturing scatter.

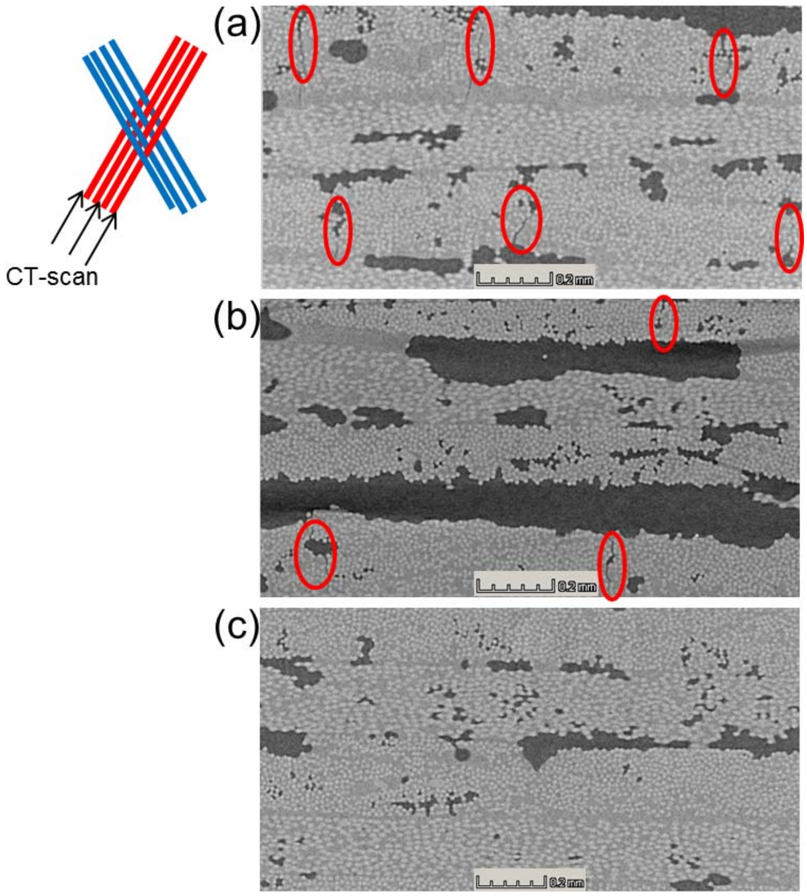

Figure 4.4: CT-images of WHIPOX™ material with a winding angle of ±30° from different batches: (a) sample BT30 similar crack density and distribution as ±45° in Figure 4.3a; (b) sample BR30 with a crack density of approx. 3 pro mm^2; (c) sample WF30 with no shrinkage racks.

Figure 4.5 shows the relationship of crack density and winding angle (from 0° to 45° because of the symmetry). It should be noticed that the calculation of crack density is a quantitative binary approach to estimate, whether the shrinkage cracks are existent or not. Based on the microstructure analysis of matrix cracks, no monotonic increase of the crack density in relation to winding angle can be observed. A transition line between the matrix with and without cracks can be found in the winding angle of ±30°. No cracks were observed for smaller winding angles. WHIPOX™ with winding angles of ±30° through ±45 showed similar crack distributions. Therefore, as one of the particular features of the investigated WHIPOX™, the modeling of the properties of WHIPOX™ was divided into two classes: WHIPOX™ with matrix cracks and WHIPOX™ without matrix cracks.

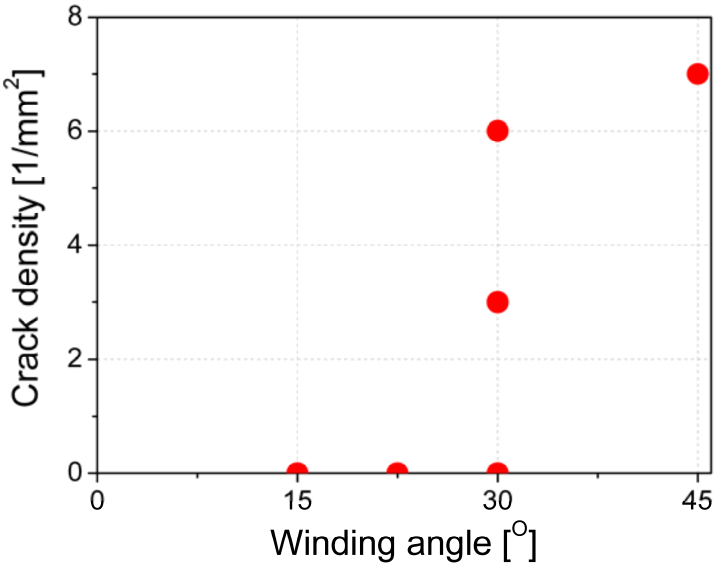

Figure 4.5: Crack density of different winding angles.

5 Modeling Approach

For the modeling of mechanical behavior, detailed description of the advanced modeling approach with and without particular features of WHIPOX™ are introduced in this section.

5.1 Classical Laminate Theory

The Classical Laminate Theory (CLT), which is based on the engineering constants of individual UD-layers and the stacking sequence, has been discussed in a number of studies and has been successfully adapted for composites with polymeric matrices for the calculation of material properties (e.g. compiled in [114]). All issues which are necessary for the modeling of the in-plane mechanical behavior of CMCs are described in the following text.

For the application of CLT on thin plies and boards, some reasonably accurate assumptions have been made: the material properties of the matrix are homogeneous and isotropic on a macroscopic scale; no relative movement between the fiber, the matrix and the individual layers exists; the residual stresses are irrelevant; the material exhibits linear elastic material behavior under in-plane stress conditions. In this case, the displacement in the plane is assumed to be a linear function of the layer thickness and the cross section remains flat. Accordingly, the shear strain ε_{yz} and ε_{xz} must be set to zero. With these prerequisites, the performance of a laminate can be reduced to two-dimensional behavior of the middle surface of the layer.

For further consideration, the strain ε_i and ε_{ij} with $i, j = x, y, xy$ are first calculated in three-dimensional status through kinematic equations [114]:

$$\varepsilon_x = \frac{\partial u}{\partial x}$$

5.1

$$\varepsilon_y = \frac{\partial v}{\partial y}$$

5.2

$$\varepsilon_z = \frac{\partial w}{\partial z}$$

5.3

$$\varepsilon_{xy} = \frac{1}{2}\left(\frac{\partial u}{\partial y} + \frac{\partial v}{\partial x}\right)$$

5.4

$$\varepsilon_{yz} = \frac{1}{2}\left(\frac{\partial v}{\partial z} + \frac{\partial w}{\partial y}\right)$$

5.5

$$\varepsilon_{xz} = \frac{1}{2}\left(\frac{\partial u}{\partial z} + \frac{\partial w}{\partial x}\right)$$

5.6

where u, v and w present the displacements in x, y and z-direction, respectively (see Figure 5.2). The displacement in the plane is assumed to be a linear function of the thickness, applies to the displacements u and v [114]:

$$u = u^0(x,y) + zf_1(x,y)$$

5.7

$$v = v^0(x,y) + zf_2(x,y)$$

5.8

where u^0 and v^0 are the displacements of the middle surface of the layer. Because the strains ε_{yz} and ε_{xz} must be set to zero, the functions $f_1(x,y)$ and $f_2(x,y)$ can be expressed through insertion of equations 5.7 and 5.8 into equations 5.5 and 5.6 as [114]:

$$\varepsilon_{xz} = \frac{1}{2}\left(f_1(x,y) + \frac{\partial w}{\partial x}\right) = 0$$

5.9

$$\varepsilon_{yz} = \frac{1}{2}\left(f_2(x,y) + \frac{\partial w}{\partial y}\right) = 0$$

5.10

$$f_1(x,y) = -\frac{\partial w}{\partial x}$$

5.11

$$f_2(x,y) = -\frac{\partial w}{\partial y}$$

5.12

The following prerequisites are used: firstly, the strain ε_z in thickness direction is negligible for the thin plies; secondly, the vertical displacement does not change within the plate thickness. Then the in-plane strain for small distortion can be calculated [114]:

$$\varepsilon_x = \frac{\partial u^0}{\partial x} - z\frac{\partial^2 w}{\partial x^2}$$

5.13

$$\varepsilon_y = \frac{\partial v^0}{\partial y} - z\frac{\partial^2 w}{\partial y^2}$$

5.14

$$\varepsilon_{xy} = \frac{1}{2}\left(\frac{\partial u^0}{\partial y} + \frac{\partial v^0}{\partial x}\right) - z\frac{\partial^2 w}{\partial xy}$$

5.15

By using the $\kappa_x = -\frac{\partial^2 w}{\partial x^2}$, $\kappa_y = -\frac{\partial^2 w}{\partial y^2}$ and $\kappa_{xy} = -\frac{\partial^2 w}{\partial xy}$, which present the curvature of the plate, equations 5.13 to 5.15 can be described in matrix 5.16 [114]:

$$\begin{bmatrix} \varepsilon_x \\ \varepsilon_y \\ \varepsilon_{xy} \end{bmatrix} = \begin{bmatrix} \varepsilon_x^0 \\ \varepsilon_y^0 \\ \varepsilon_{xy}^0 \end{bmatrix} + z\begin{bmatrix} \kappa_x \\ \kappa_y \\ \kappa_{xy} \end{bmatrix}$$

5.16

where ε_x^0, ε_y^0 and ε_{xy}^0 are the displacements of the middle surface of the layer in different direction.

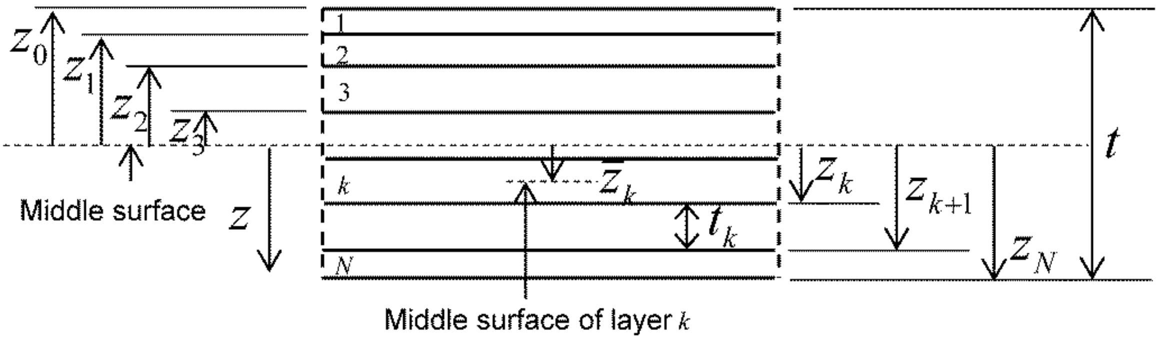

Figure 5.1: Geometry of laminate plate with UD-layer: UD-layer is numbered from 1 to N; Z_k is the distance between the middle surface of the laminate to the top or bottom of each layer; $\overline{Z_k}$ is the distance between the middle surface of the laminate to the middle surface of each layer; t_k is the thickness of each layer and $t_k = Z_{k+1} - Z_k$.

The last mentioned connection between strain, displacements and curvature can be applied for each ply within a composite made of UD-layers (shown in Figure 5.1 with each layer having a thickness of t_k). The thickness of the whole laminate h can be calculated using:

$$h = \sum_{k=1}^{n} t_k$$

5.17

Using the assumption that no displacement between individual layers exists, the strains across the thickness stay constant. The stress and strain of the individual layer k in Figure 5.1 can be related with help of the well-known Hooke's law:

$$\sigma_i = \bar{Q}_{ij}(\varepsilon_j^0 + z\kappa_j)$$

5.18

where $\bar{Q}_{ij}$ indicated the stiffness of each layer.

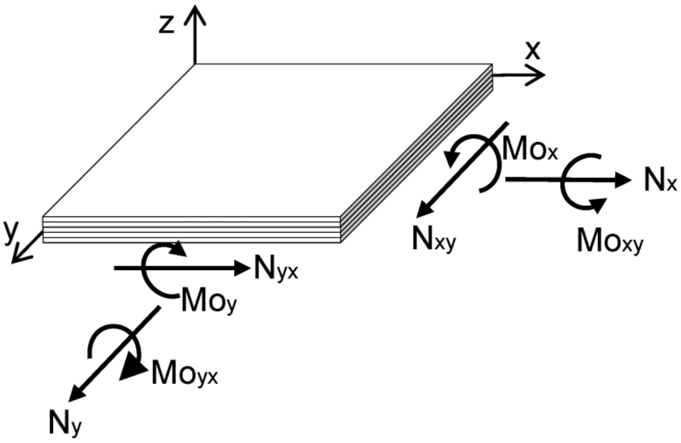

Figure 5.2: The in-plane forces N_{ij} and moment Mo_{ij} on a flat laminate.

Through the integration of stress into the global in-plane coordinate system $x - y$ (Figure 5.2) of each UD-layer, the resultant force N_{ij} and moment Mo_{ij} can be formulated using equations 5.19 and 5.20:

$$N_{x,y,xy} = \int_{-h/2}^{h/2} (\sigma_x, \sigma_y, \sigma_{xy}) dz$$

5.19

$$Mo_{x,y,xy} = \int_{-h/2}^{h/2} (\sigma_x, \sigma_y, \sigma_{xy}) z dz$$

5.20

where σ = $(\sigma_x, \sigma_y, \sigma_{xy})$ are average in-plane stresses.

With the help of the stiffness matrix $\left[\bar{Q}_{ij}\right]$ for a multilayer laminate (Figure 5.1), the relationship between strain $\{\varepsilon^0\}$, curvature $\{\kappa\}$, resultant force $\left[N_{x,y,xy}\right]$ and moment $\left[Mo_{x,y,xy}\right]$ under in-plane loading can be described with equation 5.21 [114]:

$$\begin{Bmatrix} N_x \\ N_y \\ N_{xy} \\ Mo_x \\ Mo_y \\ Mo_{xy} \end{Bmatrix} = f\left(\left[\bar{Q}_{ij}\right], \varepsilon^0, \kappa\right) = \begin{bmatrix} \begin{bmatrix} S_{11} & S_{12} & S_{16} \\ S_{21} & S_{22} & S_{26} \\ S_{61} & S_{62} & S_{66} \end{bmatrix} & \begin{bmatrix} C_{11} & C_{12} & C_{16} \\ C_{21} & C_{22} & C_{26} \\ C_{61} & C_{62} & C_{66} \end{bmatrix} \\ \begin{bmatrix} C_{11} & C_{12} & C_{16} \\ C_{21} & C_{22} & C_{26} \\ C_{61} & C_{62} & C_{66} \end{bmatrix} & \begin{bmatrix} B_{11} & B_{12} & B_{16} \\ B_{21} & B_{22} & B_{26} \\ B_{61} & B_{62} & B_{66} \end{bmatrix} \end{bmatrix} \begin{Bmatrix} \varepsilon_x^0 \\ \varepsilon_y^0 \\ \varepsilon_y^0 \\ \kappa_x \\ \kappa_y \\ \kappa_{xy} \end{Bmatrix}$$

5.21

The above relation can be reduced as follows:

$$\begin{Bmatrix} N_{ij} \\ Mo_{ij} \end{Bmatrix} = \begin{bmatrix} \left[S_{ij}\right] & \left[C_{ij}\right] \\ \left[C_{ij}\right] & \left[B_{ij}\right] \end{bmatrix} \begin{Bmatrix} \left[\varepsilon_{ij}^0\right] \\ \left[\kappa_{ij}\right] \end{Bmatrix}$$

5.22

The individual in-plane sub-matrices of $\left[\bar{Q}_{ij}\right]$ are: strain stiffness $\left[S_{ij}\right]$, coupling stiffness$\left[C_{ij}\right]$ and bending stiffness $\left[B_{ij}\right]$. They were determined through the stiffness matrix of a single UD-layer with a thickness of t_k [114]:

$$S_{ij} = \sum_{k=1}^{N} (\bar{Q}_{ij})_k t_k$$

5.23

$$C_{ij} = \sum_{k=1}^{N} (\bar{Q}_{ij})_k t_k \bar{Z}_k$$

5.24

$$B_{ij} = \sum_{k=1}^{N} (\bar{Q}_{ij})_k (t_k {\bar{Z}_k}^2 + {t_k}^3/12)$$

5.25

The strains and curvatures can be expressed in terms of forces and moments with the inverse SCD matrix:

$$\begin{Bmatrix} \left[\varepsilon_{ij}^0\right] \\ \left[\kappa_{ij}\right] \end{Bmatrix} = \begin{bmatrix} \left[s_{ij}\right] & \left[c_{ij}\right] \\ \left[c_{ij}\right] & \left[b_{ij}\right] \end{bmatrix} \begin{Bmatrix} N_{ij} \\ Mo_{ij} \end{Bmatrix}$$

5.26

where,

$$\begin{bmatrix} [s_{ij}] & [c_{ij}] \\ [c_{ij}] & [b_{ij}] \end{bmatrix} = \begin{bmatrix} [S_{ij}] & [C_{ij}] \\ [C_{ij}] & [B_{ij}] \end{bmatrix}^{-1}$$

5.27

In the case of a laminate with a symmetric fiber orientation under in-plane resultant force $[N_{x,y,xy}]$, there is no coupling stiffness $[C_{ij}]$ and bending stiffness $[B_{ij}]$ and the $S_{ij} = S_{ji}$ in the equation 5.21. The SCD matrix can be reduced to:

$$\begin{Bmatrix} N_x \\ N_y \\ N_{xy} \end{Bmatrix} = \begin{bmatrix} S_{11} & S_{12} & 0 \\ S_{21} & S_{22} & 0 \\ 0 & 0 & S_{66} \end{bmatrix} \begin{Bmatrix} \varepsilon_x^0 \\ \varepsilon_y^0 \\ \varepsilon_y^0 \end{Bmatrix}$$

5.28

With inverse strain stiffness $[s_{ij}]$ the effective engineering constants of laminate in x-y coordinate system are evaluated by [114]:

$$E_x = \frac{1}{s_{11}t}$$

5.29

$$E_y = \frac{1}{s_{22}t}$$

5.30

$$G_{xy} = \frac{1}{s_{66}t}$$

5.31

$$\nu_{xy} = -\frac{s_{12}}{s_{11}}$$

5.32

where E_x and E_y are the effective Young's moduli of laminate in the x and y-directions; ν_{xy} is the effective Poisson's ratios and G_{xy} is the effective shear modulus. In this case, only four effective composite constants are independent, ν_{yx} can be calculated from the equation $\nu_{yx}E_x = \nu_{xy}E_y$.

5.2 Inverse approach of Classic Laminate Theory

As mentioned above, an inverse approach to classic laminate theory using an equivalent UD-layer is presented in this section.

Firstly, each single, non-orthogonal wound-double-layer with winding angle $\pm\theta°$ can be replaced by two superimposed equivalent UD-layers with angle $+\theta°$and $-\theta°$ in Figure 5.3a. The winding angle $\pm\theta°$ was originally defined between the longitudinal axis X of the WHIPOX™ preforms and the fiber tows direction in Figure 4.1b. These equivalent UD-layers were defined with half the thickness of the CMC wound-double-layer and identical mechanical properties in the local coordinate system with 1-axis parallel to the fiber direction and 2-axis perpendicular to the fiber (Figure 5.3a). Due to the fact that the fiber and matrix properties are unknown, the elastic properties of the equivalent UD-layer are calculated using the inverse operation of CLT and the Cartesian transformation. Through the stacking of equivalent UD-layers with the orientation $\pm\theta°$, an equivalent layered composite (Figure 5.3b) is designed which has orthotropic properties. Finally, the equivalent UD-layers allow for the modeling of any other fiber orientation and stacking sequence.

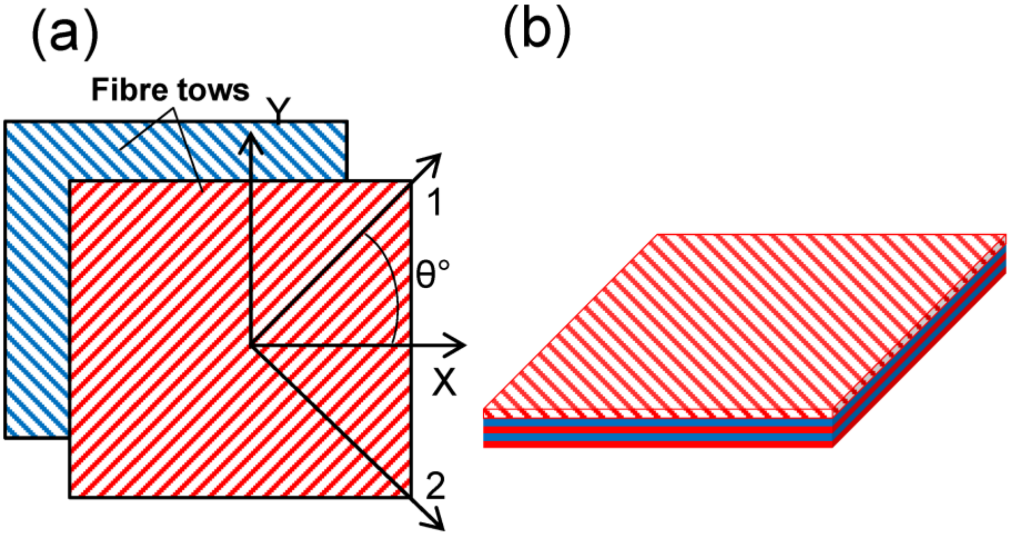

Figure 5.3: (a) Equivalent UD-layers with the local coordinate system, 1-axis in fiber direction and 2-axis in perpendicular direction; (b) Equivalent composite structure with UD-layers.

With the adaption of winding angle $\theta°$ to the inverse matrix $[Ma]^{-1}$, the material stiffness $[Q_{ij}]$ in the local coordinate system is derived from the transformation of the reduced stiffness matrix $[\bar{Q}_{ij}]$ along the global coordinate system [114]:

$$\begin{bmatrix} Q_{11} \\ Q_{22} \\ Q_{12} \\ Q_{66} \end{bmatrix} = [Ma]^{-1} \begin{bmatrix} \bar{Q}_{11} \\ \bar{Q}_{22} \\ \bar{Q}_{12} \\ \bar{Q}_{66} \end{bmatrix}$$

5.33

where $[Ma]$ is the Cartesian transformation matrix and is defined as:

$$[Ma] = \begin{bmatrix} m^4 & n^4 & 2m^2n^2 & 4m^2n^2 \\ n^4 & m^4 & 2m^2n^2 & 4m^2n^2 \\ m^2n^2 & m^2n^2 & m^4+n^4 & -4m^2n^2 \\ m^2n^2 & m^2n^2 & -2m^2n^2 & (m^2-n^2)^2 \end{bmatrix}$$

5.34

where $m = cos\theta$ and $n = sin\theta$.

The determination of the reduced stiffness matrix $[\bar{Q}_{ij}]$ requires the in-plane elastic properties of a laminated composite in the global coordinate system. The terms of $[Q_{ij}]$ can be calculated from the following equations [114]:

$$\bar{Q}_{11} = \frac{E_x}{1 - v_{xy}^2 \frac{E_y}{E_x}}$$

5.35

$$\bar{Q}_{22} = \frac{E_y}{1 - v_{xy}^2 \frac{E_y}{E_x}}$$

5.36

$$\bar{Q}_{12} = \frac{E_y v_{xy}}{1 - v_{xy}^2 \frac{E_y}{E_x}}$$

5.37

$$\bar{Q}_{66} = G_{xy}$$

5.38

Moving on to the elastic constants of the equivalent UD-layer: the Young's modulus in fiber direction E_1 and perpendicular direction E_2; the Poisson's ratio v_{12}; and the shear modulus G_{12}, can be calculated with the local material stiffness $[Q_{ij}]$ as follows:

$$E_1 = Q_{11} - \frac{Q_{12}^2}{Q_{22}}$$

5.39

$$E_2 = Q_{22} - \frac{Q_{12}^2}{Q_{11}}$$

5.40

$$v_{12} = \frac{Q_{12}}{Q_{22}}$$

5.41

$$G_{12} = Q_{66}$$

5.42

Finally, through the stacking of equivalent UD-layers (Figure 5.3a) with the calculated elastic properties (equation 5.39 to 5.42) and any desired fiber orientation an equivalent layered composite (Figure 5.3b) is created. Its material constants can be predicted with the help of the stiffness matrix $[\bar{Q}_{ij}]$ and sub-matrices strain stiffness $[S_{ij}]$, coupling stiffness $[C_{ij}]$ and bending stiffness $[B_{ij}]$ from equation 5.21 to 5.25.

5.3 Modified Tsai-Wu failure criterion

For the prediction of failure mechanism of composite structures under multi-axial loading conditions, many different failure criteria have been developed and published but no recommendation for a choice can be given, because none of the criteria is proved by sufficient experiments (see section 2.2.3). On the one hand, due to the lack of recommendations for the suitable material parameters (e.g. Puck criterion in [106]) for CMCs, it is particularly difficult to apply the physically based criteria for the investigated WHIPOX™ material or other CMCs (see section 2.2.3). On the other hand, the Tsai-Wu failure criterion has been improved by using the modified definition of the directional failure indices by the work of Paepegem in [18], which allows to predict which stress component is mainly responsible for the failure. Therefore, a modified Tsai-Wu quadratic failure criterion with implementation of virtual equivalent UD-layers for the modeling of the mechanical properties of wound oxide ceramic composites has been developed in this study and is presented in this section.

5.3.1 Tsai-Wu failure criterion in stress space

The failure surface in the stress space of the Tsai-Wu failure criterion can be described as [16]:

$$F_i \sigma_i + F_{ij} \sigma_i \sigma_j = 1$$

5.43

where $i, j = 1,2, \dots ,6$; F_i and F_{ij} are strength tensors of the second and fourth rank, respectively.

In the one-dimensional case, the Tsai-Wu strength failure criterion can be written as:

$$F_1 \sigma_1 + F_{11} \sigma_1^2 = 1$$

5.44

In its two-dimensional formulation, the general Tsai-Wu quadratic criterion in stress space can be written as:

$$F_1 \sigma_1 + F_2 \sigma_2 + F_{11} \sigma_1^2 + F_{22} \sigma_2^2 + F_{66} \tau_{12}^2 + 2F_{12} \sigma_1 \sigma_2 = 1$$

5.45

The strength parameters F_1 to F_{66} from equations 5.44 and 5.45 are related to the engineering strengths of UD-layer under uniaxial loading [16]. For a unidirectional lamina with longitudinal tensile strength σ_1^T and compressive strength σ_1^C and no transverse and shear loading applied, the equation 5.45 can be reduced to:

$$F_1\sigma_1^T + F_{11}(\sigma_1^T)^2 = 1$$

5.46

$$F_1\sigma_1^C + F_{11}(\sigma_1^C)^2 = 1$$

5.47

From the above equations 5.46 and 5.47, the values for F_1 and $F_{11}$are obtained as:

$$F_1 = \frac{1}{\sigma_1^T} - \frac{1}{\sigma_1^C}$$

5.48

$$F_{11} = \frac{1}{\sigma_1^T\sigma_1^C}$$

5.49

The equation 5.45 can be likewise treated as a unidirectional lamina with a transverse tensile strength of σ_2^T and a compressive strength of σ_2^C, without longitudinal and shear loading:

$$F_2\sigma_2^T + F_{22}(\sigma_2^T)^2 = 1$$

5.50

$$F_2\sigma_2^C + F_{22}(\sigma_2^C)^2 = 1$$

5.51

The values for F_2 and F_{22} are obtained from the above equations:

$$F_2 = \frac{1}{\sigma_2^T} - \frac{1}{\sigma_2^C}$$

5.52

$$F_{22} = \frac{1}{\sigma_2^T\sigma_2^C}$$

5.53

Similar steps are followed for the evaluation of F_{66} with its value being related to the shear strength of unidirectional lamina τ_{12}:

$$F_{66} = \frac{1}{(\tau_{12})^2}$$

5.54

It is important to realize that the concept of directional failure parameters does not only depend on the chosen failure criterion. Similar concepts could be defined for failure criteria other than the Tsai-Wu criterion. Generally a failure envelope must be closed in order to prevent infinite strength values. In the case of Tsai-Wu strength criterion an interaction term F_{12} is bound to ensure that the failure envelope is closed. The value of F_{12} has to be determined through the bi-axial tensile test. When equal tensile loads and no shear loads are applied along the two principal material axes in an unidirectional lamina, F_{12} is obtained via:

$$F_{12} = \frac{1}{2}\left[\frac{1}{(\sigma_{bi})^2} - \frac{F_1 + F_2}{\sigma_{bi}} - (F_{11} + F_{22})\right]$$

5.55

where σ_{bi} is the failure load during the bi-axial tensile test. Because of the great difficulty in performing combined stress tests, some empirical estimations of the F_{12} value have been proposed for different failure criterion and summarized in [115], e.g.:

Tsai-Hill failure criterion:

$$F_{12} = -\frac{1}{2(\sigma_1^T)^2} = -\frac{1}{2(\sigma_1^C)^2}$$

5.56

Hoffman failure criterion:

$$F_{12} = -\frac{1}{2\sigma_1^T \sigma_1^C}$$

5.57

An empirical model for the determination of the value of F_{12} has been given by Hahn and Tsai in [116]:

$$F_{12} = -\frac{\sqrt{F_{11}F_{22}}}{2} = -\frac{1}{2\sqrt{\sigma_1^T(|\sigma_1^C|)\sigma_2^T(|\sigma_2^C|)}}$$

5.58

The effect of F_{12} on the Tsai-Wu failure envelopes has been studied in the following research [117-120]. In the basic paper on Tsai-Wu failure criterion F_{12} may be considered to be zero if it falls in the range $\pm 6 \cdot 10^{-5}$ based on the test results of unidirectional graphite/epoxy samples [121]. According to the studies of Narayanaswami and Adelman [122], the interaction parameter of composite material is small and can be often taken to zero. This conclusion drawn from the negligible interaction parameter has been generally accepted as being applicable to different composite materials [123-125]. In the case of the investigated

WHIPOX™ material, the interaction term F_{12} has been set to zero due to the lack of the possibility of production of real unidirectional layer and bi-axial tensile testing. Nevertheless, the sensitivity of F_{12} to the shape of the Tsai-Wu failure envelope of WHIPOX™ will be discussed in section 8.1. With the above in mind the equation 5.45 can be reduced to:

$$F_1\sigma_1 + F_2\sigma_2 + F_{11}\sigma_1^2 + F_{22}\sigma_2^2 + F_{66}\tau_{12}^2 = 1$$

5.59

The original form of Tsai-Wu failure criterion with equation 5.43 could only predict the final failure moment of the material. In order to analyze the progressive failure mode, a strength ratio R has been defined in [118]. The ratio R is a linear scaling factor and related to the loading applied from any state of stress:

$$R\sigma^{app} = \sigma^{max}$$

5.60

where σ^{app} is the current applied stress and σ^{max} is the strength value of the material. Obviously, failure occurs when $R = 1$. By substituting the maximum stress components $\sigma_i = \sigma_i^{max}$ and $\sigma_j = \sigma_j^{max}$ with the relationship between applied stress and strength to the original Tsai-Wu failure equation 5.43, the value of the ratio R can be easily determined with the quadratic equation [118]:

$$\left(F_{ij}\sigma_i\sigma_j\right)R^2 + (F_i\sigma_i)R - 1 = 0$$

5.61

Upon solving the quadratic equation 5.62:

$$aR^2 + bR - 1 = 0$$

5.62

The values of $a = F_{ij}\sigma_i\sigma_j$ and $b = F_i\sigma_i$ and the ratio R can be given by:

$$R = \frac{-b \pm \sqrt{b^2 + 4a}}{2a}$$

5.63

The positive root of equation 5.63 provides the value of the strength ratio R which can be applied to any kind and state of load.

In addition, a reciprocal failure index k was defined as being the inverse value of R with $k = 1/R$ [118]. The original Tsai-Wu form can be described as:

$$\left(F_{ij}\sigma_i\sigma_j\right)\left(\frac{1}{k}\right)^2 + (F_i\sigma_i)\left(\frac{1}{k}\right) - 1 = 0$$

5.64

5.3.2 Tsai-Wu failure criterion in strain space

Compared to the stress space, the Tsai-Wu failure criterion in strain space is more convenient because the distribution of strain across the thickness of a laminate is idealized as being constant. Therefore, elongation of any ply in a laminate can be easily determined through applying the failure criterion in the strain space. In the case of linear elastic behavior up to failure, the one-to-one correspondence between stress and strain is always available. The stress value at each state of load can have one and only one corresponding strain. For an orthotropic material, Tsai-Wu stress failure criterion in equations 5.43 can be represented in strain components as [126]:

$$F_i\sigma_i + F_{ij}\sigma_i\sigma_j = F_i[Q_{ik}\varepsilon_k] + F_{ij}[Q_{ik}\varepsilon_k][Q_{jl}\varepsilon_l] = [F_iQ_{ik}]\varepsilon_k + [F_{ij}Q_{ik}Q_{jl}]\varepsilon_k\varepsilon_l = G_k\varepsilon_k + G_{kl}\varepsilon_k\varepsilon_l = 1$$

5.65

where G_k and $G_{kl}$are strain tensors of the second and fourth rank, respectively, and can be determined [126]:

$$G_k = F_iQ_{ik}$$

5.66

$$G_{kl} = F_{ij}Q_{ik}Q_{jl}$$

5.67

The same strength ratio R and failure index k can be determined from the quadratic criterion in strain space [126]:

$$(G_{kl}\varepsilon_k\varepsilon_l)R^2 + (G_k\varepsilon_k)R - 1 = 0$$

5.68

$$(G_{kl}\varepsilon_k\varepsilon_l)\left(\frac{1}{k}\right)^2 + (G_k\varepsilon_l)\left(\frac{1}{k}\right) - 1 = 0$$

5.69

On the other hand, as it is the case of the non-linear elastic behavior up to failure, stress and strain do not correspond directly to initial material stiffness matrix Q_{ij}. Since the stiffness values are usually degraded after a certain load state for non-linear behavior, any calculated strain values using initial material stiffness would be underestimated. In order to model the inelastic strain, an inelastic deformation factor Δ as one of the particular features of investigated material WHIPOX™ is introduced in section 5.4.

5.3.3 Successive ply failures

Whether in stress space or in strain space, the Tsai-Wu quadratic failure criterion is applied to each single ply within a whole laminate. It is quite common for the plies having different values of strength or elongation even under the same load, because e.g. each fiber orientation to the loading axis of each layer is different from one another. In this case, the ply with the lowest strength ratio R or the highest failure index k fails first, which is first-ply-failure (FPF). Successive ply failure will proceed until the highest strength ratio R or the lowest failure index k is reached, thus, last-ply-failure (LPF). As indicated in section 2.3 "Motivation and procedure", the damage mechanism for the investigated material WHIPOX™ is beyond the scope of this study. The initial crack by FPF and further distribution/development of cracks of the state LPF are not topics of this dissertation. Modeling with successive ply failure will be used for the determination of stress and strain values at different loading states, which is very useful for the design of the component. The FPF can be recommended for the limitation of load and LPF for the ultimate failure of component.

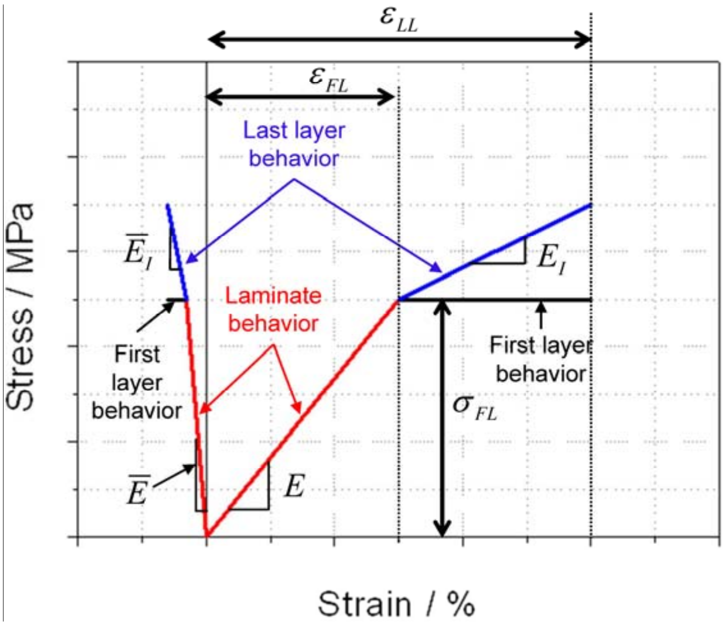

Figure 5.4: Successive ply failures in a laminate of two ply groups with different fiber orientations.

Failure of a ply or ply group will change the internal stress distribution of the laminate and the effective stiffness of the laminate will reduce. A successive ply failure of two different ply groups in a laminate under tensile loading is shown in Figure 5.4 as an example. Linear elastic behavior up to first-ply-failure is assumed by the initial behavior of laminate (non-linear behavior is presented in section 5.4). With this assumption, E and $\bar{E}$ are the initial stiffnesses of laminate in tensile longitudinal and transverse directions, respectively. After FPF, as long as the ply is still embedded in the laminate it will continue to take the strain but no additional stress (first layer behavior in Figure 5.4). In other words, the stiffness of the failed ply or ply group is reduced to zero while the stress is not zero. σ_{FL} is the strength and ε_{FL} the elongation of the first layer. After obtaining the FPF, the initial stiffnesses are reduced to E_I and $\overline{E_I}$ in longitudinal and transverse directions, respectively. The value of E_I and $\overline{E_I}$ can be calculated with the Classical Laminate Theory (section 5.1) after the assumption is made that the failure of the first ply had no effect on the remaining plies: the remaining plies are left without degradation because of the failure of first plies. The laminate fails completely when LPF occurs with the ultimate strain of last layer ε_{LL} (Figure 5.4).

To overlook the possibility of crack development in the remaining plies after FPF is not a conservative modeling approach. However, it is reasonable to assume that the ultimate strain of the ply is not dependent on the laminate system. In order to prove the applicability of the above modeling approach for the investigated WHIPOX™, two laminates with fiber orientations of 0°/90° and 0°/60° were examined under tensile loading. According to the approach presented in this section, the value of strength σ_{FL} and of elongation ε_{FL} of FPF should be different, because the strength ratio R and failure index k are not identical concerning the layer groups with diffenrent orientation 90° and 60°. However, the ultimate strain ε_{LL} of two laminates (0°/90° and 0°/60°) is identical due to the common orientation of 0° during LPF. The test results and comparisons with the calculated values of these two laminates are shown later.

5.3.4 Directional failure indices

By using the strength ratio R and the successive ply failure approach, the failure factor of any state of load can be calculated. However, the original Tsai-Wu quadratic failure criteria do not differentiate between different failure modes. In 2002/2003, Paepegem [18, 127] presented an extension of the Tsai-Wu failure criterion for progressive failure analysis. Instead of one failure index k (section 5.3.2), a set of directional failure indices $\sum_{ij}$ were defined with the respective stress component σ_{ij}. In this two-dimensional formulation, the general Tsai-Wu quadratic criterion in stress space can be written for each separate stress component σ_{ij} as [18, 127]:

$$F_1 \frac{\sigma_1}{\sum_{11}} + F_2\sigma_2 + F_{11}\left(\frac{\sigma_1}{\sum_{11}}\right)^2 + F_{22}\sigma_2^2 + F_{66}\tau_{12}^2 = 1$$

5.70

$$F_1\sigma_1 + F_2 \frac{\sigma_2}{\sum_{22}} + F_{11}\sigma_1^2 + F_{22}\left(\frac{\sigma_2}{\sum_{22}}\right)^2 + F_{66}\tau_{12}^2 = 1$$

5.71

$$F_1\sigma_1 + F_2\sigma_2 + F_{11}\sigma_1^2 + F_{22}\sigma_2^2 + F_{66}\left(\frac{\tau_{12}}{\sum_{12}}\right)^2 = 1$$

5.72

where $\sum_{11}$, $\sum_{22}$ and $\sum_{12}$ are the corresponding failure indices for the stress components σ_{11}, σ_{22} and τ_{12}, respectively. For the assessment of the relative importance of the separate stress components σ_{ij} at failure, $\sum_{ij}$ were calculated as [18, 127]:

$$\sum_{11} = \frac{\sum_{11}^{2D}}{1 + (\sum_{11}^{2D} - \sum_{11}^{1D})}$$

5.73

$$\Sigma_{22} = \frac{\Sigma_{22}^{2D}}{1 + (\Sigma_{22}^{2D} - \Sigma_{22}^{1D})}$$

5.74

$$\Sigma_{12} = \frac{\Sigma_{12}^{2D}}{1 + (\Sigma_{12}^{2D} - \Sigma_{12}^{1D})}$$

5.75

The failure indices $\sum_{ij}^{2D}$ can be calculated from the respective equations 5.70 to 5.72. The one-dimensional failure indices $\sum_{ij}^{1D}$ are defined as the ratio of the stress σ_{ij} to the respective 1D static strength. It should be noted that, according to [18, 127] indices $\sum_{ij}$ are defined as damage dependent failure indices, which is not within the scope of this study. However, using this modified definition of the failure indices, it is possible to predict which stress component is mainly responsible for failure. The results of different failure modes of the investigated WHIPOX™ are presented in section 7.2.2.

5.4 Inelastic deformation factor *Δ*

As mentioned in section 5.3.2, in the case of non-linear elastic behavior up to failure, stress and strain cannot be directly tied to the initial material stiffness matrix Q_{ij}. The Classic Laminate Theory and the Tsai-Wu failure criterion are restricted to linear elastic behavior of the composite. This does not allow for the calculation of failure strain in non-linear elastic behaviors of laminates. In this section, an empirical modeling approach is presented to introduce the calculation of failure strain of the laminate with non-linear elastic behavior.

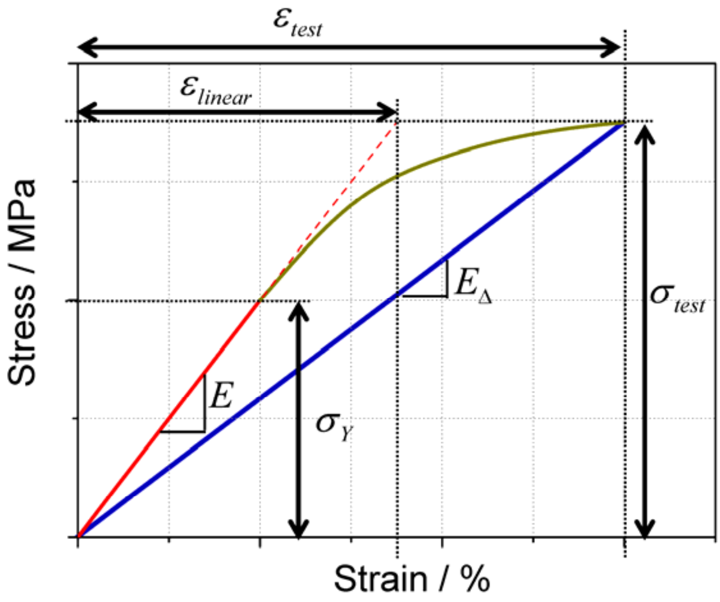

Figure 5.5: Tensile stress-strain behavior of a typical WHIPOX™ laminate with non-linear elastic behavior.

The aim of this modeling approach is to predict failure strain under varying orientations for investigated WHIPOX™ material. In order to explain the approach, tensile stress-strain behavior of a typical WHIPOX™ laminate with non-linear elastic behavior is shown in Figure 5.5. Since the failure strength σ_{test} can be calculated through Tsai-Wu failure criterion in stress space, the strain value ε_{linear} calculated through the initial material stiffness E is underestimated when compared to the failure strain ε_{test}. This difference is observed in the behavior of the investigated material WHIPOX™ with different fiber orientations and a trend is noticed. An inelastic deformation factor $\mathit{\Delta}$ is supposed to consider the relationship between the two different strain values ε_{linear} and ε_{test}. This inelastic deformation factor can be illustrated through the equation:

$$\mathit{\Delta} = \frac{\varepsilon_{linear}}{\varepsilon_{test}}$$

5.76

Obviously, there is linear elastic behavior up to failure if $\mathit{\Delta} = 1$. According to the test results in the following section 6.1, the value of factor $\mathit{\Delta}$ is strongly dependent on the microstructure of WHIPOX™ matrix (with or without shrinkage cracks) and the fiber orientation θ. On the other hand, since WHIPOX™ material does not show a distinctive yield point in any direction, the virtual yield stress σ_Y in Figure 5.5 was defined as the function of factor $\mathit{\Delta}$ and failure strength σ_{test}:

$$\sigma_Y = \sigma_{test}\mathit{\Delta}$$

5.77

The factor $\mathit{\Delta}$ is considered to be a property of each layer in a particular laminate. It is reasonable to use $\mathit{\Delta}$ when the layer properties are assembled by individual sub-matrices: strain stiffness $[S_{ij}]$, coupling stiffness $[C_{ij}]$ and bending stiffness $[B_{ij}]$. The equations 5.23 to 5.25 from section 5.1 are rewritten as:

$$\left(S_{ij}\right)_{\Delta} = \sum_{k=1}^{N} (\bar{Q}_{ij})_k t_k \mathit{\Delta}$$

5.78

$$\left(C_{ij}\right)_{\Delta} = \sum_{k=1}^{N} (\bar{Q}_{ij})_k t_k \mathit{\Delta} \bar{Z}_k$$

5.79

$$\left(B_{ij}\right)_{\Delta} = \sum_{k=1}^{N} (\bar{Q}_{ij})_k (t_k \mathit{\Delta} \bar{Z}_k{}^2 + (t_k \mathit{\Delta})^3/12)$$

5.80

Engineering constants are then calculated from these new stiffness matrices, such as the effective stiffness E_{Δ} in Figure 5.5. This will lead to a possibility of calculation of failure strain ε_{test}. Since a point-by-point modeling of non-linear elastic behavior up to failure is not the aim of this study, a bilinear model was used to describe behavior beyond the virtual yield stress σ_Y in Figure 5.6. The inelastic deformation factor Δ is one of the particular features of the investigated material WHIPOX™. The relationship between Δ, the microstructure of WHIPOX™ matrix and the value of Δ for different fiber orientations is presented in section 7.3.

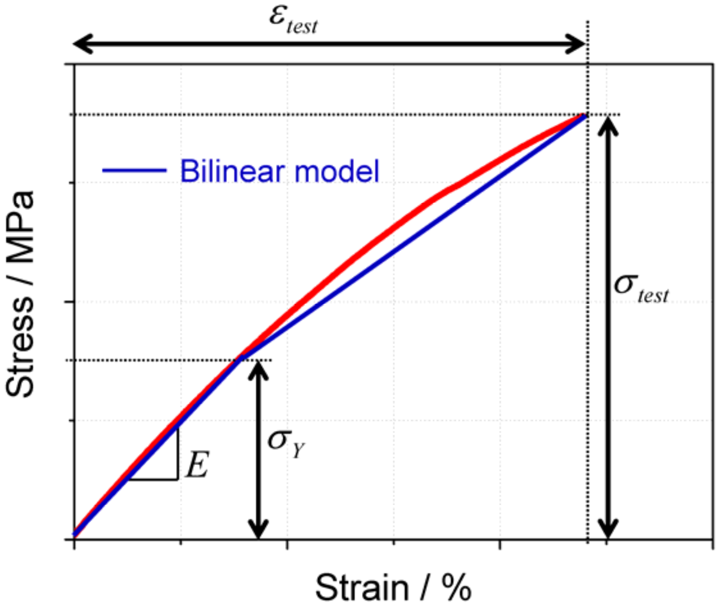

Figure 5.6: Bilinear model for tensile stress-strain behavior of a typical WHIPOX™ laminate with non-linear elastic behavior.

5.5 Manufacturing factor Ω

Due to the variations in the manufacturing process of CMCs, the previously presented modeling approaches based on CLT, the Inverse approach of CLT (ILT), the modified Tsai-Wu criterion and inelastic deformation are upgraded by introducing a manufacturing factor Ω_k, which is one of the particular features of the investigated WHIPOX™. The factor Ω_k takes into account FVC, porosity (e') and the angle between fiber orientation and occurring stress. The manufacturing process of the material results in variations in the FVC and e' of the composite, which are decisive for the mechanical properties of the component. With the assumption that each UD-layer has identical fiber volume content and homogeneous porosity on a macroscopic scale, a linear mixing rule for the compound property can be modified to determine the manufacturing factor Ω_k of each equivalent UD-layer k. Using the normal linear model the compound property with the influence of property A and property B can be defined as:

$$The\ compound\ property\ =\ Property\ A\ *\ Proportion\ of\ A\ +\ Property\ B\ *\ Proportion\ of\ B$$

The manufacturing factor Ω_k of WHIPOX™, is defined by the combination of the influence of FVC, e' and angle of fiber orientation between the average values of the laminate and the actual values of layer k. $Property\ A$ is the ratio of the actual FVC_k of the layer to the average $\overline{FVC}$ of the laminate. $Property\ B$ takes into consideration the ratio of the average $\overline{e'}$ to e'_k. The $Proportion\ of\ A$, defined as the angle between the fiber orientation of the layer k and the occurring stress, is related to the FVC dominated direction. On the other hand, $Proportion\ of\ B$ includes the angle between the fiber orientation of the layer k to the perpendicular direction of occurring stress and is considered to be the e' dominated direction. The value "$\theta_k/90$" serves as the proportion of the ratio of the porosity. As $Property\ A$ and B together form a complete compound property with individual contributions, the sum of $Proportion\ of\ A$ and $Proportion\ of\ B$ is 100 %. Therefore, the value "$1-(\theta_k/90)$" is assigned to the $Proportion\ of\ A$. With this information, the manufacturing factor Ω_k can be determined with the following equation:

$$\Omega_k = \left(\frac{FVC_k}{\overline{FVC}}\right)\left(1-\frac{\theta_k}{90}\right)+\left(\frac{\overline{e'}}{e'_k}\right)\left(\frac{\theta_k}{90}\right)$$

5.81

The manufacturing factor Ω_k is defined as a property of a layer in a particular laminate because it is calculated for individual layers factoring in the angle between the fiber orientation of the layer k and the occurring stress. With this definition, it is reasonable to use Ω_k when layer properties are assembled into the individual sub-matrices: strain stiffness $[S_{ij}]$, coupling stiffness $[C_{ij}]$ and bending stiffness $[B_{ij}]$. Therefore, the equations 5.78 to 5.80 from section 5.4 are rewritten as the equations 5.82 to 5.84. The Ω_k value is coupled with the individual ply thickness t_k, which leads to a more precise prediction of the material properties of the layer k. Engineering constants are then calculated from these new matrices:

$$\left(S_{ij}\right)_{\Delta,\Omega_k} = \sum_{k=1}^{N} \left(\bar{Q}_{ij}\right)_k t_k \Delta\Omega_k$$

5.82

$$\left(C_{ij}\right)_{\Delta,\Omega_k} = \sum_{k=1}^{N} \left(\bar{Q}_{ij}\right)_k t_k \Delta\Omega_k \bar{Z}_k$$

5.83

$$\left(B_{ij}\right)_{\Delta,\Omega_k} = \sum_{k=1}^{N} \left(\bar{Q}_{ij}\right)_k \left(t_k \Delta\Omega_k \bar{Z}_k^{\,2} + \left(t_k \Delta\Omega_k\right)^3/12\right)$$

5.84

One more observation concerning Ω_k is the calculation of the shear module G_{xy} and Poisson's ratio ν_{xy}. Both describe the material behavior between the parallel and perpendicular direction x and y for the layer k. Considering the definitions of the $Proportion\ of\ A$ and B in equation 5.81, both shear modulus G_{xy} and

Poisson's ratio ν_{xy} will be calculated to be dependent on $(\Omega_k)(\Omega_k)^{-1}$. As a result the impact of Ω_k on G_{xy} and ν_{xy} is negligible.

It should be noted that the manufacturing factor Ω is not a characteristic value of the UD-layer but only quantifies the uncertainties in the laminate for different batches. This means that for analytical modeling the calculated properties of the equivalent UD-layer are independent of different batches.

5.6 Chain from testing to modeling

The advanced modeling approach presented in this work is summarized in a flow diagram (Figure 5.7). This modeling chain is created with consideration of particular features of WHIPOX™ material.

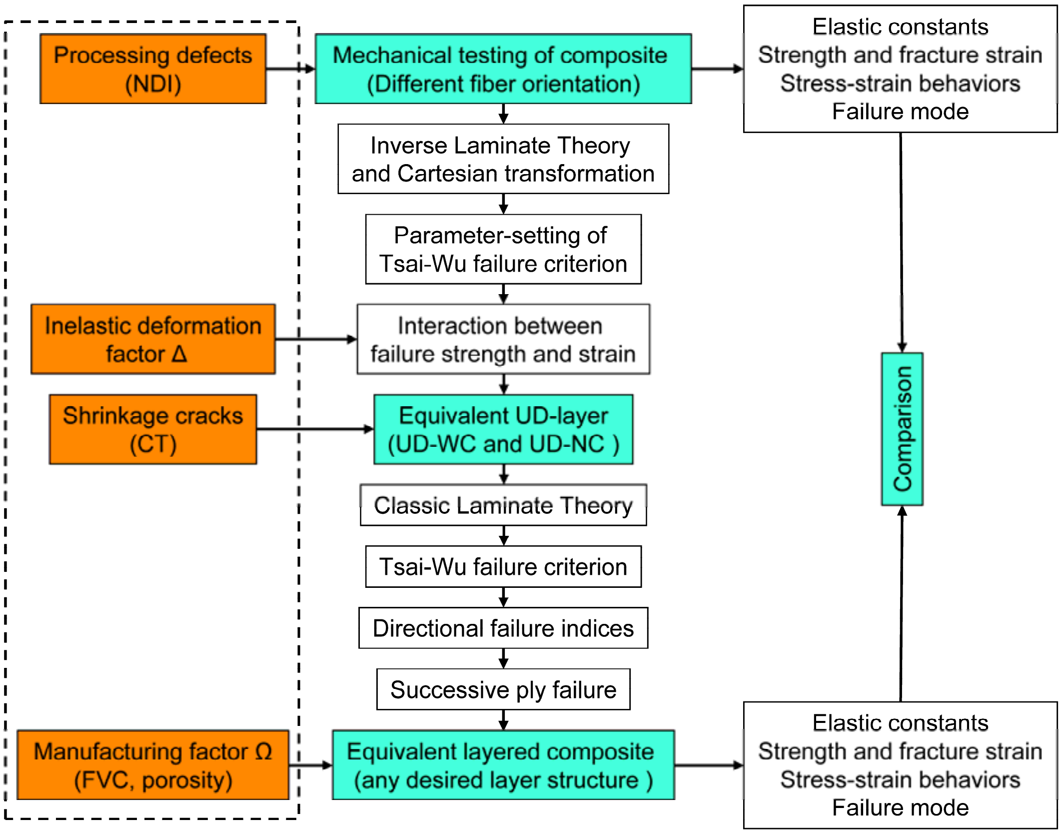

Figure 5.7: Chain from testing to modeling with consideration of material particular features.

At first, the mechanical properties of the investigated wound oxide ceramic composite WHIPOX™ with different winding angles is characterized through in-plane mechanical testing: tensile, compression and Iosipescu-shear test (see section 6.1). In order to prevent any faulty parts from compromising the results, the processing defects (inhomogeneity) of the investigated WHIPOX™ plates, as one of the material particular features, was evaluated through NDI testing before mechanical testing was conducted (see section 6.2).

Then, a virtual equivalent UD-layer was implemented in the proposed approach. The elastic properties of the equivalent UD-layer are calculated using an inverse operation of classic laminate theory and Cartesian transformation. The parameters of Tsai-Wu failure criterion are fitted with the values of maximum stress and strain through different test results. The interaction between failure strength and strain is evaluated using another material particular feature “inelastic deformation factor Δ”. Based on the above, the complete material properties of the equivalent UD-layer including elastic properties, strength, failure strain and inelastic deformation were calculated and evaluated.

After that, based on the microstructure analysis of shrinkage cracks in matrix through CT technology (one of the particular features of the investigated WHIPOX™), the modeling of the properties of WHIPOX™ was divided into two classes: WHIPOX™ with matrix cracks and WHIPOX™ without matrix cracks (see section 4.2).

Furthermore, through the stacking of these equivalent UD-layers with any desired layer structure (fiber orientation, thickness and number of layers), an equivalent layered composite is created. Its in-plane material behavior can be predicted and described with the help of modified CLT and modified Tsai-Wu failure criteria. By using the modified definition of the directional failure indices it is possible to predict which stress component is mainly responsible for failure. Based on the analysis of different microstructures (see section 4.2), two models were used to describe composite behavior and to predict failure strength and strain. Firstly, the linear model was used for the group with linear elastic behavior up to its failure. Secondly, the bilinear/multi model was used for the group with non-linear behavior beyond the virtual yield stress, as well as for the situation with successive ply failures of laminate after the failure of first layer group.

Finally, the analytical model for different batches with inhomogeneities created due to the manufacturing process is updated with consideration given to different fiber volume contents, porosities and the angles between fiber orientation and occurring stress. A manufacturing factor Ω for different batches was evaluated through a modified mixing rule. The results of modeling, including elastic constants, strength, fracture strain, stress-strain behaviors and failure mode, are compared to the test results.

Detailed description of the modeling results and of the comparison are introduced in the following sections.

6 Characterization of the material properties

6.1 Results from experimental testing

Figure 6.1 shows typical tensile, shear and compression stress-strain curves of the investigated configurations. The longitudinal and transverse strains are presented. The indications +22.5°/-22.5° (+67.5°/-67.5°) and +30°/-30° (+60°/-60°) denote the angles between fiber and loading directions for tensile and compression testing (see Table 3.1 for the tensile and compression tests). For the Iosipescu-shear tests, the fiber orientation was defined with regards to the load direction of the test samples (see Table 3.1 for Iosipescu-shear test).

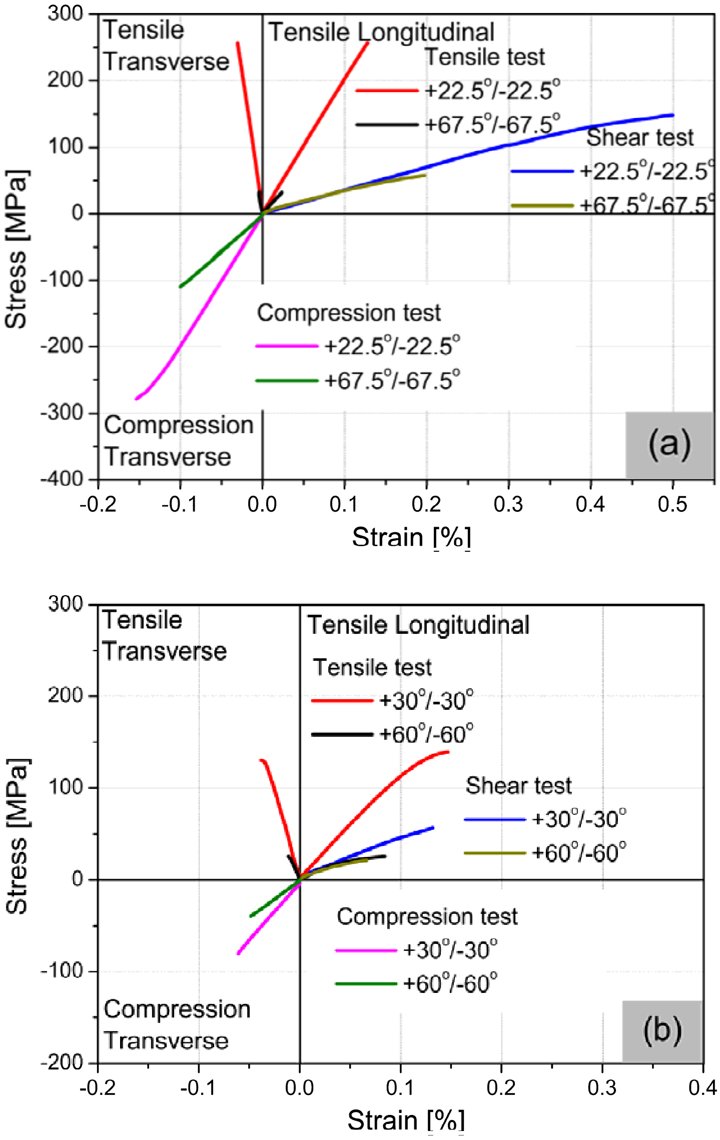

Figure 6.1: Typical tensile, compression and Iosipescu-shear stress-strain curves from strain gauge measurements for WHIPOX™ with a) fiber orientations ±22.5° (±67.5°) and b) fiber orientations ±30° (±60°).

The stress-strain response of WHIPOX™ strongly depends on the loading direction. With a ±22.5° orientation and under tensile loading, the composites show an almost linear behavior with higher stiffness and strength as seen in Figure 6.1a. Since the fibers are oriented close to the loading direction, the matrix is able to transfer the applied load to the fibers. In contrast, under a ±67.5° tensile loading the composite shows an almost linear behavior as well but stiffness and the strength values are considerably lower. This is mainly due to the dominating weak matrix in this loading direction. Furthermore, WHIPOX™ with matrix cracks (see section 4.2) under ±30° and ±60° tensile loading shows non-linear behavior (Figure 6.1b). Thess indicates that the damage to the matrix and the effects of the energy dissipation of matrix cracks lead to a significant degradation of the composite's properties in this loading direction (see section 5.4).

Figure 6.2: Fracture path of WHIPOX™ tensile sample with a fiber orientation of ±22.5°.

The fracture mechanism of the investigated material under tensile loading strongly depends on fiber orientation and loading direction. For example, for the fiber orientation of ±22.5°, a Zig-Zag shaped fracture path is observed with some fiber bundles bridging the crack (Figure 6.2). By using the modified Tsai-Wu failure criterion, more detailed analysis for the relationship between the tensile fracture mechanism, fiber orientation and loading direction is discussed in section 7.2.

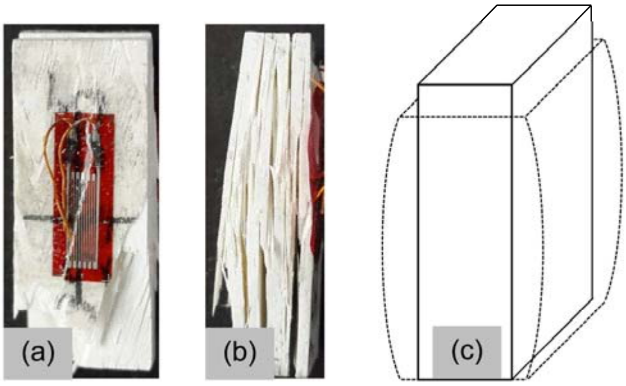

Figure 6.3: Fracture path in a WHIPOX™ compression sample with a fiber orientation of ±22.5° with two different fracture mechanisms: a) macroscopic in-plane shear failure and b) interlaminar shear failure. c) Graphic representation of the buckling of the sample during the compression test. The dash line represents the profile after test.

Under compression loading, the Young' modulus and the strength of the weak fiber orientation (±67.5° in Figure 6.1a and ±60° in Figure 6.1b) are almost twice as low as in the perpendicular loading direction (±22.5° and ±30°). In contrast to the tensile test, the compression stress-strain curves displayed in Figure 6.1 are linear for different fiber orientations. Principally, two different failure mechanisms combine for the WHIPOX™ compression sample: (1) macroscopic in-plane shear failure (Figure 6.3a) and (2) interlaminar shear failure (Figure 6.3b). With the first macroscopic in-plane shear failure mechanisms, the existing and emerging cracks under compression load spread mainly along the fiber orientation. This causes a macroscopic in-plane cracking through the strain gauges, which have been seen to break easily before the failure of the samples. In comparison with the second failure mechanism, because of the relatively low interlaminar shear strength (approx. 15 MPa in [3]), the samples buckle strongly (sample in Figure 6.3b and dash line in Figure 6.3c). This results in an interlaminar failure and a difficult interpretation of strain gauge signal. This phenomenon can be observed in almost all pressure tests. Due to these difficulties in determining the reliable stress-strain behavior during the compression test, the fracture strain was not recorded in this work.

Figure 6.4: Fracture path of WHIPOX™ Iosipescu-shear sample with a fiber orientation of ±22.5°.

The in-plane shear behavior determined through the Iosipescu-method is also shown in Figure 6.1. The fiber orientations of the shear sample were in the directions ±22.5° and ±67.5° in Figure 6.1a and ±30° and ±60° in Figure 6.1b relative to the longitudinal axis of specimen (see Table 3.1 for Iosipescu-shear test). As expected from CLT the shear modulus under ±22.5° and ±67.5° (Figure 6.1a) loading are identical but the potential shear strength of ±22.5° is much higher. Similarly, identical shear modulus with ±30° and ±60° but a higher potential strength for ±30° can be observed in Figure 6.1b. It should be pointed out that the shear stress-strain curves displayed in Figure 6.1 are not extended up to failure because the Iosipescu-shear specimens did not fracture in the shear area (Figure 6.4). The shear strength could not be reached in this experiment, because of the relatively low compressive strength. The specimens fail locally in the testing rig where high compressive stresses prevail. The necessary stress-strain curve for the determination of the shear modulus only relates to the initial linear region. Therefore, the determined shear modulus could surely be documented as characteristic values of the investigated composite material but specimen failure, shear fracture strength and ultimate strain are not discussed in this work.

The determination of the elastic constants was conducted using a linear fit of the initial linear region of the stress-strain curves. The measured elastic constants under tensile, compressive and shear load for WHIPOX™ with non-orthogonal and orthogonal and asymmetrical (off-axis 0°/60°) winding angles are summarized in Table 6.1. E_x and E_y are the Young's modulus, ν_{xy} is the Poisson's ratio and G_{xy} is the shear modulus. The indices x and y correspond to the indications from Figure 4.1b. The index T denotes the tensile test and C the compression test. For orthogonally wound WHIPOX™ the Young's modulus E_x is equal to E_y. The FVC and open porosity e' scatter in a wide range and the individual value of different batches are shown in Table 6.1. The description of the measuring methods can be found in section 3.2. Batch BT45 and BT090 were tested in different directions but prepared from the same plate, therefore, identical FVC and porosity e' have been listed in Table 6.1. Specimens from batch BT060 for off-axis tensile testing were prepared from the plate BT30, therefore, the FVC and e' for both batches are same. The experimental tests for the batch WF3 with orientations ±3°/±87° were conducted in Institute of Materials Research, German Aerospace Center Cologne.

Table 6.1: Elastic constants in directions x and y obtained from tensile, Iosipescu-shear and compression tests for WHIPOX™ with different winding angles.

	Batch	Test direction	FVC [%]	e' [%]	E_x^T [GPa]	E_y^T [GPa]	ν_{xy} [-]	G_{xy} [GPa]	E_x^C [GPa]	E_Y^C [GPa]
Non-Orthogonal	WF3	±3° (±87°)	42,7	22,0	214.0 ± 10.0	117.0 ± 7.0	0.19 ± 0.01	41.9 ± 0.9	-	-
	BT15	±15° (±75°)	41,2	27,9	202.0 ± 7.3	114.2 ± 3.3	0.25 ± 0.03	51.4 ± 6.9	202.3 ± 3.8	126.5 ± 14.9
	BT225	±22.5° (±67.5°)	39.1	18.5	198.4 ± 15.2	141.7 ± 13.7	0.30 ± 0.05	55.2 ± 11.9	203.5 ± 22.3	143.8 ± 19.3
	BT30	±30° (±60°)	34,0	31,4	131.5 ± 9.1	68.9 ± 8.3	0.37 ± 0.04	50.7 ± 11.4	127.3 ± 29.7	82.7 ± 9.6
Orthogonal	BT45	±45°	40.5	29.1	99.6 ± 2.0	99.6 ± 2.0	0.37 ± 0.08	59.2 ± 2.1	101.6 ± 2.3	101.6 ± 2.3
	BT090	0°/90°			122.8 ± 6.1	122.8 ± 6.1	0.12 ± 0.01	43.6 ± 8.0	152.5 ± 51.7	152.5 ± 51.7
Off-axis	BT060	0°/60°	34.0	31.4	121.0 ± 16.0	-	-	-	-	-

The tensile and compression strength values of different winding angles were calculated from the maximum force using the formulas for tensile and compression tests, respectively. The determined strengths σ are listed in Table 6.2. For orientation ±45° and 0°/90° the strength values σ_x and σ_y are same.

Table 6.2: Strength values in directions x and y obtained from tensile and compression tests for WHIPOX™ with different winding angles.

	Batch	Test direction	σ_x^T [MPa]	σ_y^T [MPa]	σ_x^C [MPa]	σ_y^C [MPa]
Non-Ortho-gonal	WF3	±3° (±87°)	289.0 ± 14.7	21.0 ± 0.0	-	-
	BT15	±15° (±75°)	276.8 ± 4.9	22.1 ± 3.8	-244.1 ± 20.6	-128.0 ± 13.7
	BT225	±22.5° (±67.5°)	233.4 ± 35.7	37.0 ± 3.6	-291.6 ± 37.6	-125.1 ± 23.7
	BT30	±30° (±60°)	133.5 ± 18.5	27.7 ± 2.8	-124.7 ± 27.7	-75.6 ± 21.3
Ortho-gonal	BT45	±45°	96.4 ± 8.5	96.4 ± 8.5	-104.2 ± 0.2	-104.2 ± 0.2
	BT090	0°/90°	134.3 ± 17.3	134.3 ± 17.3	-193.6 ± 32.1	-193.6 ± 32.1
Off-axis	BT060	0°/60°	137.5 ± 9.2	-	-	-

The fracture strain ε of the tensile test was defined as the strain value at maximum tensile strength, which is listed in Table 6.3. For orthogonal orientations of ±45° and 0°/90° the ultimate strain ε_x is equal to ε_y.

Table 6.3: Tensile fracture strain values in directions x and y for WHIPOX™ with different winding angles.

	Batch	Test direction	ε_x [%]	ε_y [%]
Non-Ortho-gonal	WF3	±3° (±87°)	0.135 ± 0.006	0.019
	BT15	±15° (±75°)	0.138 ± 0.003	0.020 ± 0.004
	BT225	±22.5° (±67.5°)	0.118 ± 0.014	0.026 ±0.002
	BT30	±30° (±60°)	0.122 ± 0.029	0.067 ± 0.012
Ortho-gonal	BT45	±45°	0.134 ± 0.024	0.134 ± 0.024
	BT090	0°/90°	0.123 ± 0.025	0.123 ± 0.025
Off-axis	BT060	0°/60°	0.146 ± 0.003	-

The typically tensile stress-strain behaviors of WHIPOX™-NC and -WC with different fiber orientations are summarized in Figure 6.5. The behavior of fiber orientations ±3° and ±15° (in Figure 6.5a) and ±67.5° and ±75° (in Figure 6.5b) are linear in the laminate of WHIPOX™-NC. The non-linear behavior up to failure of the laminate of WHIPOX™-WC with the fiber orientations ±30°, ±45° and ±60° are shown in Figure 6.5a. The comparison of test and modeling results are shown and discussed in section 7.3.1.

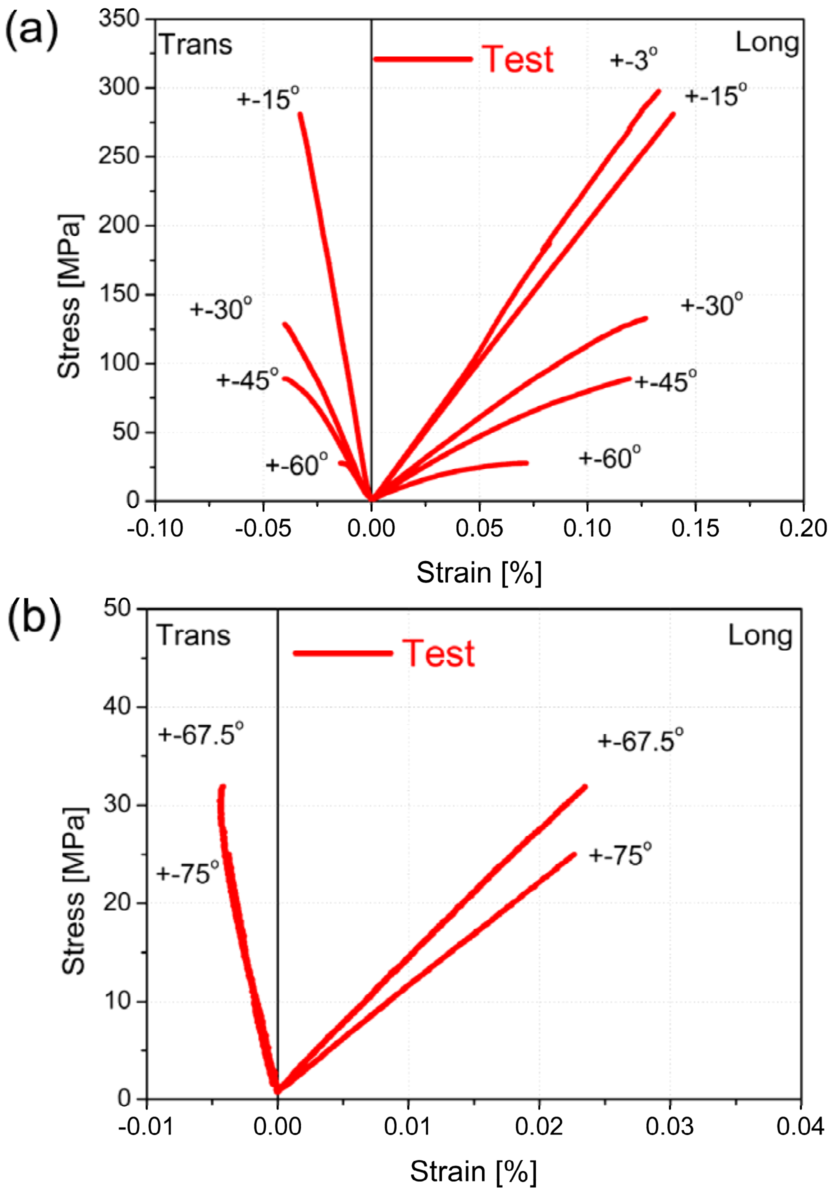

Figure 6.5: Stress-strain behaviors of WHIPOX™-NC and –WC with different fiber orientations under tensile load.

6.2 Effects of processing defects

As one of the distinct properties, the inhomogeneity of the investigated WHIPOX™ plates was evaluated through air-coupled ultrasonic testing, lock-in thermography testing and CT testing (experimental set-up for non destructive inspection (NDI) has been described in section 3.1) before mechanical testing was conducted. This was done to prevent any faulty parts from compromising the results.

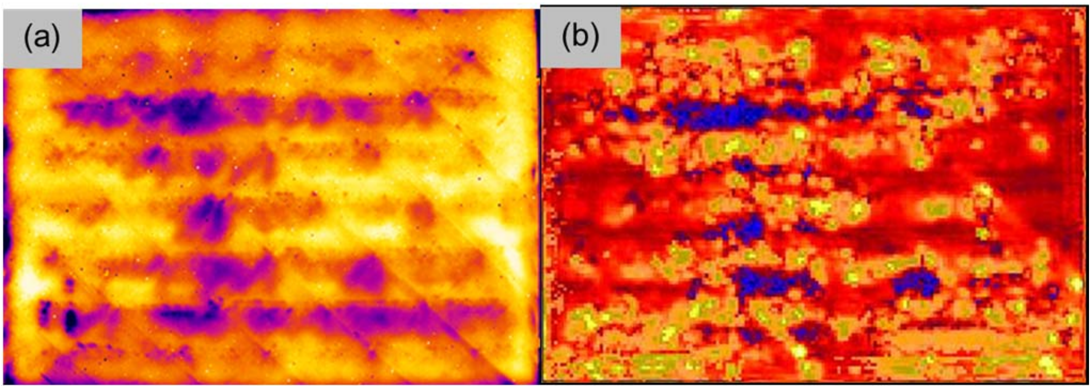

Figure 6.6 Results of the Non Destructive Inspection of batch BT45 through a) lock-in thermography testing and b) air-coupled ultrasonic testing.

Figure 6.6a shows the phase image of lock-in thermography testing for batch BT45. The plate shown here has dimensions of approx. 360*250*5 mm^3 (length/width/thickness) and a fiber orientation of ±45°. The rhombic fiber filament structure is clearly identified. The results obtained by lock-in thermography inspection reveals some areas of defects which are indicated by the dark blue and purple colours. The corresponding air-coupled ultrasonic scan for the same plate BT45 is shown in Figure 6.6b. The location of material defects seen in both forms of testing in Figure 6.6a and b are comparable and aligned in a horizontal and vertical orientation which is certainly connected with the rhombic fiber filament structure and the resulting cross-over points. It is the most likely interpretation that the material contains local areas of delaminated material or aggregations of porosity.

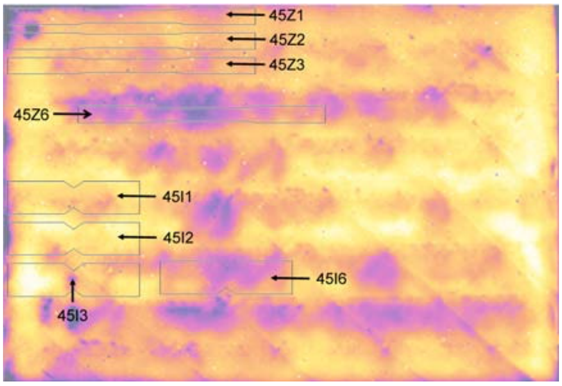

Figure 6.7: Lock-in thermography image information and test specimen selection for tensile and Iosipescu-shear testing. Specimens 45Z6 and 45I6 were prepared from areas of increased porosity (outlined by dark purple color).

In order to examine the different mechanical properties of one single WHIPOX^{TM} plate, the lock-in thermography phase image of batch45 was used as a reference for defect distribution. Figure 6.7 showed several regions of different porosity that were clearly identified within the plate. The mechanical behavior of these regions was evaluated using tensile and shear tests. The fiber orientation was ±45° with regards to the load direction of the test samples. The specimen geometry and dimensions are shown in Table 3.1. The main objective here is the verification of a correlation between the material's local porosity and its mechanical properties. Table 6.4 summarises the investigated samples.

Thus, the microstructure of two tensile specimens processing from different areas according to the Figure 6.7, 45Z2 from a "normal area" and 45Z6 from a "defect area", were extracted and analyzed with high resolution CT inspection. Two different Iosipescu-shear specimens, 45I2 from a "normal area" and 45I6 from a "defect area" were examined in same way. It should be noted that tensile specimens, including 45Z2, and Iosipescu-shear specimens, including 45I2 from batch BT45, were all prepared from "normal areas". The average values of the mechanical properties of BT45 have been listed in Table 6.1 to Table 6.3 in section 6.1. Two more tensile specimens from batch BT15 with a load direction of ±75°, 75Z5 from a "normal area" and 75Z6 from a "defect area", have been treated in same way.

A small cube with an edge size of a=3.6 mm from the specimen's estimated failure zone was analyzed with CT. The minimum voxel size of these CT-scans was 4.5 µm. Hence, structural details of >10 µm were principally detectable under these conditions. Figure 6.8 shows the reconstructed 3-dimensional volumes of specimens 45Z6 and 45I6 which were both cut from areas with increased porosity (i.e. "defect area"), according to the lock-in thermography image in Figure 6.7. While the brown phase of these images depicts the 3-dimensional distribution of fibers within the surrounding matrix, the pores and interlaminar gaps between the fiber bundles are visible as elongated and tubular-like cavities throughout the laminate microstructure. As the two 3-dimensional CT images indicate for both samples that there is an accumulation of larger pores in some layers of the CMC's laminate. These are the defects which were detected with lock-in thermography and air-coupled ultrasonic testing inspection in Figure 6.6a and b.

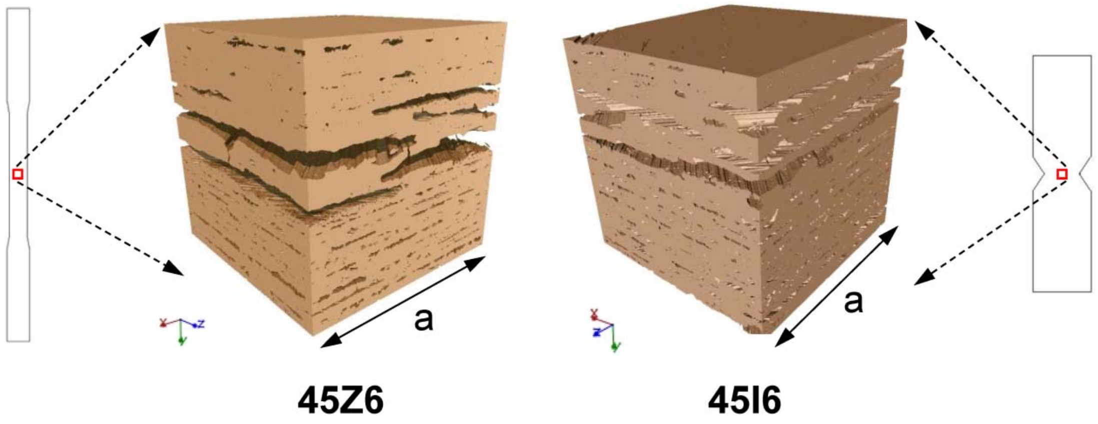

Figure 6.8: Analysis of local porosity distribution in the center area of tensile specimen 45Z6 and Iosipescu-shear specimen 45I6 through high resolution CT testing. The edge size is a=3.6 mm.

The results are summarized in Table 6.4. The porosity e'_{CT} is local porosity evaluated through CT investigation and e' is the porosity of a related batch, which was measured using Archimedes method. Because of the limitation of the minimum voxel size of these CT-scans, the local porosity e'_{CT} is lower than the porosity of the related batch. The determined mechanical properties, Young's modulus E, shear modulus G and strength σ of each specimen and the average values of the related batch are also shown in Table 6.4. According to the results shown in Table 6.4, there is a considerable difference found in the mechanical properties of specimens taken from porous locations (45Z6, 75Z6 and 45I6) and those from other locations with denser material (BT45 including 45Z2/45I2 and BT15 including 75Z5). In the case of sample 45Z6, the material fails at a relatively low stress level of 71.3 MPa. This is approx. only 74 % compared to the load levels of the other samples: the average tensile strength value of batch BT45 is 96.4 MPa. In the direction of ±75°, the local porosity of sample 75Z6 is almost twice as much as the 75Z5 and the E-modulus and tensile strength is considerably lower than the other samples of batch BT15. Regarding the shear test samples, the porous material (45I6) with a relatively high local porosity e'_{CT} also shows a relatively low shear modulus compared to the other samples of batch BT45.

Table 6.4: Specimen overview and the mechanical characteristic values and porosity of tensile and Iosipescu-shear specimen processing from different areas according to NDI testing.

		e'_{CT} [%]	e' [%]	E- and G-modulus [GPa]	σ [MPa]
Tensile test	45Z2	17.0	-	100.4	95.7
	45Z6	20.5	-	93.1	71.3
	BT45	-	29.1	99.6 ± 2.0	96.4 ± 8.5
	75Z5	10.4	-	111.5	25.6
	75Z6	20.5	-	33.8	12.2
	BT15	-	27,9	114.2 ± 3.3	22.1 ± 3.8
Iosipescu-shear test	45I2	9.4	-	60.0	-
	45I6	19.7	-	49.6	-
	BT45	-	29.1	59.2 ± 2.1	-

It is obvious that there is a correlation between the detected defects with high local porosity and the mechanical properties of the test specimens. This inhomogeneity of the investigated plates has been taken into consideration as one of the distinctive features of WHIPOX™ (section 2.4). The modeling approaches for computation of the mechanical behavior described in section 5 were based on the experimental results from "normal areas", which have been summarized in Table 6.1 to Table 6.3.

7 Modeling of mechanical properties

As discussed in the previous sectios, characterization of the material properties is the prerequisite for the implementation of the modeling approaches (see modeling chain in Figure 5.7). Therefore, the mechanical properties of the investigated material WHIPOX™ with different winding angles are determined through in-plane mechanical testing and the results were summarized in section 6.1. Furthermore, particular features of investigated material have to be taken into consideration in order to predict mechanical properties with more accuracy: the processing defects (inhomogeneity) of the investigated WHIPOX™ plates were evaluated through NDI testing before mechanical testing was conducted (see section 6.2); an inelastic deformation factor Δ was defined as a relationship between failure strength and failure strain, and used to describe the inelastic behavior of the investigated material WHIPOX™ (see section 5.4); based on the microstructure analysis of shrinkage cracks in matrix through CT technology, the modeling of the properties of WHIPOX™ has to be divided into two classes: WHIPOX™ with matrix cracks and WHIPOX™ without matrix cracks (see section 4.2); in order to qualify uncertainties in the laminate during the manufacturing process, a manufacturing factor Ω for different batches needs to be evaluated, which takes into account FVC, porosity (e') and the angle between fiber orientation and occurring stress (see section 5.5).

In this section, according to the modeling chain in section 5.6 advanced modeling approaches for the prediction of the material properties of wound ceramic composites are presented. As the core component of the modeling chain, a virtual equivalent UD-layer is implemented in the proposed approach. At first, the complete material properties of the equivalent UD-layer were calculated and evaluated in the following sections. The elastic properties of the equivalent UD-layer are calculated using an inverse operation of classic laminate theory and Cartesian transformation. The parameters of Tsai-Wu failure criterion are fitted with the values of maximum stress and strain through different test results. The interaction between failure strength and strain is evaluated using inelastic deformation factor Δ. Then, through the stacking of these equivalent UD-layers with any desired layer structure (fiber orientation, thickness and number of layers), an equivalent layered composite is created. Its in-plane material behavior is predicted and described with the help of modified CLT and modified Tsai-Wu failure criteria. After that, by using the modified definition of the directional failure indices it is possible to predict which stress component is mainly responsible for failure. Based on the analysis of different microstructures (see section 4.2), two models were used to describe composite behavior and to predict failure strength and strain. Firstly, the linear model was used for the group with linear elastic behavior up to its failure. Secondly, the bilinear/multi model was used for the group with non-linear behavior beyond the virtual yield stress, as well as for the situation with successive ply failures of laminate after the failure of first layer group. Furthermore, the analytical model for different batches with inhomogeneities created due to the manufacturing process is updated with the manufacturing factor Ω. Finally, the results of modeling, including elastic constants, strength, fracture strain, stress-strain behaviors and failure mode, are compared to the test results in each following sections.

7.1 Modeling of elastic properties

In this section, the Classical Laminate Theory and the Inverse Classic Laminate Theory are used to calculate the elastic properties of WHIPOX™ with different microstructures. The evaluation of manufacturing factor Ω_k using FVC, porosity e' and angle between fiber orientation and occurring stress for the batches are explained. The effect of this factor over the prediction of material properties is discussed and compared with the original experiment results. The following results of this section have been published in [88].

7.1.1 Computing the elastic properties of the equivalent UD-layer

The modeling approach for the computation of the equivalent UD-layer described in section 5.2 "Inverse approach of Classic Laminate Theory" will be applied first. The elastic parameters of an equivalent UD-layer $(E_1^T, E_2^T, \nu_{12}, G_{12}, E_1^C, E_2^C)$ were calculated based on the experimental data from three typical tested WHIPOX™ composites with non-orthogonal fiber orientations ±3°/±87° (WF3), ±15°/±75° (BT15) and ±30°/±60° (BT30) under tensile, shear and compression load. The winding angle of these three batches is spread from a loading almost in fiber direction (±3°) to a loading almost in transverse to fiber direction (±87°), which is the main reason for choosing them for the calculation of equivalent UD-layer properties. The evaluated elastic properties of these three batches, their individual FVC and open porosity e' have been taken from Table 6.1 and listed in Table 7.1.

Table 7.1: Elastic constants, individual FVC and open porosity e' with non-orthogonal fiber orientations ±3°/±87° (WF3), ±15°/±75° (BT15) and ±30°/±60° (BT30).

Batch	Test direction	FVC [%]	e' [%]	E_x^T [GPa]	E_y^T [GPa]	ν_{xy} [-]	G_{xy} [GPa]	E_x^C [GPa]	E_y^C [GPa]
WF3	±3° (±87°)	42.7	22.0	214.0 ± 10.0	117.0 ± 7.0	0.19 ± 0.01	41.9 ± 0.9	-	-
BT15	±15° (±75°)	41.2	27.9	202.0 ± 7.3	114.2 ± 3.3	0.25 ± 0.03	51.4 ± 6.9	202.3 ± 3.8	126.5 ± 14.9
BT30	±30° (±60°)	34.0	31.4	131.5 ± 9.1	68.9 ± 8.3	0.37 ± 0.04	50.7 ± 11.4	127.3 ± 29.7	82.7 ± 9.6

The average values of FVC and open porosity e' from these three batches in Table 7.1 are calculated and summarized in Table 7.2.

Table 7.2: average values of FVC and e' from three typical tested WHIPOX™ composites with winding angles ±3°/±87° (WF3), ±15°/±75° (BT15) and ±30°/±60° (BT30) in Table 7.1.

Average fiber volume content [%]	Average porosity [%]
39.3	27.1

In fiber direction (1-direction), the overall mechanical response is largely determined by the properties of fibers and FVC. Therefore, each computed value of E_1^T and E_1^C was scaled by the average FVC of 39.3 % in Table 7.2. On the other hand, in transverse direction (2-direction), the overall mechanical behavior is primarily affected by the properties of the matrix phase, which is related to its average porosity. E_2^T and E_2^C were scaled by e' of 27.1 % (Table 7.2). The calculated properties of the equivalent UD-layers were used for the prediction and further comparison of elastic properties in different batches (Table 6.1).

In contrast to the other constants of the equivalent UD-layer, the Young's modulus transverse to the fiber direction showed a strong dependence on the winding angle of tested composites: the average value E_2^T and E_2^C of large angles such as ±30° and above is only about half of the ±3°or ±15°. This behavior can be explained by the shrinkage cracks observed in the matrix (see section 4.2 Microstructural investigation: shrinkage cracks). Based on the microstructure analysis of matrix cracks, a transition line between the matrix with and without cracks can be found in the winding angle of ±30° in Figure 4.4. No cracks were observed for smaller winding angles. WHIPOX™ with the winding angles ±30° through ±45° showed similar crack distributions. Additionally, different mechanical constants under tensile and compression loading have been calculated. Therefore the evaluation of the properties of the equivalent UD-layer was divided into two classes considering the differences in fiber orientations: WHIPOX™ with matrix cracks and WHIPOX™ without matrix cracks. Two UD-material parameter sets with different E_1^T, E_2^T and E_1^C, E_2^C values were defined in Table 7.3. The UD-layer parameter set UD-WC (an UD-layer with cracks) was defined for the angles ±45° to ±30° and a second parameter set, UD-NC (an UD-layer no cracks), with the higher values of E_2^T and E_2^C for angles smaller than ±30°. ν_{12} and G_{12} are computed through all fiber orientations for UD-WC and UD-NC. Since the material showed different behavior under tensile and compression load, the Young's moduli E_1^T and E_1^C with small differences have been listed in Table 7.3. E_2^T and E_2^C were calculated from the respective winding angles in batches WF3, BT15 and BT30 in Table 7.1. The E_2^T value (56.2 GPa) and the E_2^C value (79.7 GPa) for UD-WC are almost 50 % smaller compared to the E_2^T under tensile (107.8 GPa) and the E_2^C under compression load (124.0 GPa) taken from UD-NC group without micro-cracks.

Table 7.3: Calculated elastic constants for equivalent UD-layers with consideration of average fiber volume content and porosity in Table 7.2; UD-WC corresponds to winding angles of ±45° to ±30° and UD-NC applies to angles smaller than ±30°. Winding angle ±30° is the turning point.

Elastic constants	E_1^T [GPa]	E_2^T [GPa]	ν_{12} [-]	G_{12} [GPa]	E_1^C [GPa]	E_2^C [GPa]
UD-WC	211.2	56.2	0.20	40.0	202.4	79.7
UD-NC	211.2	107.8	0.20	40.0	202.4	124.0

7.1.2 Modeling the elastic properties of WHIPOX™ without Ω

By using the elastic constants for the equivalent UD-layers of UD-WC and UD-NC in Table 7.3, computations were performed through CLT (see section 5.1) on symmetric wound WHIPOX™ composites (winding angle $\pm\theta°$ in Figure 5.3b). The elastic constants calculated from the different parameter sets UD-WC and UD-NC under tensile and compression loading are plotted in Figure 7.1 with dependence on the winding angle. The black symbols are the original experimental data and the curves are the predicted variations of the elastic constants of wound WHIPOX™ material. Due to the changes in microstructure, a distinct turning point at ±30° (±60°) can be observed in the curves in Figure 7.1. E_x^T, E_y^T, G_{xy} and ν_{xy} in Figure 7.1a and E_x^C and E_y^C in Figure 7.1b are in accordance with the respective experimental data for winding angle ±3°/±87° (WF3), ±15°/±75° (BT15) and ±30°/±60° (BT30) under tensile loading (Figure 7.1a) and compression loading (Figure 7.1b), respectively. Furthermore, a good agreement between test and modeling results can be observed in the magnification of dash-lined region at ±30° in Figure 7.1a, which confirmed that the modeling of mechanical properties should be divided into two classes: the first being for WHIPOX™ with matrix cracks (WC) and the second as WHIPOX™ without matrix cracks (NC). The Poisson's ratio ν_{xy} and shear modulus G_{xy} are identical for tensile and compression load. It should be noticed that, due to the symmetry of the winding angle of the sample, the values of E_x^T from 45° to 90° are equal to the values of E_y^T from 0° to 45°. As expected from CLT the shear modulus G_{xy} and G_{yx} are identical and the Poisson's ratio ν_{yx} is not a independent constant and can be calculated through $(E_y\nu_{xy})/E_x$. Therefore, only the experimental results from 0° to 45° for shear modulus and Poisson's ratio are shown in Figure 7.1.

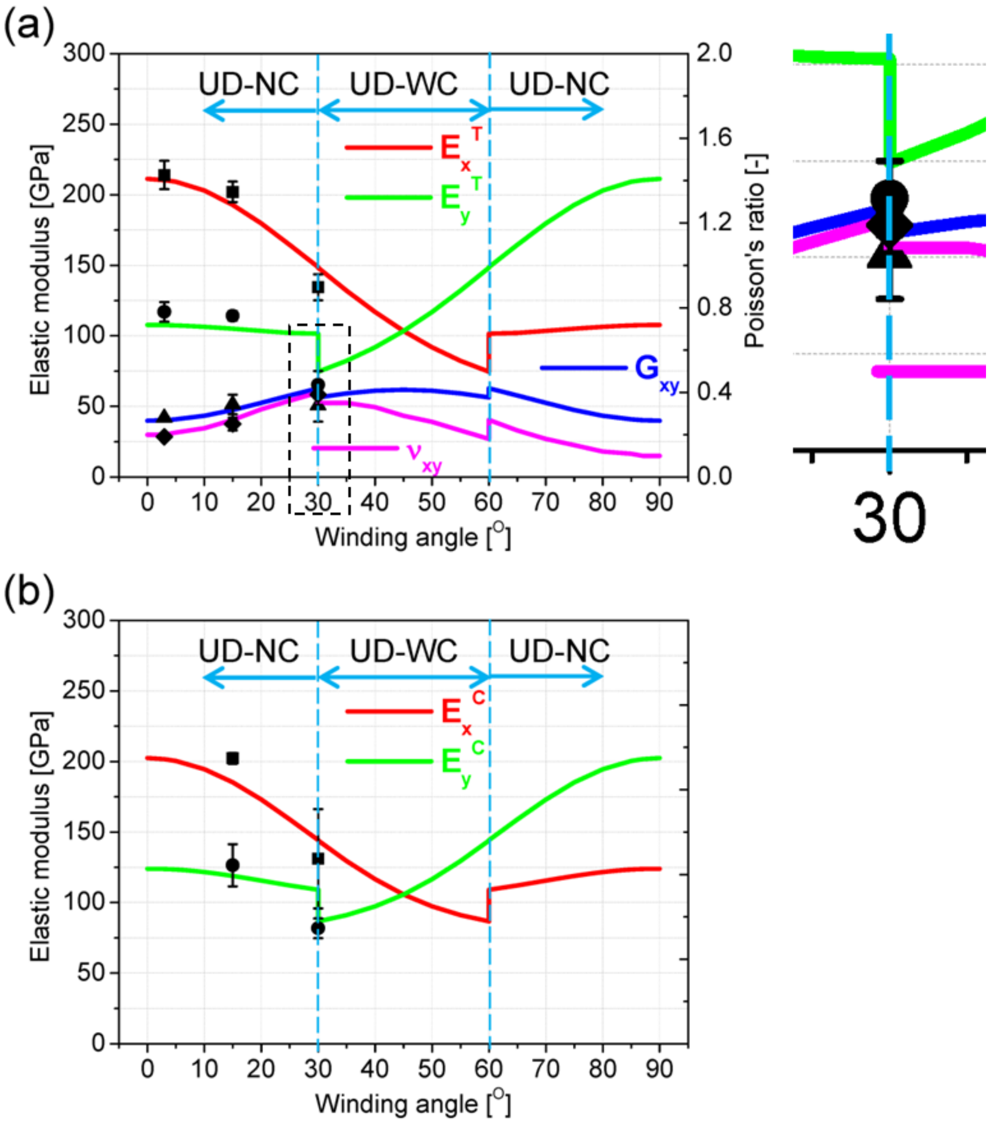

Figure 7.1: Original experimental data (black symbols) from tensile and compressive tests and predicted variation of the elastic constants (curves) for wound WHIPOX™ material depending on the winding angle: a) calculated with UD-properties under tensile load and magnification of dash-lined region at ±30°; b) calculated with UD-properties under compression load. Poisson's ratio ν_{xy} and shear modulus G_{xy} are identical for tensile and compression loading.

7.1.3 Modeling the elastic properties of WHIPOX™ with Ω

In order to upgrade the analytical approaches with consideration of fiber volume content, open porosity and loading direction of different batches, the principle mentioned in section 5.5 was used to calculate the manufacturing factor Ω_k for the individual layer k. Figure 7.2 shows the basic curve of the manufacturing factor Ω_k through modified mixing rules as a function of fiber volume content FVC_k, open porosity e'_k and the angle between the fiber orientation of the layer k and occurring stress. With the exemplary constant values of Property A and Property B, manufacturing factor Ω_k showed a linear behavior from the angle between the fiber orientation of the layer k to the perpendicular direction of the occurring stress ($Proportion\ of\ B$). In this case, when the $Proportion\ of\ B$ equals 0 % the occurring stress is in the fiber direction ($\theta_k = 0°$) and when 100 % the occurring stress is perpendicular to the fiber orientation ($\theta_k = 90°$).

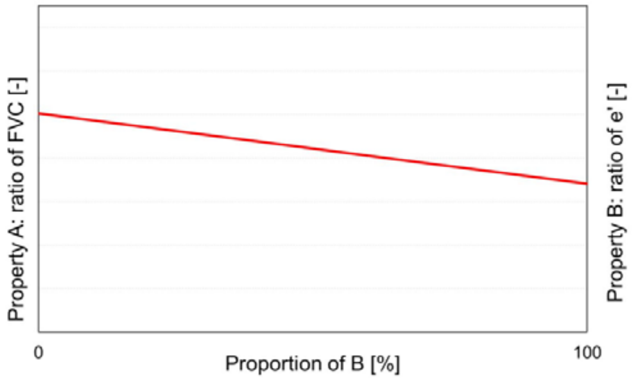

Figure 7.2: Calculated manufacturing factor through modified mixing rules as a function of FVC, porosity e' and angle θ between fiber orientation of the layer k and occurring stress. Computed for exemplary values of property A ratio of FVC, Property B ratio of e$'$ and $Proportion\ of\ B$ the angle between the fiber orientation of the layer k to the perpendicular direction of the occurring stress.

In order to calculate the value of manufacturing factor Ω_k for different WHIPOX™ batches, the average values in Table 7.2 have been used. To compare the test data and calculated elastic constants with consideration of Ω_k, further experimental results from different batches with non-orthogonal (±15°/±75° and ±30°/±60°) and orthogonal winding angles (±45° and 0°/90°) are summarized in Table 7.4. The experimental tests for the batches WF15, WF30, WF45 and WF090 with orientations from ±15°/±75° to 0°/90° were conducted in the Institute of Materials Research, German Aerospace Center Cologne. The tests applied to batch BR30 were conducted by the Advanced Ceramics Group, University of Bremen and the results have been taken from [128]. The indices x and y correspond to the indications from Figure 4.1b. The index T denotes tensile testing. For orthogonally wound WHIPOX™ the Young's modulus E_x is equal to E_y. Identical methods for the measurement of FVC and e' from section 3.2 have been used for the different batches and the results are shown in Table 7.4. Batches WF45 and WF090 were tested in different directions but prepared from the same plate, therefore, identical FVC and e' have been listed in Table 7.4.

Table 7.4: Elastic constants in directions x and y obtained from tensile and Iosipescu-shear tests for WHIPOX™ with different winding angles. The experimental tests on batches of WF were conducted in Institute of Materials Research, German Aerospace Center Cologne and batch BR30 at the Advanced Ceramics Group, University of Bremen.

	Batch	Test direction	FVC [%]	e' [%]	E_x^T [GPa]	E_y^T [GPa]	ν_{xy} [-]	G_{xy} [GPa]
Non-Orthogonal	WF15	±15° (±75°)	27.3	26.7	153.0 ± 3.0	96.0 ± 3.0	0.28 ± 0.01	-
	WF30	±30° (±60°)	35.3	28.3	141.0 ± 4.0	94.0 ± 4.0	0.29 ± 0.01	-
	BR30 [128]	±30° (±60°)	38.6	28.4	144.9 ± 15.5	83.6 ± 5.2	0.34 ± 0.07	59.8 ± 1.5
Orthogonal	WF45	±45°	35.2	33.1	89.0 ± 7.0	89.0 ± 7.0	-	-
	WF090	0°/90°			105.0 ± 8.0	105.0 ± 8.0	0.08 ± 0.02	-

By using the equation 5.81 presented in section 5.5, the manufacturing factor Ω was calculated for the batches listed in Table 6.1 and Table 7.4. The fiber orientation was symmetrical to the test direction in non-orthogonal samples. Therefore, the Ω_k for each individual layer is identical to the Ω for the whole laminate. The results in Figure 7.3 show a maximum Ω equal to 1.31 for batch BT225 in the y-direction, which has relatively low porosity (18.5 %). They also show a minimum value of 0.73 for batch WF15 in the x-direction due to the low FVC (27.3 %). Ω equal to 1 means that the tested samples have a FVC of 39.3 % and a porosity e' of 27.1 % compared to the average values listed in Table 7.2. In a batch with a fiber orientation asymmetrical to the test direction, the Ω_k of each layer can be different. In laminate BT090 the Ω_k is 1.03 in layer 0° and 0.93 for 90°. The effects of Ω_k on the off axis test 0°/60° are 0.87 in 0° and 0.82 in 60°. With batch WF090 the Ω_k in 0° and 90° is 0.90 and 0.82, respectively. The results of the manufacturing factor Ω in Figure 7.3 show that, due to the variations in the manufacturing process of CMCs the FVC and open porosity e' scatter in a wide range by different batches; the factor Ω with consideration of different fiber volume contents, porosities and the angles between fiber orientation and occurring stress can be used to qualify uncertainties in the laminate during the manufacturing process. The effect of the Ω for the modeling results are presented in the following diagrams.

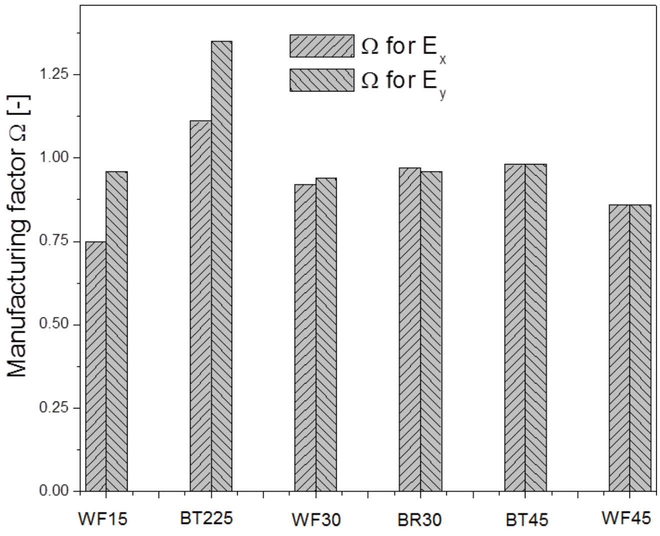

Figure 7.3: Manufacturing factor Ω for the batches with different FVC, open porosity e' and angle between fiber orientation and occurring stress.

The experimental data E_x^T and E_y^T from different batches (Table 6.1 and Table 7.4) and the predicted variation in the elastic constants under tensile load are shown in Figure 7.4. The grey points for WF3 (±3°), BT15 (±15°) and BT30 (±30°) from Table 7.1 have already been shown in Figure 7.1a, which show a good agreement between test and modeling results. However, the black symbols for BT225 (±22.5°) and BT45 (±45°) from Table 6.1 and WF15 (±15°), WF30 (±30°), BR30 (±30°) and WF45 (±45°) from Table 7.4 are distributed within a certain range (Figure 7.4) of the predicted variations of the elastic constants (curves), especially batches WF15 (±15°) and BT225 (±22.5°). Following the analysis of the shrinkage cracks with the boundary line between the data sets of UD-WC and UD-NC in Figure 4.4, strong correlation is seen between the measured and predicted Young's moduli E_y^T in the magnification of dash-lined region at ±30 of Figure 7.4b. Batch WF30 without shrinkage cracks showed the highest E_y^T, while the Young's modulus in the y-direction from batch BT30 with a similar crack density as ±45° showed the lowest (see section 4.2). Sample BR30 with some cracks lies between these two batches. As discussed above, due to the symmetry of the winding angle of the coupons, only the results from 0° to 45° are shown in Figure 7.4.

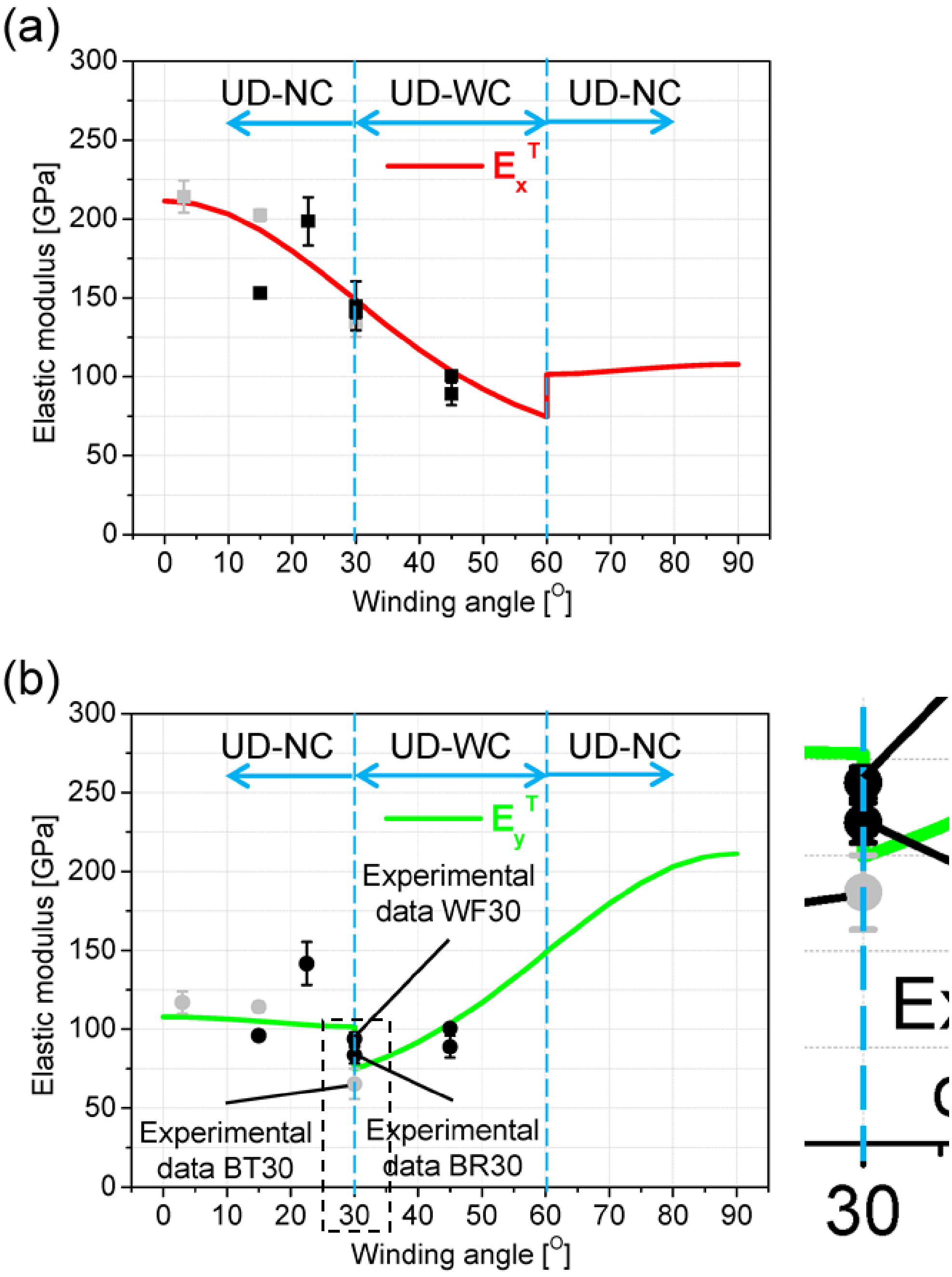

Figure 7.4: Original experimental data (symbols) from different batches and predicted variation of elastic constants under tensile load (curves) for wound WHIPOX™ material depending on the winding angle: a) calculated E_x^T values with UD-properties; b) calculated E_y^T values with UD-properties and magnification of dash-lined region at ±30°.

Similar curves with experimental data from different batches and predicted variations of the elastic constants under compression load are plotted in Figure 7.5. The grey points for BT15 (±15°) from Table 7.1 have already been shown in Figure 7.1b with a good agreement between test and modeling results. In comparison, the black symbols for BT225 (±22.5°) from Table 6.1 are distributed in Figure 7.5 and display large fluctuation when compared to the predicted curves.

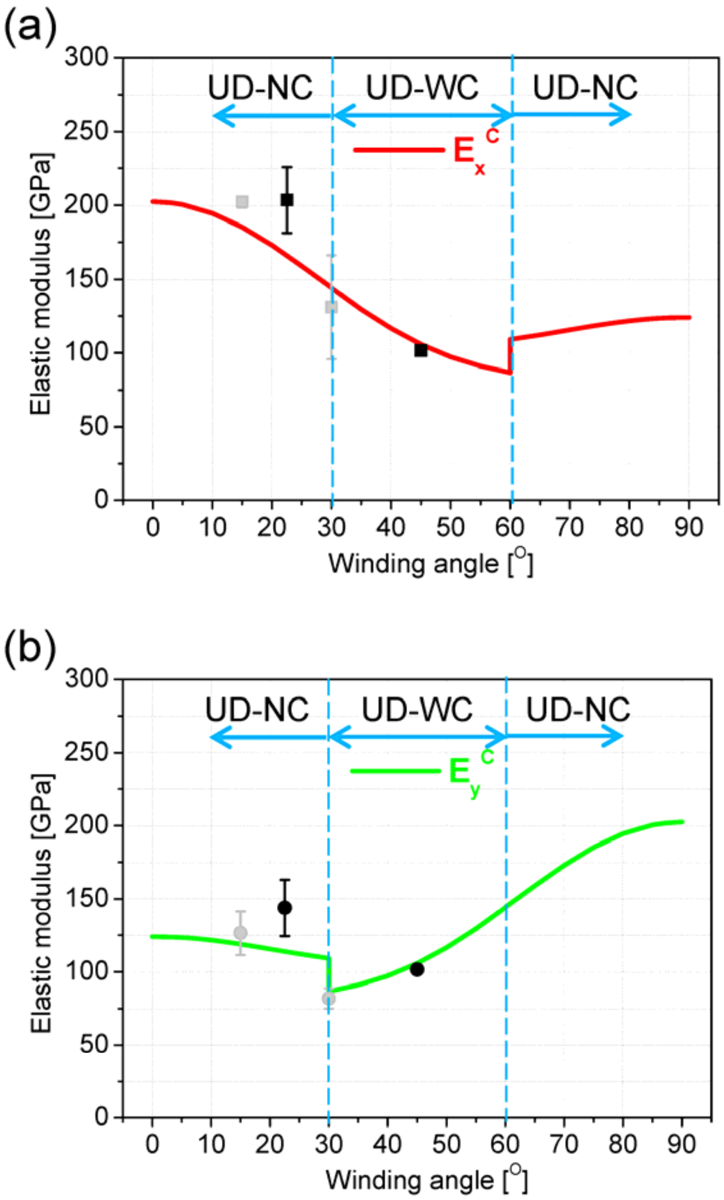

Figure 7.5: Original experimental data (symbols) from different batches and predicted variation of the elastic constants under compression load (curves) for WHIPOX™ material depending on the winding angle: a) calculated E_x^C values with UD-properties; b) calculated E_y^C values with UD-properties.

Based on the results in Figure 7.4 and Figure 7.5, the modeling approach without consideration of Ω provides an insufficient prediction of elastic properties for batches with different FVC and e'. In this case, equations 5.82 to 5.84 in section 5.5 have been used to calculate the sub-matrices: strain stiffness $[S_{ij}]$, coupling stiffness $[C_{ij}]$ and bending stiffness $[B_{ij}]$. It should be noted that the inelastic deformation factor *Δ* in equations 5.82 to 5.84 is equal to 1.0 for the modeling within the linear elastic area. The comparison between calculated elastic constants (with and without consideration of Ω) and the test results (from Table 6.1 and Table 7.4) for wound WHIPOX™ is visualized in Figure 7.6. A very close correlation is shown in Figure 7.6a to Figure 7.6c for the measured and predicted elastic values with the maximum difference of 12 % through the application of the manufacturing factor Ω. On the other hand, the computation of elastic properties without consideration of varying FVC and open porosity e' values, i.e. without consideration of

Ω, could deviate strongly from the experimental results. This is particularly true for the batch BR30 with some shrinkage cracks. Therefore, instead of using UD-WC or UD-NC properties, the average values from UD-WC and UD-NC have been applied to predict elastic constants of the batch BR30.

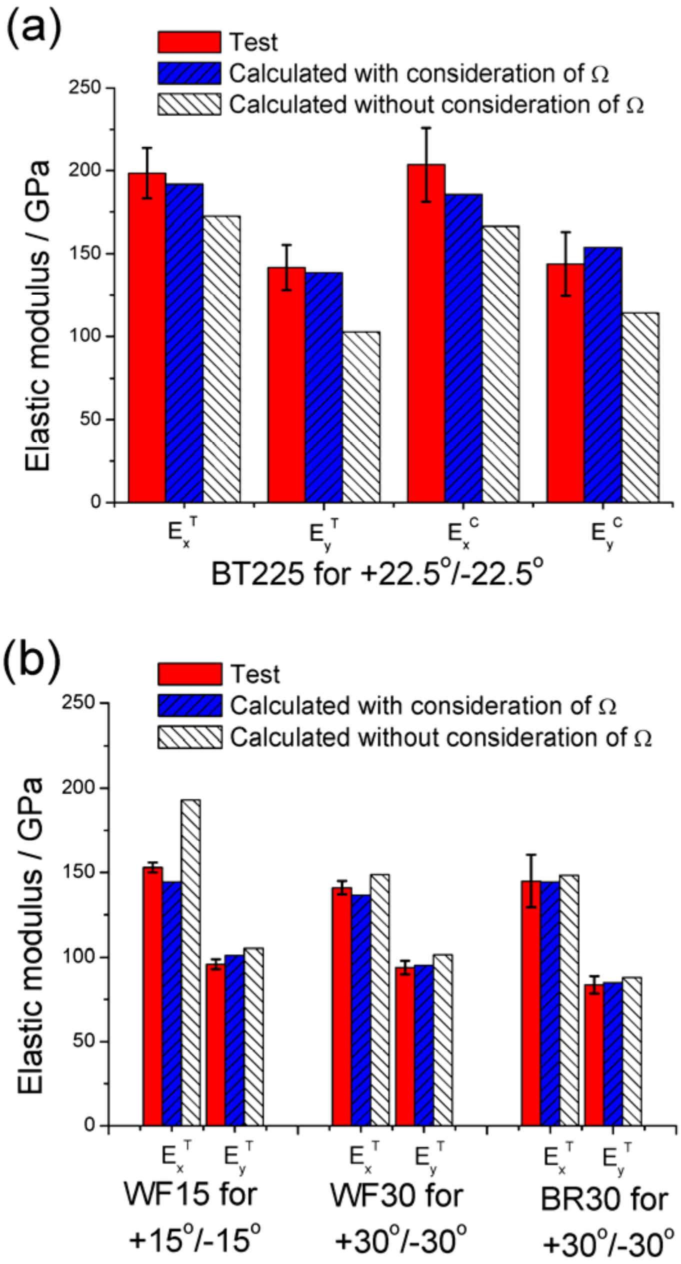

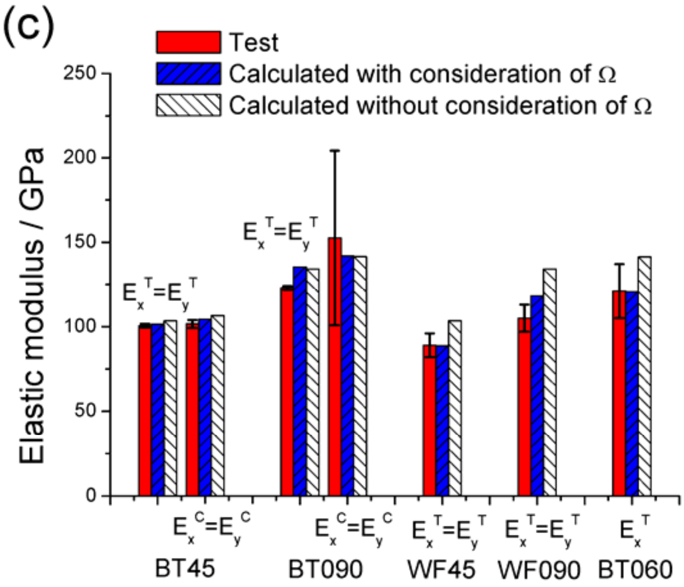

Figure 7.6: Comparison of calculated elastic constants with and without consideration of Ω to test results for wound WHIPOX™ from different batches: a) Young' modulus of non-orthogonal samples BT225 (±22.5°) under tensile and compression load; b) Young' modulus of non-orthogonal samples WF15 (±15°), WF30 (±30°) and BR30 (±30°) under tensile and compression load; c) Young' modulus of orthogonal samples BT45 (±45°), BT090 (0°/90°), WF45 (±45°) and WF090 (0°/90°) and off axis test BT060 (0°/60°) under tensile and compression load.

As described in section 5.5, the shear modulus G_{xy} and the Poisson's ratio ν_{xy} are calculated without consideration of Ω. A strong correlation between the test results and the calculated values of G_{xy} and ν_{xy} can be observed in Figure 7.7a and b.

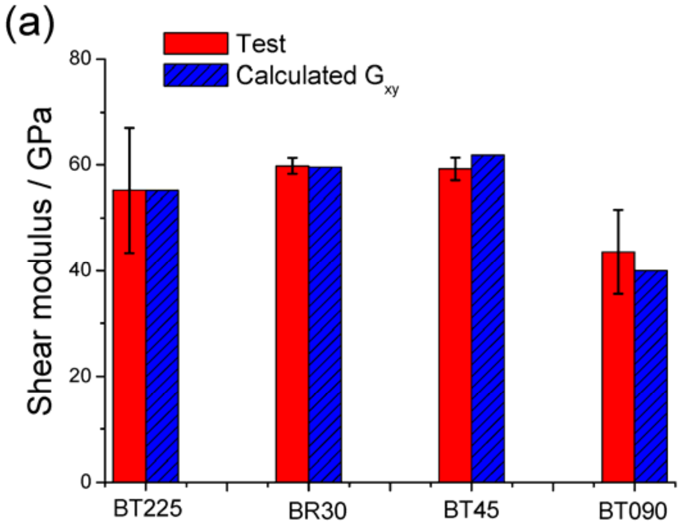

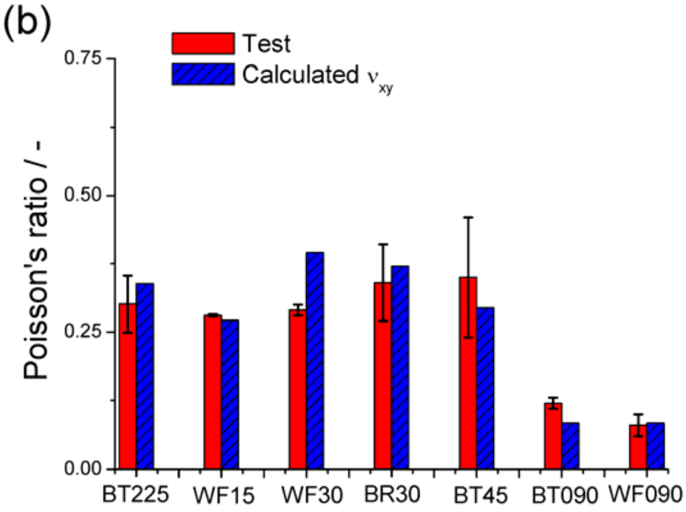

Figure 7.7: Comparison of calculated elastic constants to test results for wound WHIPOX™ from different batches: a) shear modulus non-orthogonal and orthogonal samples; b) Poisson's ratio of non-orthogonal and orthogonal samples.

7.2 Modeling of failure stresses and failure mode

In this section Tsai-Wu failure criterion in stress space using the failure ratio is used to calculate the failure strength of the investigated material WHIPOX™. The parameters of the Tsai-Wu stress criterion are evaluated considering different microstructures (with and without matrix cracks). The calculated failure strength values are compared to the original experimental results. The modeling approach using this modified definition of the directional failure indices $\sum_{ij}$ has been used to predict the failure mode of WHIPOX™.

7.2.1 Modeling of failure stresses

As mentioned in section 5.3, Tsai-Wu failure criterion in stress space requires the strength properties of the UD-layer.

Due to the lack of matrix and fiber properties within the composite material, it is not reasonable to calculate the strength properties of the virtual UD-layer from the individual properties of matrix and fiber. Furthermore, the production and characterization of the actual UD-layer for CMCs is also critical because the non-typical unhindered shrinkage of matrix transverse to the fibers during processing leads to material which cannot be considered as representative material. Instead of following those modeling approaches, the strength values of UD-layer were fitted to different test results from the investigated material WHIPOX™. The approximated strength properties with the inclusion of different micro-structures, UD-WC (UD-layer with cracks) and UD-NC (UD-layer no cracks) (see section 4.2), are enumerated in Table 7.5. The indices 1 and 2 correspond to the indications in Figure 5.3a where 1 is in the fiber direction and 2 is transverse to the fiber direction. The index T denotes the tensile test and C the compression test, while τ_{12} is the estimated in-plane shear strength.

Table 7.5: The estimated strength values of the equivalent UD-layer of WHIPOX™: UD-WC corresponds to winding angles of ±45° to ±30° and UD-NC applies to angles smaller than ±30°.

Strength	σ_1^T [MPa]	σ_2^T [MPa]	σ_1^C [MPa]	σ_2^C [MPa]	τ_{12} [MPa]
UD-WC	279.0	22.5	-243.0	-45.0	65.0
UD-NC	279.0	22.0	-274.0	-120.0	85.0

All the parameters of the Tsai-Wu failure criterion in stress space can be evaluated through the aforementioned equations in section 5.3.1 by using the estimated strength values in Table 7.5. These parameters are also dependent on the different micro-structure for UD-WC and UD-NC and are listed in Table 7.6.

Table 7.6: Tsai-Wu parameters in stress space of the equivalent UD-layer of WHIPOX™: UD-WC corresponds to winding angles of ±45° to ±30° and UD-NC applies to angles smaller than ±30°.

Tsai-Wu Parameters	F_1	F_{11}	F_2	F_{22}	F_{66}
UD-WC	-5.3E-04	1.5E-05	2.2E-02	9.9E-04	2.4E-04
UD-NC	-6.5E-05	1.3E-05	3.7E-02	3.8E-04	1.4E-04

The parameters listed in Table 7.6 can be put into the Tsai-Wu equation in stress space (section 5.3.1). It should be noticed that, In the case of the investigated WHIPOX™ material, the interaction term F_{12} has been set to zero due to the lack of the possibility of production of real unidirectional layer and bi-axial tensile testing. The Influence of F_{12} on the shape of the Tsai-Wu failure envelope of WHIPOX™ will be discussed in section 8.1. A 3D visualization with help of MATLAB R2013a for WHIPOX™ depicting with (red envelope) and without matrix cracks (grey envelop) shows in Figure 7.8. It outlines the failure regions of these two different groups.

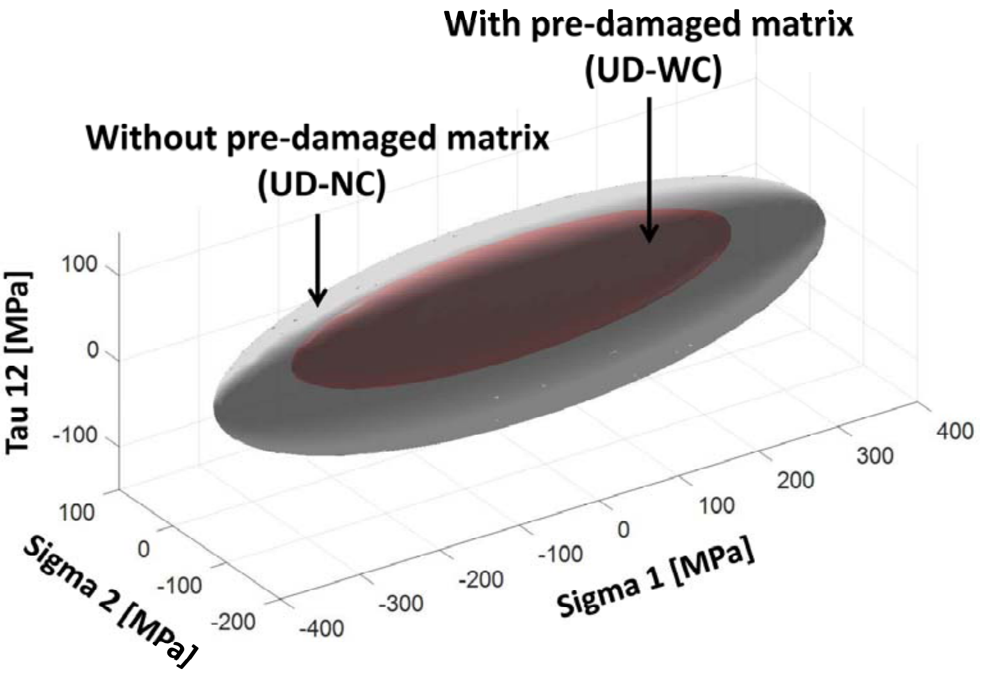

Figure 7.8: 3D representation of Tsai-Wu failure criterion in stress space for material WHIPOX™ depicting with (red envelope) and without matrix cracks (grey envelope).

By using the strength ratio *R* of the Tsai-Wu failure criterion, which has been presented in 5.3.1, the tensile and compressive strengths of the laminate with a symmetric fiber orientation can be predicted. Figure 7.9a und b show the test results (from Table 6.2) with different fiber orientations and calculated failure strengths for the material WHIPOX™. This is depicted with (UD-WC) and without the matrix cracks (UD-NC) under tensile and compression loading. The modeling curves in Figure 7.9 are the results calculated without consideration of the manufacturing factor Ω for different batches. Similar to the modeling of elastic properties, a distinct inconsistency at ±30° (±60°) can be observed in the curves due to the changes in microstructure.

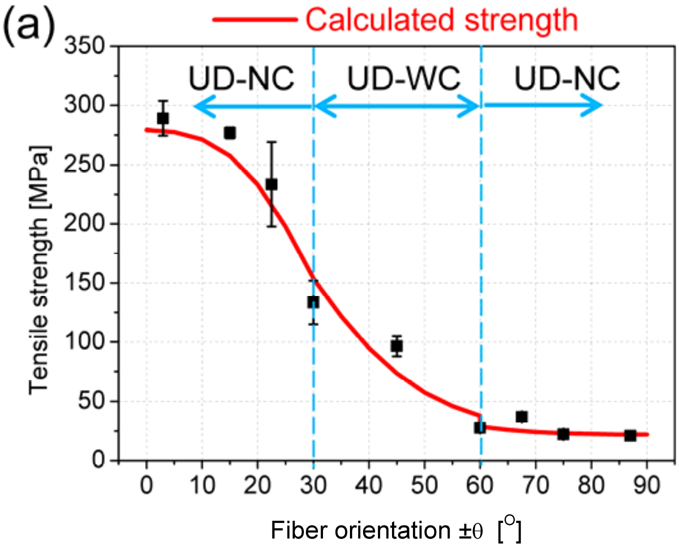

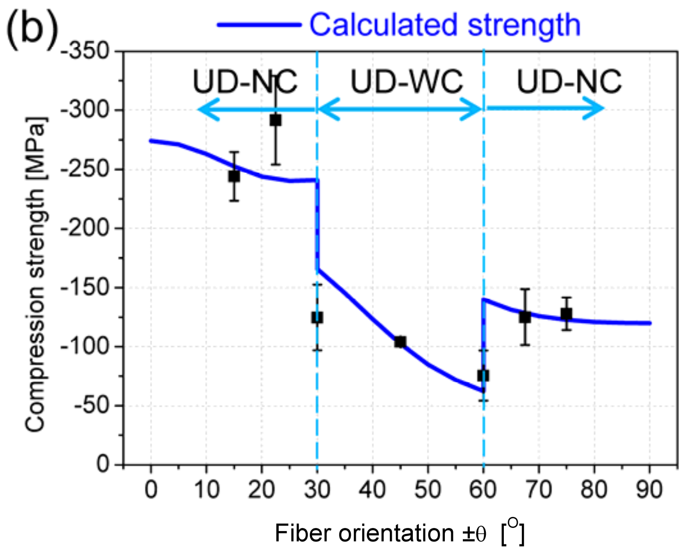

Figure 7.9: Original experimental data with different fiber orientation (black symbols) and predicted failure strength (curves) for wound material WHIPOX™ depicting with (UD-WC) and without matrix cracks (UD-NC) under a) tensile loading and b) compression loading.

Although a relatively good correlation between the modeling results and some experiments can be observed in Figure 7.9, in order to upgrade the analytical approach with consideration of fiber volume content and open porosity from different batches, the manufacturing factor Ω value is coupled with individual sub-matrices for the modeling of failure strength. It leads to a more precise prediction of failure strength (Figure 7.10). Modeling of the strength value of the laminate with successive ply failures (e.g. with the fiber orientation 0°/90° and 0°/60° in Table 6.2) cannot be directly obtained from the strength ratio R. Their results are presented in the following section 7.3 with the inclusion of the non-linear behavior of investigated WHIPOX™ as a factor.

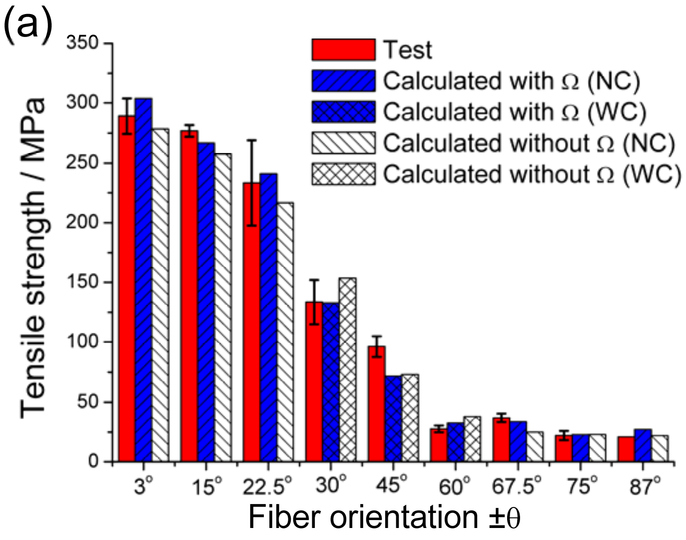

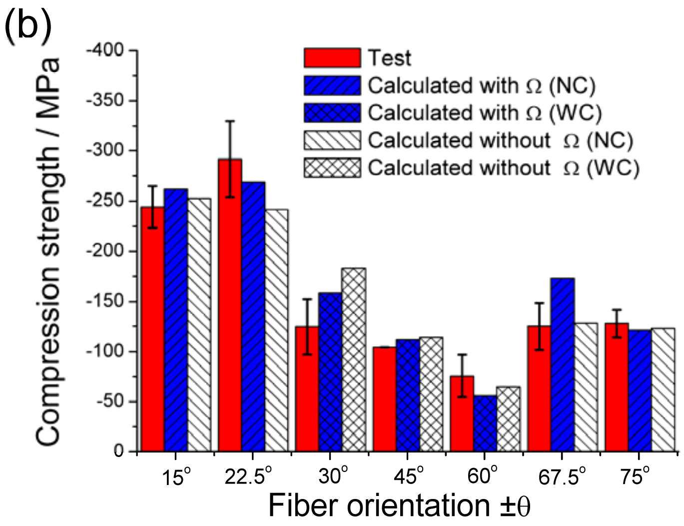

Figure 7.10: Comparison of calculated failure strength with and without consideration of manufacturing factor Ω to test results of wound WHIPOX™ under a) tensile loading and b) compression loading.

7.2.2 Modeling of failure mode

By using the modeling approach presented in section 5.3.4, directional failure indices Σ_{ij} of the investigated material WHIPOX™ can be calculated for the modeling of failure mode. The calculation of failure indices Σ_{ij} is focused on the test results of specimens with symmetric fiber orientation under tensile loading. This is because most compression samples were totally destroyed after the test. Due to the relatively low compressive strength the shear specimens fail locally in the testing rig where high compressive stresses prevail (see section 6.1). Therefore, the failure modes of compression and shear specimens are not discussed in this section. To explain the performance of modeling approach for failure mode, directional failure indices Σ_{ij} (equations 5.73 to 5.75 in section 5.3.4) of tensile samples with the fiber orientation of ±15° have been first calculated as examples. The predicted failure tensile strength of the wound WHIPOX™ laminate ±15° is approx. 267 MPa (see Figure 7.10a). Under this loading, the failure indices Σ_{11}^{2D}, Σ_{22}^{2D} and Σ_{12}^{2D} for their respective stress components σ_{11}, σ_{22} and τ_{12} are all equal to 1.0 in the failure event. The one-dimensional failure indices Σ_{ij}^{1D} are calculated with the separate stress components σ_{ij} and the approximated strength values of the UD-layer for WHIPOX™ (see Table 7.5): $\Sigma_{11}^{1D} = |257.9/279.0| = 0.92$; $\Sigma_{22}^{1D} = |-0.3/22.0| = 0.01$ and $\Sigma_{12}^{1D} = |-34.0/85.0| = 0.40$. With this information, the directional failure indices Σ_{ij} of WHIPOX™ with winding angle ±15° can be calculated as follows:

$$\Sigma_{11} = \frac{\Sigma_{11}^{2D}}{1 + (\Sigma_{11}^{2D} - \Sigma_{11}^{1D})} = \frac{1.0}{1 + (1.0 - 0.92)} = 0.93$$

$$\Sigma_{22} = \frac{\Sigma_{22}^{2D}}{1 + (\Sigma_{22}^{2D} - \Sigma_{22}^{1D})} = \frac{1.0}{1 + (1.0 - 0.01)} = 0.50$$

$$\Sigma_{12} = \frac{\Sigma_{12}^{2D}}{1 + (\Sigma_{12}^{2D} - \Sigma_{12}^{1D})} = \frac{1.0}{1 + (1.0 - 0.40)} = 0.62$$

It should be noticed that the directional failure indices $\sum_{ij}$ are calculated separately and show the "relative importance of the separate stress components σ_{ij} in the failure event" ([18]). In this case of fiber orientation ±15°, the values of $\sum_{11}$ (0.93), $\sum_{22}$ (0.50) and $\sum_{12}$ (0.62) indicate that $\sum_{11}$ will be mainly responsible for the failure in this particular example.

Table 7.7: The directional failure indices $\sum_{ij}$ of the investigated material WHIPOX™ with different fiber orientations.

Directional failure indices	±15°	±22.5°	±30°	±45°	±60°	±67.5°	±75°
$\sum_{11}$	0.93	0.81	0.68	0.56	0.48	0.48	0.22
$\sum_{22}$	0.50	0.53	0.59	0.80	0.94	0.99	1.00
$\sum_{12}$	0.62	0.69	0.80	0.70	0.59	0.53	0.52

The estimated directional failure indices $\sum_{ij}$ of the investigated material WHIPOX™ with different fiber orientations have been summarized in Table 7.7. In order to compare the test results, some typical failure surfaces of the investigated material WHIPOX™ with different fiber orientations have been shown in Figure 7.11. For the tensile sample ±15°, the value of $\sum_{11}$ (0.93) is much larger than the values of $\sum_{22}$ and $\sum_{12}$. This leads to a fiber breakage dominant failure surface as seen it in Figure 7.11a. On the contrary, a clear matrix breakage can be obtained in Figure 7.11b with a significantly higher $\sum_{22}$ (1.00) for the winding angle ±75°. In the case of the laminate with ±30°, although the values in Table 7.7 indicate that the $\sum_{12}$ will be mainly responsible for failure in this example, the value of $\sum_{11}$ is also relative high. They lead to a failure surface with combined matrix and fiber breakage in the Figure 7.11c. The failure surface of a tensile sample with the orientation of ±45° in Figure 7.11d shows mainly matrix breakage and a few fiber breakages, which correlates with the calculated higher $\sum_{22}$ and $\sum_{12}$ values for the same winding angle in Table 7.7.

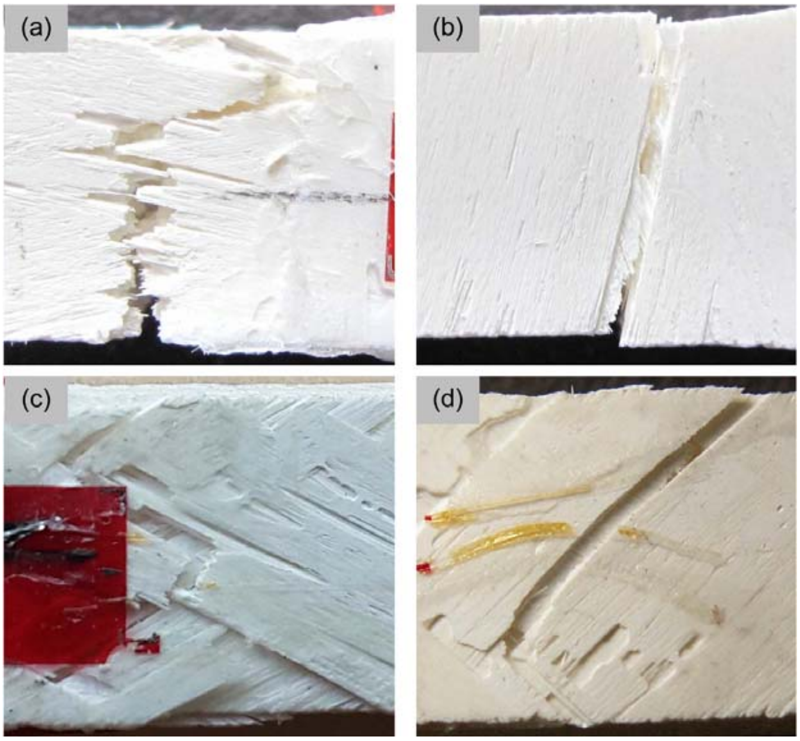

Figure 7.11: Typical failure surface of the investigated material WHIPOX™ with different fiber orientations a) ±15° and b) ±75° and c) ±30° and d) ±45°.

It should be noticed that each of these failure indices $\sum_{ij}$ indicates the direction of failure indices connected with stress components σ_{ij}. Based on the results of this section, the modeling approach using this modified definition of the directional failure indices $\sum_{ij}$ has the great potential to predict which stress component is mainly responsible for failure.

7.3 Modeling of failure strain and successive ply failures

In this section the inelastic deformation factor Δ, which is defined as the relationship between calculated linear strain value ε_{linear} and real failure strain ε_{test} (Figure 5.5), is used to calculate the failure strain of the investigated material WHIPOX™. The value of Δ is discussed and evaluated in light of different microstructures (with and without matrix cracks). The calculated failure strain values and stress-strain behaviors in bilinear-model are compared to the original experiment results. The modeling approach of successive ply failures has been used to predict the material behavior of laminate with several groups of layers and each group has different fiber orientaion.

7.3.1 Modeling of failure strain

The tensile stress-strain curves of WHIPOX™ with fiber orientations of ±30° and ±60° in Figure 6.1b show inelastic behavior up to failure. In this case, the failure strength and strain cannot be directly correlated with the Tsai-Wu failure criterion in stress and strain spaces. Figure 7.12 shows the predicted failure strain (curve) without consideration of the inelastic deformation of the investigated material WHIPOX™. Significant differences between calculated and original experimental results can be observed.

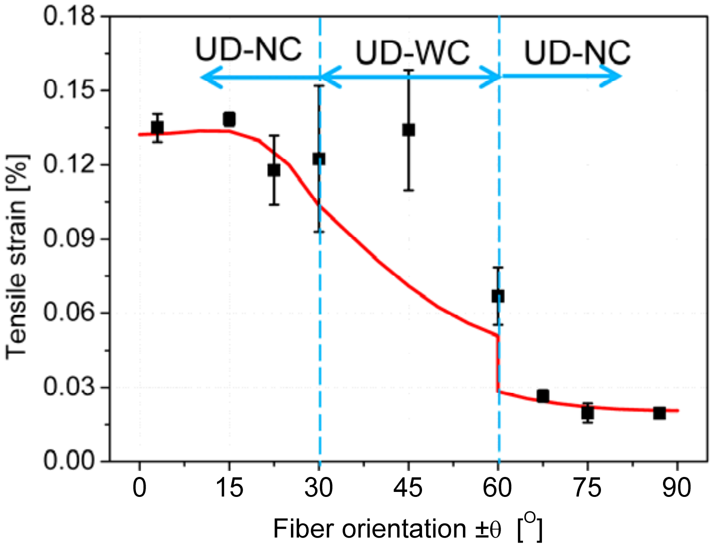

Figure 7.12: Original experimental data with different fiber orientation (black symbols) and predicted failure strain (curve) without consideration of inelastic deformation for wound material WHIPOX™ depicted with matrix cracks (UD-WC) and without matrix cracks (UD-NC).

The inelastic deformation factor Δ presented in section 5.4 is defined as the relationship between calculated linear strain value ε_{linear} and real failure strain ε_{test}: $\Delta = \varepsilon_{linear}/\varepsilon_{test}$ (see equation 5.76). If $\Delta = 1$ then linear elastic behavior up to failure is shown. The calculated values (black symbols) of the inelastic deformation factor Δ from the investigated material WHIPOX™ with different fiber orientations are shown in Figure 7.13. It can be observed that the laminates in the area without matrix cracks (NC) exhibit linear stress-strain behavior with Δ equal to approx. 1.0. In comparison, the value of Δ is strongly dependent on the fiber orientation of the laminate in the area with matrix cracks (WC). A function can be established by fitting the calculated results Δ between ±30° and ±60° in Figure 7.13. The inelastic deformation factor Δ depicting the areas without matrix cracks (NC) and with matrix cracks (WC) is defined as:

$$\begin{gathered} WHIPOX - NC\colon \Delta = 1.0 \\ WHIPOX - WC\colon \Delta = (-6.6E-3)\theta + 1.0 \end{gathered} \tag{7.1}$$

where θ is the angle between fiber orientation and the loading direction.

The different behavior can be explained by the micro structure in the WC area with matrix cracks. The nonlinear behavior is most probably induced by cracks in the matrix under a certain load. The already existing shrinkage cracks in the WHIPOX™-WC matrix show strong dependence on the angle between fiber orientation and the occurring loading. For the WHIPOX™ without matrix cracks, a linear behavior with Δ equal to 1 is expected. In the case of tensile loading in fiber direction of a virtual UD-layer with cracks, the fiber properties are dominated in this direction and the matrix and shrinkage cracks have limited influence. Therefore, the material behavior is assumed as linear elastic up to failure with the value of factor Δ equals to 1.0. This agrees with the calculated results from second part of equation 7.1 with $\theta = 0$. On the other hand, in case of loading in transverse fiber direction, the matrix dominates the mechanical behavior and a significant non-linear behavior with low Δ value can be expected. It is important to note that the evaluation of factor Δ combines features of implicit and explicit models (see section 2.2.2). This model uses both approximation and physically-based methods in order to characterize WHIPOX™ inelastic behavior. The inelastic deformation factor Δ is defined as a mathematical equation that is incorporated into the material modeling relation and solved by using the analysis of microstructure of the investigated material WHIPOX™.

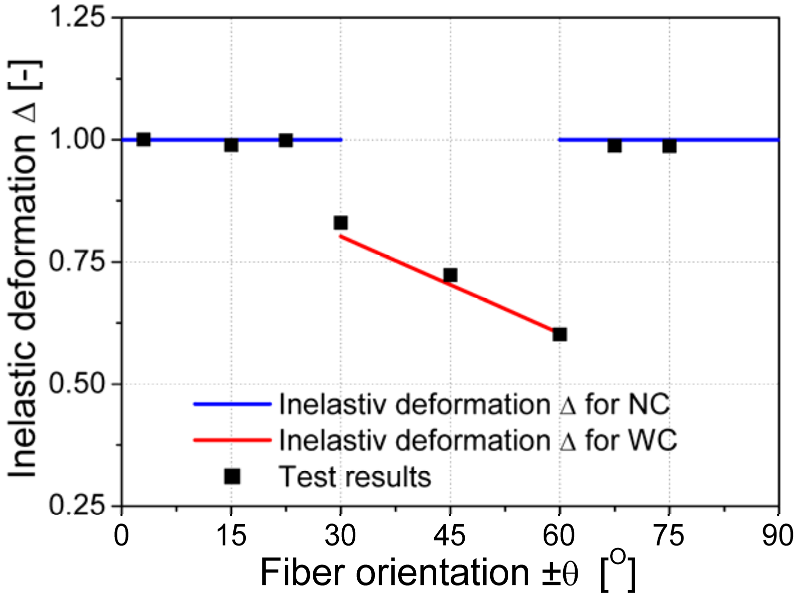

Figure 7.13: Calculated inelastic deformation factor Δ (black symbols) from the investigated material WHIPOX™ with different fiber orientations.

As presented in section 5.4, the factor Δ is assembled into the individual sub-matrices: strain stiffness $[S_{ij}]$, coupling stiffness $[C_{ij}]$ and bending stiffness $[B_{ij}]$, for the calculation of the engineering constants of a virtual equivalent UD-layer of WHIPOX™ (such as E_Δ in Figure 5.5). In this way, the failure strain can be estimated. For WHIPOX™-NC with Δ equals to 1.0, the initial stiffness matrix remains unchanged up to the failure. On the other hand, a bilinear model was used to describe the behavior of WHIPOX™-WC beyond the virtual yield stress σ_Y exhibited in Figure 5.6. σ_Y was defined as the function of inelastic deformation factor Δ and failure strength σ_{test} as $\sigma_Y = \sigma_{test}\Delta$ in equation 5.77.

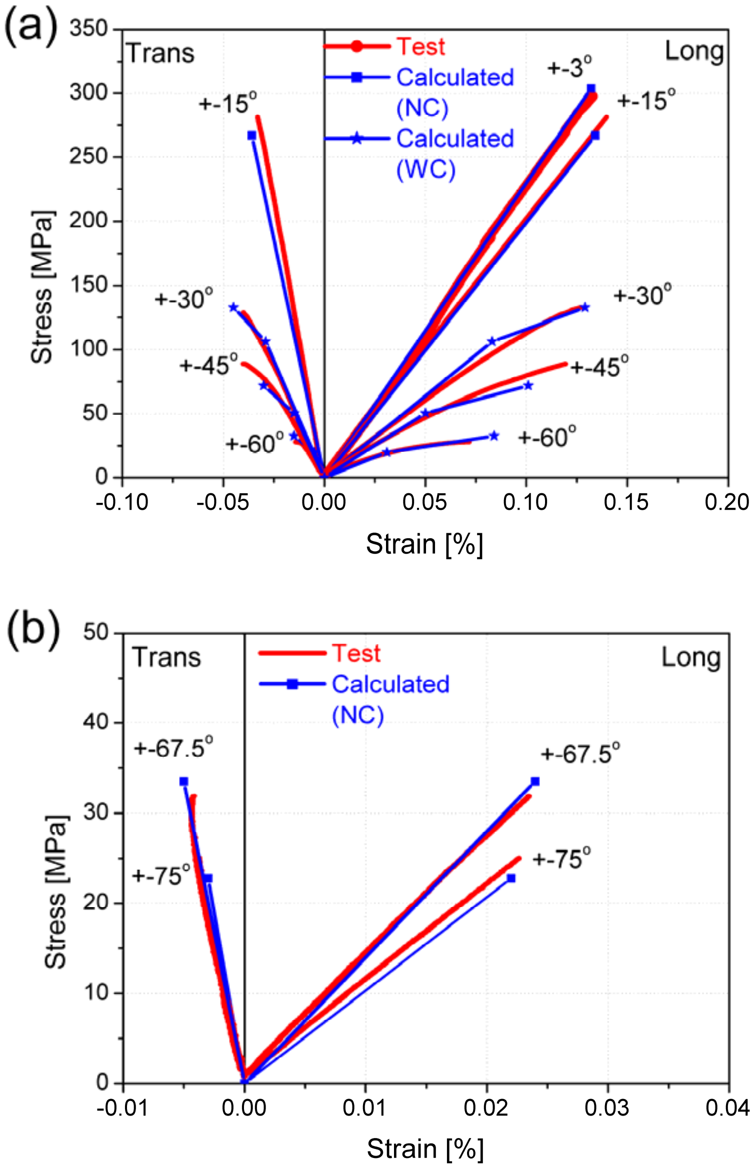

Figure 7.14: Tensile stress-strain comparison diagrams with test results and calculated results for laminate WHIPOX™-NC and WHIPOX™-WC with fiber orientations a) from ±3° to ±60° and b) ±67.5° and ±75°.

The comparison of longitudinal and transverse stress-strain behavior of WHIPOX™-NC and WHIPOX™-WC as seen in test and calculated results are summarized in Figure 7.14. The behavior of fiber orientations ±3° and ±15° (in Figure 7.14a) and ±67.5° and ±75° (in Figure 7.14b) are linear in the laminate of WHIPOX™-NC. The non-linear behavior up to failure of the laminate of WHIPOX™-WC with the fiber orientations ±30°, ±45° and ±60° are compared with the bilinear model results in Figure 7.14a. A bar diagram for the comparison of calculated failure strain depicting WHIPOX™-NC and -WC with the tensile test results for wound WHIPOX™ with different fiber orientations is shown in Figure 7.15. A very close correlation can be observed in Figure 7.14 and Figure 7.15 for the measured and predicted failure strain. Due to the fact that the Ω_k value is coupled with the layer thickness t_k for the calculation of the stiffness matrices $(S_{ij})_{\Delta,\Omega}$, $(C_{ij})_{\Delta,\Omega}$ and $(B_{ij})_{\Delta,\Omega}$ in section 5.5, the influence of different FVC, e' and angle of fiber orientation from different batches has been taken into consideration in the modeling of elastic properties (section 7.1) and strength (section 7.2). Therefore, for the modeling of the strain value, the influence of Ω_k can be hypothesized to $(\Omega_k)(\Omega_k)^{-1}$. As a result the impact of Ω_k on the strain is negligible.

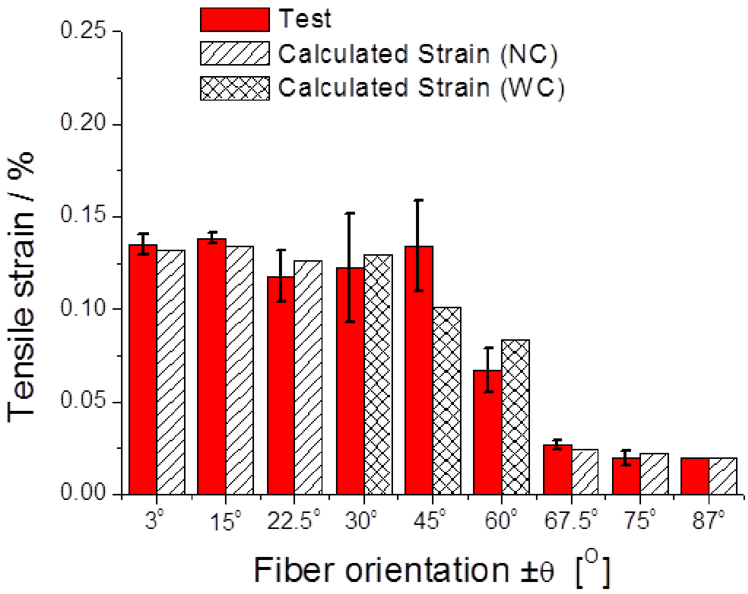

Figure 7.15: Comparison of calculated failure strains of WHIPOX™-NC and WHIPOX™-WC with tensile test results for WHIPOX™ with different fiber orientations.

7.3.2 Modeling of successive ply failures

As presented in section 5.3.3, because of the different fiber orientations to the loading direction from each layer to the other, the different ply groups in a laminate have different mechanical behavior under the same load. In this study, two laminates, batches BT090 and BT060, with the fiber orientations 0°/90° and 0°/60° were examined under tensile loading. The modeling approach with successive ply failure in section 5.3.3 has been used to determine the stress and strain values at different loading states for these two laminates. Specimens from batch BT090 were prepared from the plate BT45 with a winding angle ±45°. Other specimens from batch BT060 were taken from plate BT30 (±30°). This means that these two batches belong to the laminates with matrix cracks (WC).

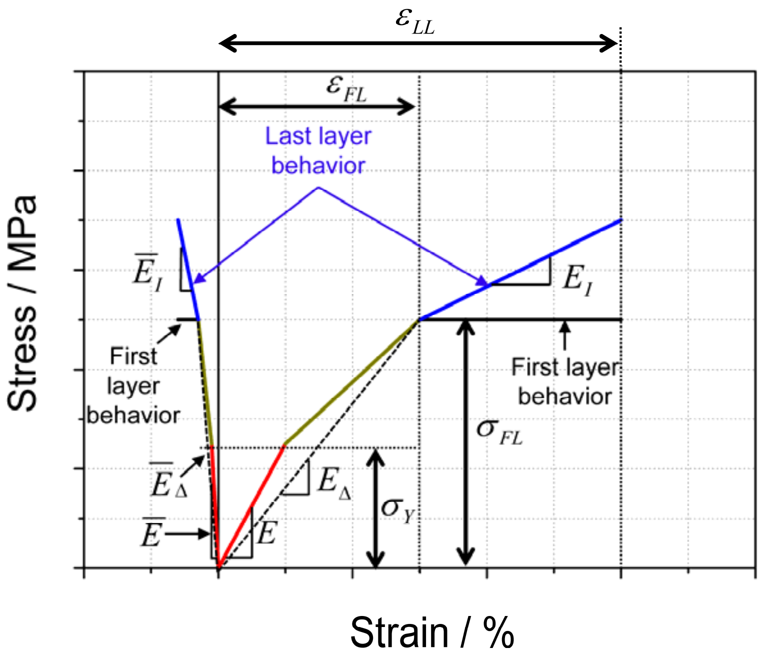

Figure 7.16: Successive ply failures in a laminate with two different ply groups with the non-linear behavior taken into account.

With the non-linear behavior of WHIPOX^{TM}-WC taken into account, the successive ply failure of two different ply groups in a laminate under tensile loading in Figure 5.4 can be added to Figure 7.16. According to the modeling approach in section 5.4 and the calculation of the inelastic deformation factor Δ in section 7.3.1, the ply groups at 90° from batch BT090 and 60° from BT060 exhibit significant non-linear behavior. Therefore, a bilinear model (defined in section 5.4) with the virtual yield stress σ_Y and effective stiffnesses E_Δ and $\bar{E}_\Delta$ (the longitudinal and transverse directions) describes the behavior of laminate before the first-ply-failure (FPF). On the other hand, in the direction with the fiber orientation of 0° in both batches, the material's behavior is described as linear elastic up to failure with the value of factor Δ equals to 1.0. The linear model is shown in Figure 7.16 with the reduced stiffnesses E_I and $\bar{E}_I$ in the longitudinal and transverse directions after obtaining the FPF. The laminate has completely failed when last-ply-failure (LPF) has occurred with the maximum strain value of the last layer ε_{LL}. It should be noted that the strength values σ_{FL} and the strain values ε_{FL} at FPF of two batches are different because of the different strength ratios R between lay groups with 90° and 60° orientation. However, the ultimate strain ε_{LL} of two laminates is identical due to the same orientation of 0° at LPF.

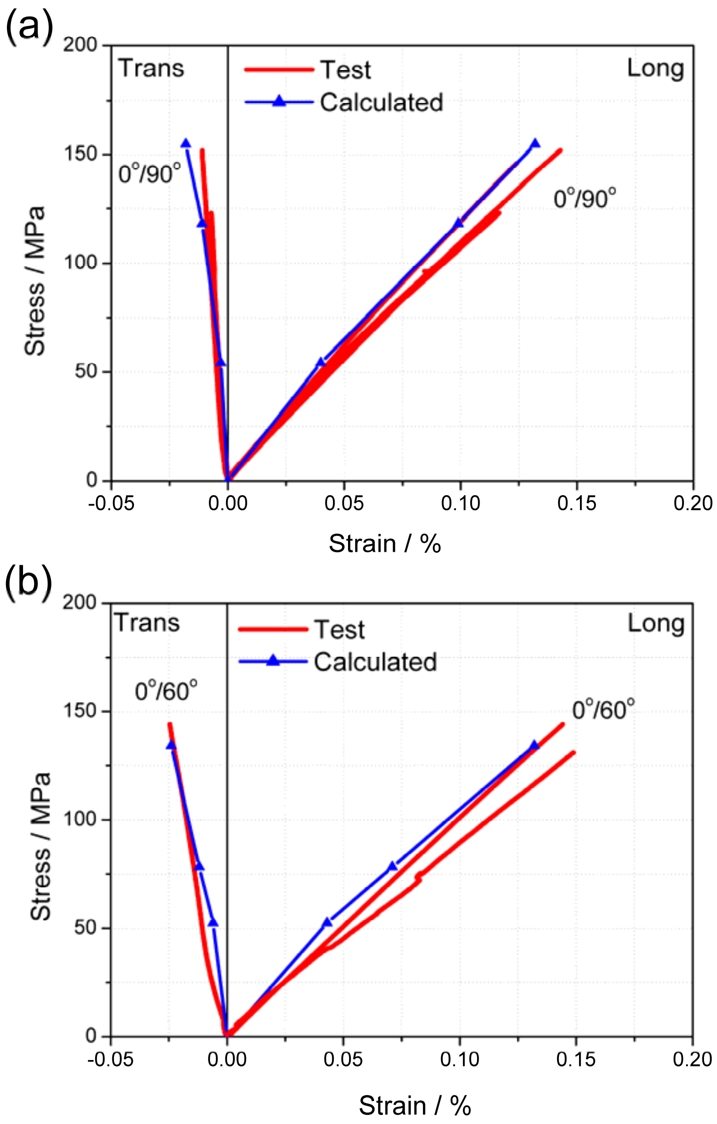

Figure 7.17: The tensile stress-strain comparison diagrams comparing the test results with the calculated results for the successive ply failures of a) batch BT090 (0°/90°) and b) batch BT060 (0°/60°).

The comparison of longitudinal and transverse stress-strain behavior from tensile test and modeling results for batches BT090 (0°/90°) and BT060 (0°/60°) is shown in Figure 7.17. The non-linear behavior up to failure of the laminate is compared with the multi-linear modeling results and shows a strong correlation.

8 Discussion

8.1 Characterization of mechanical properties

The main objectives of this work were the characterization and modeling of the mechanical properties of wound oxide ceramic composites with varied fiber orientations. As fundament of the modeling chain (Figure 5.7), full coverage of the mechanical properties of the investigated material WHIPOX™ in different wound orientations (±3°/±87°, ±15°/±75°, ±22.5°/±67.5°, ±30°/±60° ±45°, 0°/90° and 0°/60°) were evaluated with in-plane tension, Iosipescu-shear and compression tests. The material's characteristic values, including initial stiffness, strength, strain, elastic and inelastic behavior, were used for the modeling of the mechanical properties of the material WHIPOX™ with any desired fiber orientation and different fiber volume contents and porosities.

Based on the results in section 6.2, there is a significant correlation between the detected defects (NDI-tests) and the material properties from the mechanical tests. One of the distinctive features of material WHIPOX™ (section 2.4), the inhomogeneity of the investigated plates was examined first through NDT-tests. Only the results from “normal areas” were used in the modeling approach for the computation of the mechanical behavior of WHIPOX™.

The material properties under tensile load were measured in WHIPOX™ with different winding angles at room temperature. In contrast to the tensile test, because of the interlaminar failure and the buckling effect of compression samples, the strain gauges could not measure the strain values correctly until failure (see section 6.1), the compression fracture strain was not recorded in this study. Furthermore, due to the relatively low compressive strength, the Iosipescu-shear specimens fail locally in the testing rig where high compressive stresses prevailed. Therefore, the necessary stress-strain curve for the determination of the shear module only relates to the initial linear region (see section 6.1). Therefore, calculation of failure strain, modeling of stress-strain behavior and analysis of failure mode have been concentrated on the mechanical properties of WHIPOX™ under tensile load in this work.

As the interaction term F_{12} from the Tsai-Wu equation in stress space has been set to zero in section 5.3.1, this assumption is discussed in this section. The original formulation of the Tsai-Wu failure criterion includes the interaction term $2F_{12}\sigma_1\sigma_2$, which cannot be evaluated directly using the five strength values σ_1^T, σ_2^T, σ_1^C, σ_2^C and τ_{12} in Table 7.5. It has to be determined by a much more complicated bi-axial tensile test. An empirical model for the determination of the F_{12} value is taken from Hahn and Tsai in [116] and shown as equation 5.58 in section 5.3.1. This results in a value of F_{12} being -6.0E-05 for WHIPOX™ UD-WC and -3.5E-5 for UD-NC. According to the conclusion of Tsai-Wu failure criterion in [121], the interaction term F_{12} for WHIPOX™ may be considered as being zero since they fall in the range ±6.0E-05. Although these values are very small, the interaction term F_{12} has a significant effect on the shape of the Tsai-Wu failure surface for WHIPOX™. Figure 8.1 shows the 2D representation of Tsai-Wu stress failure criterion in Sigma1-Sigma2-plane with and without the F_{12} term. The black symbols are the tensile test results with the fiber orientations ±3° and ±87°. These were considered to be very close to the strength in the fiber direction (Sigma 1) and transverse direction of the UD-layer (Sigma 2), respectively.

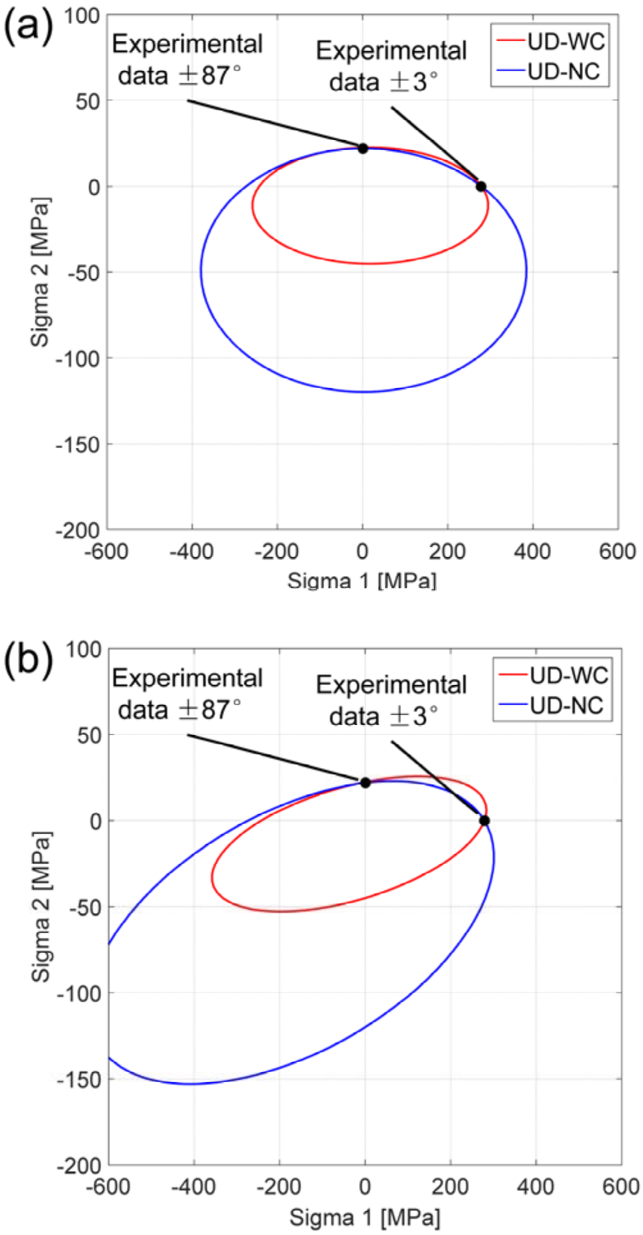

Figure 8.1: 2D representation of Tsai-Wu stress failure criterion in sigma1-sigma2-plane: a) without the interaction term F_{12} and b) with the interaction term F_{12}.

The large difference between these failure surfaces (Figure 8.1) is only due to the value of the interaction term F_{12}. In Figure 8.1b the strength in the bi-axial compression quadrant will be overestimated. The values of F_{12} for WHIPOX^{TM} with matrix cracks (UD-WC) and without matrix cracks (UD-NC) that are calculated for a bi-axial failure stress σ_{bi} between 10 to 100 MPa are shown in Figure 8.2. The curves of both equivalent UD-layers are similar. As can be seen from Figure 8.2, the variation of the interaction term F_{12} is relatively large and it becomes negative for a bi-axial failure stress of approx. 20 MPa. Based on the good correlation between the modeling results and experiments, in the case of material WHIPOX™, it turns out that assigning a zero value to F_{12} was a good choice, since the bi-axial failure stress of a real UD-layer has not been experimentally determined.

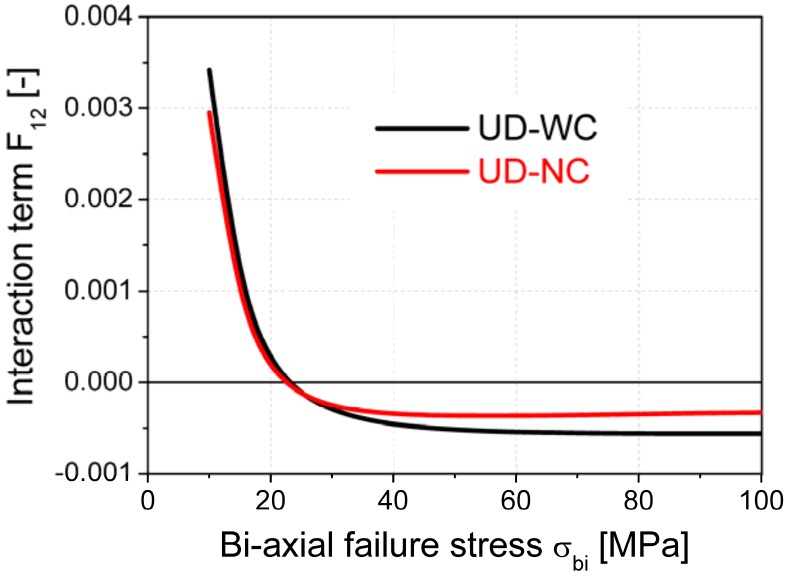

Figure 8.2: Dependence of the interaction term F_{12} on the bi-axial failure stress σ_{bi}.

8.2 Modeling with the equivalent UD-layer

In order to model the mechanical properties of WHIPOX™ a virtual equivalent UD-layer is introduced. Based on the analysis of microstructure for shrinkage cracks in section 4.2, modeling with the equivalent UD-layer properties was divided into two classes: WHIPOX™ with matrix cracks (WC) and WHIPOX™ without matrix cracks (NC). A transition line between the matrix with and without matrix cracks can be found in the winding angle of ±30°. No cracks were observed for smaller winding angles and WHIPOX™ with a winding angle of ±30° until ±45 showed similar crack distributions. Two UD-material parameter sets of the calculated elastic constants (Table 7.3), the estimated strength values (Table 7.5), the Tsai-Wu parameters in stress space (Table 7.6) and the inelastic deformation factor Δ (section 7.3) are summarized in Table 8.1.

Table 8.1: Summary of the calculated elastic constants, the estimated strength values, the Tsai-Wu parameters in stress space and the inelastic deformation factor Δ for WHIPOX™ UD-WC and UD-NC material parameter sets.

UD-WC

Elastic constants	E_1^T [GPa]	E_2^T [GPa]	ν_{12} [-]	G_{12} [GPa]	E_1^C [GPa]	E_2^T [GPa]
	211.2	56.2	0.20	40.0	202.4	79.7

Strength values	σ_1^T [MPa]	σ_2^T [MPa]	σ_1^C [MPa]	σ_2^C [MPa]	τ_{12} [MPa]
	279.0	22.5	-243.0	-45.0	65.0

Tsai-Wu parameters	F_1	F_{11}	F_2	F_{22}	F_{66}
	-5.3E-04	1.5E-05	2.2E-02	9.9E-04	2.4E-04

Δ	$\Delta = (-6.6E-3)\theta + 1.0$

UD-NC

Elastic constants	E_1^T [GPa]	E_2^T [GPa]	ν_{12} [-]	G_{12} [GPa]	E_1^C [GPa]	E_2^T [GPa]
	211.2	107.8	0.20	40.0	202.4	124.0

Strength values	σ_1^T [MPa]	σ_2^T [MPa]	σ_1^C [MPa]	σ_2^C [MPa]	τ_{12} [MPa]
	279.0	22.0	-274.0	-120.0	85.0

Tsai-Wu parameters	F_1	F_{11}	F_2	F_{22}	F_{66}
	-6.5E-05	1.3E-05	3.7E-02	3.8E-04	1.4E-04

Δ	$\Delta = 1.0$

By using the parameters for the equivalent UD-layers of UD-WC and UD-NC in Table 8.1, calculations of the elastic constants, the failure strength/strain values and the elastic/inelastic behaviors were performed through the modeling approaches in section 7 for wound WHIPOX™ composites with different fiber orientations. Furthermore, by using the modified directional failure indices (section 5.3.4) the failure mode can be predicted for WHIPOX™ under tensile load. The modeling approach to successive ply failures with inelastic properties taken into account has been used to predict the material behavior of WHIPOX™ laminate with different lay groups. Moreover, a manufacturing factor Ω (one of the distinctive features of material WHIPOX™ in section 2.4) was introduced which considered the FVC and porosity e' of the different batches. By applying of manufacturing factor Ω, a much better correlation between the measured and predicted results, especially concerning the elastic properties, could be obtained. A few deviations in the modeling of failure strength with factored in Ω (e.g. calculated compression strength by ±60° in Figure 7.10b) can be explained by the lack of further unidentified factors: due to the fact that the manufacturing factor Ω_k only takes into account FVC, porosity (e') and the angle between fiber orientation and occurring stress, more uncertainties and different microstructures created due to the manufacturing process, such as the distribution of the matrix or density of the micro delamination and so on, were not considered in the modeling of mechanical properties of wound CMCs.

With the modeling approaches explained in section 7 and the results summarized in section 7 and in Table 8.1, the failure tensile strain for the equivalent UD-layer with (WC) and without (NC) matrix cracks can be calculated. The results were shown in Figure 8.3a depending on the loading direction θ_k. As mentioned before, with the WHIPOX™ without matrix cracks, linear behavior with the inelastic deformation factor Δ equal to 1 is expected. In the case of a tensile test conducted in the fiber's direction on a UD-layer with matrix cracks, the properties of fiber are dominant and the matrix and shrinkage cracks have only a limited influence. The material behavior can be assumed to be linear elastic up to failure. In other words, the value of factor Δ should be equal to 1.0. This agrees with the calculated results from the second part of equation 7.1 (where $\theta = 0$). Therefore, the failure tensile strain from both NC and WC groups are identical and equal to approx. 0.13 % (in Figure 8.3a). On the other hand, with the loading in a transverse fiber direction, e.g. 90°, a significantly higher failure strain in group WC compared to the group NC can be seen in Figure 8.3. This is because of its non-linear behavior with the lowest Δ value.

Furthermore, tensile strength values of equivalent UD-layers (WC and NC) depending on the loading direction θ_k are calculated and plotted in Figure 8.3b. Because similar values under tensile loading between the two can be seen (the parameters of the Tsai-Wu failure stress criterion in Table 7.5), it follows that almost identical curves for UD-WC and UD-NC can be obtained, as Figure 8.3b.

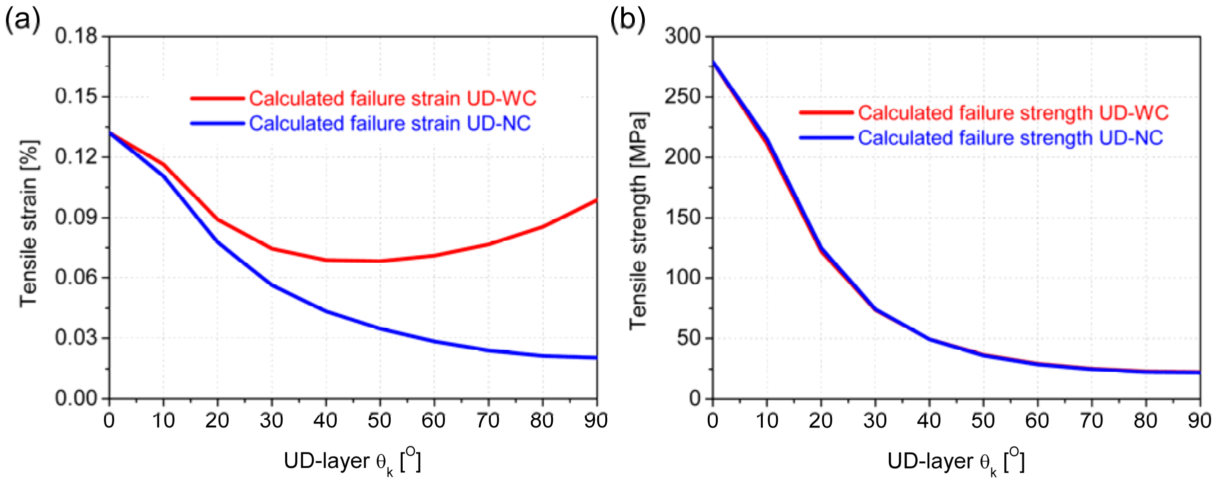

Figure 8.3: Calculated a) failure tensile strain and b) failure tensile stress for the equivalent UD-layer with (WC) and without (NC) matrix cracks depending on the loading direction θ_k.

Based on the above summarized properties of the equivalent UD-layers, these equivalent UD-layers are used to creat equivalent layered composite with any desired fiber orientation. Its material constants can be predicted by using the modeling approaches presented in this work.

In order to demonstrate the potential of the modeling approaches with equivalent UD-layers, material properties of laminates with orientation of 0°/90° are calculated. According to the results of analysis for shrinkage cracks (section 4.2) laminates with fiber orientation 0°/90° (winding angle ±45°) belong to the group with matrix cracks (WC). Therefore, the material behavior of laminate 0°/90° was calculated with equivalent UD-WC properties in section 7.3.2 and the multi-linear modeling results were shown a good correlation with the original test results in Figure 7.17a. In comparison, laminates with the orientation of 0°/90° from the group NC have not been experimentally determined since this winding angle ±45° cannot be manufactured without matrix cracks (see Figure 4.3a). However, the mechanical behavior of this virtual laminate can be still calculated through the modeling approaches given in this study with UD-NC properties. The modeling results for the laminate 0°/90° from different groups UD-WC (with matrix cracks) and UD-NC (without matrix cracks) are shown in Figure 8.4.

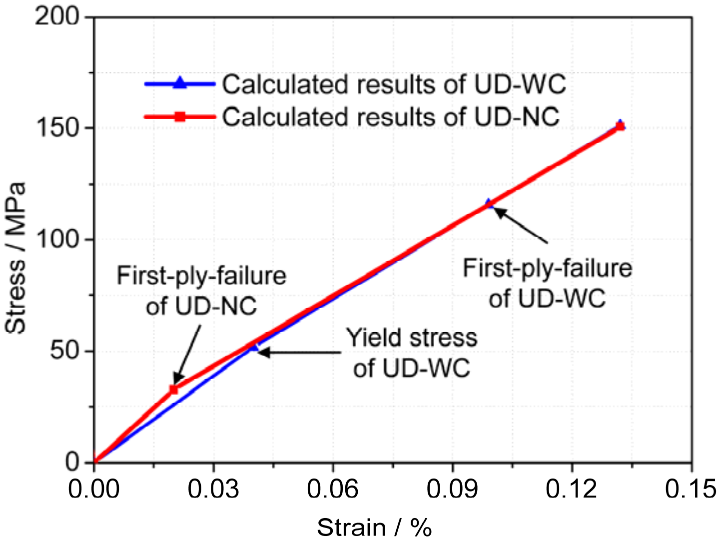

Figure 8.4: Calculated results of the laminate 0°/90° from groups with (UD-WC) and without (UD-NC) the matrix cracks.

As can be seen from Figure 8.4, the initial stiffness of laminate from NC (red curve) is higher than WC (blue curve), which is because the Young's moduli in transverse direction (E_2^T) of NC-group is almost twice as much as the value of WC-group (section 7.1.1), the stronger 90° layer from NC-group in the laminate leads to a higher value of initial stiffness. Then, layer from group NC under tensile loading was considered to be displaying a linear stress-strain behavior with inelastic deformation factor Δ equal to 1.0 up to failure (section 7.3). Therefore, a bilinear model with one virtual yield stress (first-ply-failure) was used to describe the behavior of laminate 0°/90° from group NC (the red curve in Figure 8.4). For comparison, a multi-linear model with consideration of the non-elastic behavior of layer 90° from group WC (the blue curve) is shown in Figure 8.4 for laminate 0°/90° from group WC: firstly, bilinear model with a virtual yield stress of UD-WC for the non-linear material behavior will proceed; secondly, the second yield point appears after reaching the highest strength ratio R of layer groups 90° (first-ply-failure of laminate from group WC); thirdly, the laminate fails completely when last-ply-failure (layer 0°) occurs. With the results summarized in Figure 8.3, the failure strain and strength values of layer 0° from both groups NC and WC are identical. Therefore, the strength and failure strain values of the two laminates in Figure 8.4 are calculated with the same value in the event of the last-ply-failure.

8.3 Applicability of modeling approaches to other CMCs

The modeling approaches developed and presented in this study can be applied to predict the mechanical properties of other CMCs.

In the work of Tushtev et al. 2008 published in [129], based on the test data with non-orthogonal fiber orientations ±20°/±70° under in-plane tensile and shear loading, the elastic properties of an equivalent UD-layer were calculated through the Inverse Laminate Theory and applied to predict the effects of various braiding angles. The mechanical experiments focused on the C/C braided composite CARBOTEX® produced by EADS Space Transportation GmbH, Munich, Germany. The predicted elastic constants were compared with experiment values for the orthogonal braided (0°/90°) C/C composite. A general correlation was seen, especially for shear modulus. However, higher values for Young's modulus and Poisson's ratio were predicted, which may be explained by "the different geometry of tow undulation for orthogonal and non-orthogonal composites" in [129]. According to the collected knowledge in this dissertation, the potential for more precise predictions of the elastic properties of C/C could be realized if the relationship between tow undulation and fiber orientation was considered as a factor. This relationship could be one of the distinctive features of the C/C material.

A similar modeling approach was applied to predict the elastic properties of wound C/C-SiC material (with T800 fiber) in the work of Breede et al. 2016 in [130]. The equivalent UD-properties were calculated through ILT with tensile test results and estimated shear modulus. A correlation can be observed between the experiment and computed results with the exception of Poisson`s ratio. Its value was significantly exaggerated and could be improved with the use of a potential material factor for the relationship between transverse contraction and winding angle. It should be noted that the different micro-structures of wound C/C-SiC material can be obtained by varying the winding angles, e.g. winding angles ±15° and ±45° in [131]. The concept of WHIPOX™ with matrix cracks (WC) and without matrix cracks (NC) can be further transferred to improve the prediction of elastic properties of wound C/C-SiC composites. Based on the tensile strengths in the dissertation of Breede ([132]) the approximated strength values of the equivalent UD-layer are enumerated in Table 8.2. Due to the lack of values concerning results of compressive testing in [132], the strength parameters F_1 to F_{66} of Tsai-Wu failure criterion in stress space are calculated using only the tensile strength of the equivalent UD-layer in Table 8.2 ($\sigma_1^T = \sigma_1^C$ and $\sigma_2^T = \sigma_2^C$). The shear strength (τ_{12}) is taken from an existing report [133]. Similar to material WHIPOX™, the interaction term F_{12} from the Tsai-Wu equation has been set to zero.

Table 8.2: Summary of the calculated elastic constants ([130]), the estimated strength values, the Tsai-Wu parameters in stress space and the inelastic deformation factor *Δ* for wound C/C-SiC material parameter sets.

<table>
<tr><td rowspan="2">Elastic Constants ([130])</td><td>E_1^T [GPa]</td><td colspan="3">E_2^T [GPa]</td><td colspan="3">ν_{12} [-]</td><td>G_{12} [GPa]</td></tr>
<tr><td>190.6</td><td colspan="3">17.6</td><td colspan="3">0.20</td><td>9.8</td></tr>
<tr><td rowspan="2">Strength values</td><td colspan="2">$\sigma_1^T = \sigma_1^C$
[MPa]</td><td colspan="4">$\sigma_2^T = \sigma_2^C$
[MPa]</td><td colspan="2">τ_{12}
[MPa]</td></tr>
<tr><td colspan="2">230.0</td><td colspan="4">35.0</td><td colspan="2">80.0</td></tr>
<tr><td rowspan="2">Tsai-Wu parameters</td><td>F_1</td><td colspan="2">F_{11}</td><td colspan="2">F_2</td><td colspan="2">F_{22}</td><td>F_{66}</td></tr>
<tr><td>0</td><td colspan="2">1.9E-05</td><td colspan="2">0</td><td colspan="2">8.2E-04</td><td>1.6E-04</td></tr>
<tr><td>Δ</td><td colspan="8">$\Delta = (-0.015)\theta + 1.255$: Orientation $\pm 30°$ to $\pm 60°$
$\Delta = 1$: Orientation 0° to $\pm 15°$ & $\pm 75°$ to 90°</td></tr>
</table>

By using the strength ratio R of the Tsai-Wu failure criterion, which has been presented for material WHIPOX™, the tensile strengths of the wound C/C-SiC with different fiber orientations can be predicted. Figure 8.5a shows the original test results (from [132]) with different fiber orientations and calculated failure strengths. The stress-strain response of wound C/C-SiC strongly depends on the loading direction. The composites under ±30°, ±45° and ±60° under tensile loading show non-linear elastic behavior and with ±15° and ±75° orientations the composites show an almost linear behavior in [132]. Therefore, similar to material WHIPOX™, an inelastic deformation factor *Δ* was evaluated for the fiber orientations between ±30° and ±60° (Table 8.3). A bar diagram for the comparison of calculated failure strain with the tensile test results for wound C/C-SiC with different fiber orientations is shown in Figure 8.5b. A strong correlation can be observed in Figure 8.5a and b for the measured and predicted failure values. It should be noted that, the equation of the factor $\Delta = (-0.015)\theta + 1.255$ in Table 8.2 was defined only for material C/C-SiC with winding angle from ±30° to ±60°.

A variety of different fiber orientations lead to different mechanical behaviors of wound C/C-SiC. This can be explained by the presence of different microstructure, which consequently influences the resulting material properties. On the one hand, similar microstructure of fiber orientations ±30° (±60°) and ±45° can be observed in [132]. On the other hand, due to the less hindering of shrinkage during the manufacturing process, the matrix width of winding angle ±15° (±75°) is clearly narrower (see [132]). Therefore, an identical definition of *Δ* from Table 8.2 cannot be applied for the fiber orientation between ±0° to ±30° and ±60° to ±90°. According to the stress-strain curves in [132], almost linear elastic behavior can be obtained for material C/C-SiC with winding angle 15° and 75°. Therefore, the failure strains of fiber orientation between ±0° to ±30° and ±60° to ±90° were calculated with $\Delta = 1$ (Table 8.2) and shown in Figure 8.5b. This phenomenon is comparable to the modeling approaches for material WHIPOX™ with two different groups WC with inelastic deformation and NC without inelastic deformation (section 5).

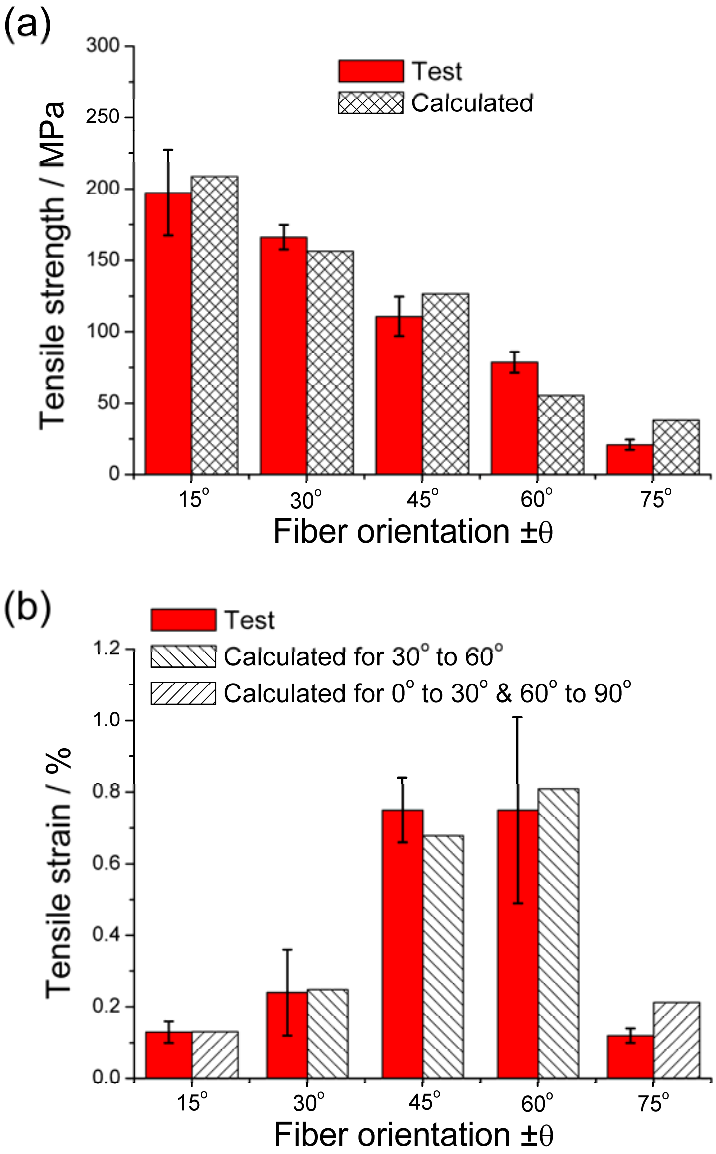

Figure 8.5: Comparison of calculated results to original experimental data of wound C/C-SiC, a) tensile strength and b) tensile strain.

The further applicability of these modeling approaches can be considered for the prediction of the mechanical properties of CMCs with woven structures, e.g. an oxide/oxide ceramic matrix composites “Keramikblech FW12” (acronym FW12) developed by Walter E.C. Pritzkow Spezialkeramik.

FW12 is composed of oxide fiber N610 and oxide matrix with 85 % Al_2O_3 and 15 % 3YSZ (3 mol % Yttria-stabilised Zirconia). The value of its porosity is approx. 25-35 %. The evaluated mechanical properties of FW12 under in-plane tensile and shear loading can be found in [134]. Due to the fact that the mechanical properties in the x- and y-directions are identical for woven composites, the values in Table 8.3 can be defined as the material constants for the equivalent UD-layer. These are then used for the calculation of properties in other loading directions. The Poisson's ratio in Table 8.3 is evaluated from the stress-strain curve of test results from [134] by using the software Engauge Digitizer 5.1.

Table 8.3: Elastic constants obtained from in-plane tensile and Iosipescu-shear tests for the material FW12 with the fiber orientation of 0°/90° from [134].

<table>
<tr><td rowspan="2">Elastic constants</td><td>$E_x = E_y$ [GPa]</td><td colspan="2">ν_{xy} [-]</td><td>G_{xy} [GPa]</td></tr>
<tr><td>122.8±2.9</td><td colspan="2">0.07</td><td>36.6±0.7</td></tr>
<tr><td colspan="5"></td></tr>
<tr><td rowspan="2">Strength [MPa]</td><td colspan="2">$\sigma_x = \sigma_y$</td><td colspan="2">τ_{xy}</td></tr>
<tr><td colspan="2">191.9±11.5</td><td colspan="2">92.7±1.7</td></tr>
</table>

The elastic properties of the woven FW12 at ±45° are determined on the basis of the elastic constants of its equivalent UD-layer (Table 8.3) using the modeling approach explained in section 5.1. The results are then compared with the experimental values from [134] and listed in Table 8.4. The software Engauge Digitizer 5.1 was used for the evaluation of Poisson's ratio for the test results at ±45°. The shear properties at ±45° were not investigated in [134]. A good correlation is seen in the measured and predicted values.

Table 8.4: Comparison of the calculated elastic constants with the experiment values (from [134]) for FW12 in test direction ±45°.

	$E_x = E_y$ [GPa]	ν_{xy} [-]	G_{xy} [GPa]
Experimental	98.9±4.0	0.26	-
Calculated	94.0	0.28	57.7

Furthermore, using the elastic constants of the equivalent UD-layer in Table 8.3, calculations are performed for different loading directions of the woven FW12 and plotted in Figure 8.6. These results can be used to design better methods to stack of woven fiber composites in a loading optimized fiber arrangement.

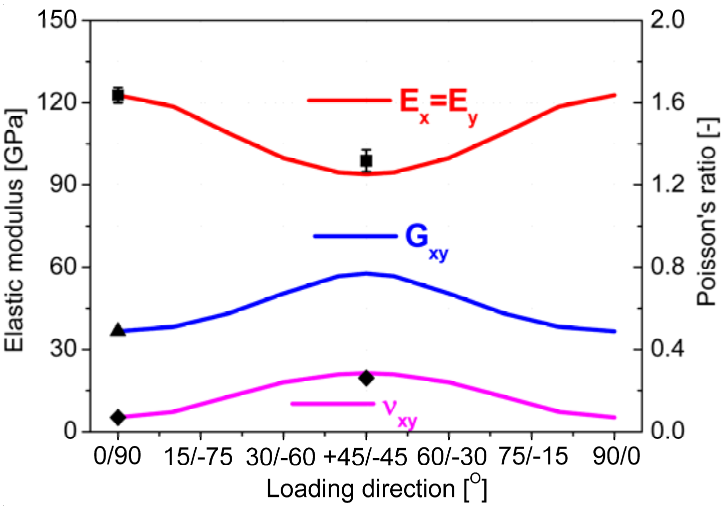

Figure 8.6: Experimental data (black symbols) and the predicted elastic properties of woven FW12 depending on the loading direction.

The Tsai-Wu failure criterion, described in section 5.3, is applied to predict the failure strength of the material FW12. Due to the lack of values concerning compressive strength in longitudinal and transverse directions in [134], the strength parameters F_1 to F_{66} are calculated using only the tensile strength of the equivalent UD-layer in Table 8.3. The failure tensile strength of FW12 in ±45° is determined through the Tsai-Wu criterion in stress space. The results are compared with the experimental values from [134] and listed in Table 8.5. The predicted result is slightly higher, which may be explained by the missing value under the compression load. The load capacity under tensile or compression stress can be different for CMCs, for example with the material WHIPOX™ in 0°/90° (Table 6.2): the tensile strength is 134.3 MPa and the compression strength is -193.6 MPa. The value of compression is approx. 45 % higher than the absolute tensile value. Thus, if a higher value, e.g. -275 MPa (approx. 45 % higher than the tensile value) is assumed as the compressive strength for FW12 in the 0°/90° direction, the calculated strength for ±45° is 141.9 MPa. This is much closer to the original test results (Table 8.5). According to the stress-strain curves in [134], clear inelastic behavior can be obtained with material FW12. However, without further results concerning the values of failure strain and stress-strain curves in other loading directions, the modeling of non-linear behavior and failure strain for FW12 under varying stress directions is not possible.

Table 8.5: Comparison of the calculated failure strength with the experimental values (from [134]) for FW12 in testing direction ±45°.

	$\sigma_x = \sigma_y$ [MPa]
Experimental	133.1±4.3
Calculated	153.1
Calculated with modified compression strength	141.9

Finally, the material properties of two more oxide/oxide CMCs with woven structures, COI 720/AS (COI Ceramics, USA) and GEN-IV (General Electric, USA) have been calculated and compared with the experiment results. The modeling approaches are the same as with FW12, the test values in 0°/90° can be defined as the material constants for the equivalent UD-layer. These are then used for the calculation of the properties in other loading directions. The test results can be found in [35]. Due to the lack of further test data, only the calculated elastic modul of COI 720/AS and the tensile strength of GEN-IV have been compared to the original results in test direction ±45°. A good correlation between experiment and analytically calculated results can be seen in Table 8.6.

Table 8.6: Comparison of calculated material properties with experiment values from [35] for oxide/oxide CMCs COI 720/AS and GEN-IV in the testing direction ±45°.

<table>
<tr><td colspan="2">COI 720/AS</td></tr>
<tr><td>Elastic module</td><td>$E_x = E_y$ [GPa]</td></tr>
<tr><td>Experimental</td><td>50.0</td></tr>
<tr><td>Calculated</td><td>49.0</td></tr>
<tr><td colspan="2">GEN-IV</td></tr>
<tr><td>Tensile strength</td><td>$\sigma_x = \sigma_y$ [MPa]</td></tr>
<tr><td>Experimental</td><td>54.0</td></tr>
<tr><td>Calculated</td><td>53.1</td></tr>
</table>

9 Summary and conclusions

The present work has demonstrated that the mechanical behavior of wound ceramic composites with various fiber orientations may be described using macroscopic constitutive modeling approaches.

First, all modeling approaches developed in this study are dependent on experimental determination and microstructure analysis. The mechanical properties of the investigated material WHIPOX™ in different wound orientations (±3°/±87°, ±15°/±75°, ±22.5°/±67.5°, ±30°/±60° ±45°, 0°/90° and 0°/60°) were completely evaluated with in-plane tension, Iosipescu-shear and compression tests at room temperature. The material's characteristic values, including initial stiffness, strength, strain, elastic and inelastic behavior were used for the modeling of the mechanical properties of the material WHIPOX™ with any desired fiber orientation. Based on the microstructure analysis of shrinkage cracks of WHIPOX™ through Micro Computed Tomography, a transition line between the matrix with and without cracks can be found in the winding angle of ±30°. No cracks were observed for smaller winding angles and WHIPOX™ with the winding angles of ±30° until ±45 showed similar crack distributions. Therefore, the modeling of the properties of WHIPOX™ was divided into two classes: WHIPOX™ with matrix cracks (WC) and WHIPOX™ without matrix cracks (NC).

Then, it was demonstrated that traditional modeling methods and classic failure criterion, which were introduced to predict the mechanical properties of fiber reinforced polymers, cannot be directly adapted to describe the material behavior of wound CMCs. This is due to the lack of the required matrix and fiber properties within the composite and due to the unavailable representative characteristics of CMC UD-materials. Therefore, advanced modeling approaches with virtually equivalent UD-layer properties are created for the evaluation and prediction of the material properties of wound CMC materials. These approaches are summarized in a flow diagram Figure 5.7 “chain from testing to modeling” (section 5.6). As the core component of the modeling chain, complete material properties of equivalent UD-layers were calculated and evaluated: elastic properties through the Inverse Laminate Theory; strength properties by fitting different test results to modified Tsai-Wu criterion; and failure strain using the inelastic deformation behavior factor Δ. All the values are discussed and calculated with consideration given to different microstructures with or without matrix cracks. Through the stacking of these equivalent UD-layers with any desired fiber orientation, e.g. non-orthogonal, orthogonal and asymmetrical (off-axis), an equivalent layered composite is created and its material constants can be predicted.

Furthermore, the modeling approaches developed in this study may be applied to different fiber reinforced composites manufactured by the winding process. However, particular features of investigated material have to be taken into consideration in order to predict mechanical properties with more accuracy. For the investigated composite WHIPOX™, four material specialties are implemented in the modeling approaches:

- Identification of inhomogeneity in the investigated plate through Non Destructive Inspection: the modeling approaches for computation of mechanical behavior are applied only based on experimental results from areas without significant defects.

- Interaction between failure strength and strain through inelastic deformation: the inelastic deformation factor Δ was defined as a relationship between failure strength and maximal strain, and used to describe the inelastic behavior of the investigated material WHIPOX™.
- Division of material modeling groups based on the analysis of microstructure: the evaluated mechanical properties of the equivalent UD-layer were divided into two classes: the first being for WHIPOX™ with matrix cracks (WC) and the second as WHIPOX™ without matrix cracks (NC). These were based on the CT-results.
- Update of the analytical model for different batches with inhomogeneities created due to the manufacturing process: with consideration given to different fiber volume contents, porosities and the angles between fiber orientation and occurring stress, a manufacturing factor Ω for different batches was evaluated through a modified mixing rule. This can be used to qualify uncertainties in the laminate during the manufacturing process.

Finally, modeling approaches for the prediction of the material properties of wound ceramic composites were presented. It was shown that the Classical Laminate Theory (CLT) and the Inverse Laminate Theory (ILT) can be used to calculate the elastic properties of WHIPOX™ with different microstructures. Using the strength ratio R of the Tsai-Wu failure criterion the strength values of the laminate with different fiber orientations can be predicted. The modeling approach using the modified definition of the directional failure indices $\sum_{ij}$ has been used to predict the failure mode of WHIPOX™. A modified stiffness matrix with the inelastic deformation factor Δ leads to a precise calculation of failure strain and has been used to describe the inelastic stress-strain behavior. The material behavior of asymmetric lay groups (off-axis) was determined through successive ply failure approach. Based on the good correlation between the experiments and the modeling results, it can be shown that modeling approaches factoring in the above mentioned particular material features allow for a very accurate prediction of the in-plane mechanical properties for CMC laminates.

In future work, investigations should be conducted to see if the material behavior can be modeled for other CMC materials in the same way as presented here. As discussed in section 8.3, the presented approaches are useful for some other WMC materials with braided, wound and woven structures. For WICs with fiber coating, e.g. SiC/SiC material, the influence of the interphase area between fiber and matrix on the mechanical properties of different fiber orientations might be evaluated and defined as a material distinctive feature.

Furthermore, in order to develop and assess modeling approaches for the prediction of mechanical behavior, different experiment determinations for material characterization should be performed in order to to validate the models. However, as CMCs are mostly emerging materials under active development, property characterization is limited. It is not unusual to encounter significant variations in important properties resulting from small refinements in processing. On the other hand, a feature of most current experimental investigations is the dependence on uniaxial simple test procedure, which identifies only one or two material parameters per test sample. Bi- or multi-axial testing methods have to be developed to overcome these issues and to allow for the determination of various material parameters from multiaxial responses of the specimen.

Additionally, further development of modeling approaches should be given priority in the future. The models have to be extended to predict the behavior of composites including the effects of out-of-plane force, high temperature, cyclic loading and damage. At the level of structural detail, modeling may take into account the size of holes, stiffening, transitions and other structural elements. In order to adapt the presented approaches for the computation of CMC structures, complete modeling methods should be implemented into Finite-Element-Method (FEM) code. Due to the fact that the modeling chain presented in this work was created with consideration of material particular features, a user subroutine may be incorporated with the inhomogeneity, the inelastic deformation, the division of modeling groups and the manufacturing factor of the investigated material.

Up to now, the present work has identified a general modus operandi going from experimental determination and microstructure analysis to the prediction of the mechanical behavior of WHIPOX™ with varied fiber orientations. With these advanced modeling approaches, a comprehensive model could be established which considers fiber orientation via ILT and modified Tsai-Wu criterion on the one hand and complex and varying microstructures and material scatting via CT for microstructural analysis on the other. In the future, the same approaches will help to design and develop CMC structures to meet stiffness, strength and failure strain requirements. In this way the application of CMC-components in new fields, like aerospace and civil engineering, may be enhanced.

10 Literature

[1] F. Christin, "CMC Materials for Space and Aeronautical Applications," in *Ceramic Matrix Composites*, ed: Wiley-VCH Verlag GmbH & Co. KGaA, 2008, pp. 327-351.

[2] A. Kohyama, "CMC for Nuclear Applications," in *Ceramic Matrix Composites*, ed: Wiley-VCH Verlag GmbH & Co. KGaA, 2008, pp. 353-384.

[3] M. Gerendás, Y. Cadoret, C. Wilhelmi, T. Machry, R. Knoche, T. Behrendt*, et al.*, "Improvement of Oxide/Oxide CMC and Development of Combustor and Turbine Components in the HiPOC Program," *ASME 2011 Turbo Expo: Turbine Technical Conference and Exposition,* pp. 477-490, 2011.

[4] T. Behrendt, S. Hackemann, P. Mechnich, Y. Shi, S. Hönig, S. Hofmann*, et al.*, "Development and test of oxide/oxide cmc combustor liner demonstrators for aero engines," *ASME 2016 Turbo Expo: Turbine Technical Conference and Exposition,* 2016.

[5] T. P. Herbell and A. J. Eckel, "Ceramic Matrix Composites for Rocket Engine Turbine Applications," *Journal of Engineering for Gas Turbines and Power-Transactions of the Asme,* vol. 115, pp. 64-69, Jan 1993.

[6] S. Schmidt, S. Beyer, H. Knabe, H. Immich, R. Meistring, and A. Gessler, "Advanced ceramic matrix composite materials for current and future propulsion technology applications," *Acta Astronautica,* vol. 55, pp. 409-420, Aug-Nov 2004.

[7] I.-M. Low, *Ceramic matrix composites : microstructure, properties and applications*. Cambridge, England: Woodhead Pub. and Maney Pub. on behalf of the Institute of Materials, Minerals & Mining, 2006.

[8] J. Göring, S. Hackemann, and B. Kanka, "WHIPOX (R): A fiber-reinforced oxide-ceramic matrix composite for long-term high-temperature applications," *Materialwissenschaft Und Werkstofftechnik,* vol. 38, pp. 766-772, Sep 2007.

[9] F. Breede, R. Jemmali, H. Voggenreiter, and D. Koch, "Design and Testing of a C/C-Sic Nozzle Extension Manufactured Via Filament Winding Technique and Liquid Silicon Infiltration," in *Design, Development, and Applications of Structural Ceramics, Composites, and Nanomaterials*, ed: John Wiley & Sons, Inc., 2014, pp. 1-14.

[10] W. Zhao, P. K. Liaw, and N. I. Yu, "Computation of the lamina stacking sequence effect on elastic moduli of a plain-weave Nicalon/SiC laminated composite with a [0/30/60] lay-up," *Journal of Nuclear Materials,* vol. 253, pp. 10-19, Mar 1998.

[11] Z. M. Huang, "The mechanical properties of composites reinforced with woven and braided fabrics," *Composites Science and Technology,* vol. 60, pp. 479-498, 2000.

[12] J. Carey, M. Munro, and A. Fahim, "Longitudinal elastic modulus prediction of a 2-D braided fiber composite," *Journal of reinforced plastics and composites,* vol. 22, pp. 813-831, 2003.

[13] P. Potluri and A. Manan, "Mechanics of non-orthogonally interlaced textile composites," *Composites Part a-Applied Science and Manufacturing,* vol. 38, pp. 1216-1226, 2007.

[14] L. Srikanth and R. M. V. G. K. Rao, "Concurrent studies on braided and filament wound carbon fiber composites - a comparative appraisal," *Journal of reinforced plastics and composites,* vol. 30, pp. 1359-1365, Aug 2011.

[15] L. Xu, S. J. Kim, C. H. Ong, and S. K. Ha, "Prediction of material properties of biaxial and triaxial braided textile composites," *Journal of Composite Materials,* vol. 46, pp. 2255-2270, Aug 2012.

[16] S. W. Tsai and E. M. Wu, "A General Theory of Strength for Anisotropic Materials," *Journal of Composite Materials,* vol. 5, pp. 58-80, 1971.

[17] A. Puck and H. Schürmann, "Failure analysis of FRP laminates by means of physically based phenomenological models," *Composites Science and Technology,* vol. 62, pp. 1633-1662, 2002.

[18] W. Van Paepegem and J. Degrieck, "Calculation of damage-dependent directional failure indices from the Tsai–Wu static failure criterion," *Composites Science and Technology,* vol. 63, pp. 305-310, 2003.

[19] K. Tushtev, J. Horvath, D. Koch, and G. Grathwohl, "Deformation and failure modeling of fiber reinforced ceramics with porous matrix," *Advanced Engineering Materials,* vol. 6, pp. 664-669, Aug 2004.

[20] J. Lamon, "A micromechanics-based approach to the mechanical behavior of brittle-matrix composites," *Composites Science and Technology,* vol. 61, pp. 2259-2272, 2001.

[21] J. Lamon, "Approach to Microstructure–Behavior Relationships for Ceramic Matrix Composites Reinforced by Continuous Fibers," in *Ceramic Matrix Composites*, N. P. Bansal and J. Lamon, Eds., ed: John Wiley & Sons, Inc., 2014, pp. 520-547.

[22] K.-D. Linsmeier, "Technical Ceramics - The material of choice for the most demanding applications," *Verlag moderne industrie,* 2015.

[23] M. Schmücker and P. Mechnich, "All-Oxide Ceramic Matrix Composites with Porous Matrices," in *Ceramic Matrix Composites*, W. Krenkel, Ed., ed: Wiley-VCH Verlag GmbH & Co. KGaA, 2008, pp. 205-229.

[24] A. G. Evans, F. W. Zok, and T. J. Mackin, "The structural performance of ceramic matrix composites," in *High Temperature Mechanical Behaviour of Ceramic Composites*, S. V. Nair and J. Karl, Eds., ed Boston, USA: Butterworth-Heinemann, 1995, pp. 3-84.

[25] M. Y. He and J. W. Hutchinson, "Kinking of a Crack Out of an Interface," *Journal of Applied Mechanics-Transactions of the Asme,* vol. 56, pp. 270-278, Jun 1989.

[26] W.-C. Tu, F. F. Lange, and A. G. Evans, "Concept for a Damage-Tolerant Ceramic Composite with "Strong" Interfaces," *Journal of the American Ceramic Society,* vol. 79, pp. 417-424, 1996.

[27] K. Sindermann, "Langzeitverhalten eines SiC/Al2O3 Faserverbundwerkstoffs," Dissertation, Universität Karlsruhe, Karlsruhe, Germany, 1999.

[28] A. S. Fareed, "Chapter 12 - Silicon carbide and oxide fiber reinforced alumina matrix composites fabricated via directed metal oxidation," in *Handbook of Ceramic Composites*, N. P. Bansal, Ed., ed: Springer US, 2005, pp. 277-306.

[29] M. P. Bacos, "Carbon-Carbon Composites - Oxidation Behavior and Coatings Protection," *Journal de Physique IV,* vol. 3, pp. 1895-1903, Nov 1993.

[30] D. Taylor, "The structural behavior of tetrahedral framework compounds–a review. part I. Structural behavior," *Mineralogical Magazine,* vol. 47, pp. 319-326, 1983.

[31] D. Taylor, "The structural behavior of tetrahedral framework compounds-a review. Part II. Framework structures," *Mineralogical Magazine,* vol. 48, pp. 65-79, 1984.

[32] D. Lewis, "Future Opportunities and Critical Needs for Advanced Ceramics and Ceramic Matrix Composites in Aerospace Applications," in *24th Annual Conference on Composites, Advanced Ceramics, Materials, and Structures: A: Ceramic Engineering and Science Proceedings,* . vol. 21, T. Jessen and E. Ustundag, Eds., ed Hoboken, NJ, USA John Wiley & Sons, Inc., 2000, pp. 2-14.

[33] K. A. Keller, G. Jefferson, and R. J. Kerans, "Chapter 16 - Oxide-Oxide Composites," in *Handbook of Ceramic Composites*, N. P. Bansal, Ed., ed: Springer US, 2005, pp. 377-421.

[34] W. Pritzkow, A. Nöth, and A. Rüdinger, "Oxide Ceramic Matrix Composites - Manufacturing, Machining, Properties and Industrial Applications," *Ceramic Applications,* vol. 3, pp. 48-54, 2015.

[35] K. A. Keller, G. Jefferson, and R. J. Kerans, "Oxide-Oxide Composites," in *Ceramic Matrix Composites*, N. P. Bansal and J. Lamon, Eds., ed: John Wiley & Sons 2014, pp. 236-272.

[36] P. Spriet, "CMC Applications to Gas Turbines," in *Ceramic Matrix Composites*, N. P. Bansal and J. Lamon, Eds., ed: John Wiley & Sons, Inc., 2014, pp. 591-608.

[37] A. R. Bunsell and M. H. Berger, "Fine diameter ceramic fibres," *Journal of the European Ceramic Society,* vol. 20, pp. 2249-2260, 2000.

[38] D. Schawaller, B. Clauss, and M. R. Buchmeiser, "Ceramic Filament Fibers - A Review," *Macromolecular Materials and Engineering,* vol. 297, pp. 502-522, Jun 2012.

[39] M. Schmücker and P. Mechnich, "Microstructural Coarsening of Nextel™610 Fibers Embedded in Alumina-Based Matrices," *Journal of the American Ceramic Society,* vol. 91, pp. 1306-1308, 2008.

[40] F. Deléglise, M. H. Berger, and A. R. Bunsell, "Microstructural evolution under load and high temperature deformation mechanisms of a mullite/alumina fibre," *Journal of the European Ceramic Society,* vol. 22, pp. 1501-1512, 2002.

[41] 3M, "Nextel™ - Ceramic Textiles Technical Notebook," online product literature 2011.

[42] NITIVY Co. L. Datasheet of Nitivy ALF™ fiber [Online]. Available: http://www.nitivy.co.jp/en/products/alf/index.html

[43] S. Petzold, M. Morche, and J. Taesler, "Oxide-ceramic continuous fibres and ceramic fibre reinforced composites – innovative materials for the firing process," *Ziegelindustrie International,* pp. 24-31, 2011.

[44] M. Schmücker, F. Flucht, and P. Mechnich, "Degradation of oxide fibers by thermal overload and environmental effects," *Materials Science and Engineering: A,* vol. 557, pp. 10-16, 2012.

[45] A. G. Evans and F. W. Zok, "Review: The Physics and Mechanics of Fiber-Reinforced Brittle Matrix Composite," *Journal of materials and science,* vol. 29, pp. 3857-3896, 1994.

[46] F. W. Zok, "Developments in Oxide Fiber Composites," *Journal of the American Ceramic Society,* vol. 89, pp. 3309-3324, 2006.

[47] R. J. Kerans, R. S. Hay, T. A. Parthasarathy, and M. K. Cinibulk, "Interface design for oxidation-resistant ceramic composites," *Journal of the American Ceramic Society,* vol. 85, pp. 2599-2632, Nov 2002.

[48] G. Jefferson, K. A. Keller, R. S. Hay, and R. J. Kerans, "Oxide/Oxide Composites with Fiber Coatings," in *Ceramic Matrix Composites*, W. Krenkel, Ed., ed: Wiley-VCH Verlag GmbH & Co. KGaA, 2008, pp. 187-204.

[49] C. J. Griffin and R. R. Kieschke, "CVD Processing of Fiber Coatings for CMCs," in *Proceedings of the 19th Annual Conference on Composites, Advanced Ceramics, Materials, and Structures - A: Ceramic Engineering and Science Proceedings*. vol. 16, J. B. Wachtman Jr, Ed., ed Hoboken, NJ, USA: John Wiley & Sons, Inc., 1995, pp. 425-432.

[50] M. Schmücker, H. Schneider, K. K. Chawla, Z. R. Xu, and J.-S. Ha, "Thermal Degradation of Fiber Coatings in Mullite-Fiber-Reinforced Mullite Composites," *Journal of the American Ceramic Society,* vol. 80, pp. 2136-2140, 2005.

[51] E. Boakye, R. S. Hay, and M. D. Petry, "Continuous coating of oxide fiber tows using liquid precursors: Monazite coatings on Nextel 720 (TM)," *Journal of the American Ceramic Society,* vol. 82, pp. 2321-2331, Sep 1999.

[52] E. E. Boakye, R. S. Hay, P. Mogilevsky, and L. M. Douglas, "Monazite coatings on fibers: II, coating without strength degradation," *Journal of the American Ceramic Society,* vol. 84, pp. 2793-2801, Dec 2001.

[53] M. Holmquist, R. Lundberg, O. Sudre, A. G. Razzell, L. Molliex, J. Benoit*, et al.*, "Alumina/alumina composite with a porous zirconia interphase - Processing, properties and component testing," *Journal of the European Ceramic Society,* vol. 20, pp. 599-606, 2000.

[54] K. A. Keller, T. I. Mah, T. A. Parthasarathy, and C. M. Cooke, "Fugitive interfacial carbon coatings for oxide/oxide composites," *Journal of the American Ceramic Society,* vol. 83, pp. 329-336, Feb 2000.

[55] J. B. Davis, D. B. Marshall, and P. E. D. Morgan, "Oxide composites of Al2O3 and LaPO4," *Journal of the European Ceramic Society,* vol. 19, pp. 2421-2426, 1999.

[56] P.-Y. LEE, M. IMAI, and T. YANO, "Effects of Sintering Condition on Mechanical Properties of Monazite-Coated Alumina-Fiber/Alumina-Matrix Composites Fabricated by Hot-Pressing," *Journal of the Ceramic Society of Japan,* vol. 112, pp. 29-34, 2004.

[57] H. T. Larker and R. Lundberg, "Near net shape production of monolithic and composite high temperature ceramics by hot isostatic pressing (HIP)," *Journal of the European Ceramic Society,* vol. 19, pp. 2367-2373, 1999.

[58] G. Motz, S. Schmidt, and S. Beyer, "The PIP-process: Precursor Properties and Applications," in *Ceramic Matrix Composites*, W. Krenkel, Ed., ed: Wiley-VCH Verlag GmbH & Co. KGaA, 2008, pp. 165-186.

[59] H. Fujita, C. G. Levi, F. W. Zok, and G. Jefferson, "Controlling mechanical properties of porous mullite/alumina mixtures via precursor-derived alumina," *Journal of the American Ceramic Society,* vol. 88, pp. 367-375, Feb 2005.

[60] P. Mogilevsky, R. J. Kerans, H. D. Lee, K. A. Keller, and T. A. Parthasarathyz, "On densification of porous materials using precursor solutions," *Journal of the American Ceramic Society,* vol. 90, pp. 3073-3084, Oct 2007.

[61] E. Volkmann, "Effects of High-temperature Exposure on the Mechanical Performance of Polymer-derived Oxide-based Ceramic Matrix Composites," PhD Thesis, Universität Bremen, Germany, 2015.

[62] S. Denis, M. Frieß, E. Klatt, and B. Heidenreich, "Manufacture and Characterization of OXIPOL Based on Different Oxide Fibres," presented at the 7th Int. Conf. on HT-CMC, 2010.

[63] A. Rüdinger and W. Pritzkow, "Die Entwicklung oxidkeramischer Faserverbundwerkstoffe am Fraunhofer ISC / Zentrum HTL in Zusammenarbeit mit W.E.C. Pritzkow Spezialkeramik," *Keramische Zeitschrift,* vol. 65, pp. 166-169, 2013.

[64] R. A. Simon, "Progress in processing and performance of porous-matrix oxide/oxide composites," *International Journal of Applied Ceramic Technology,* vol. 2, pp. 141-149, 2005.

[65] L. P. Zawada, R. S. Hay, S. S. Lee, and J. Staehler, "Characterization and high-temperature mechanical behavior of an oxide/oxide composite," *Journal of the American Ceramic Society,* vol. 86, pp. 981-990, Jun 2003.

[66] R. A. Jurf and S. C. Butner, "Advances in oxide-oxide CMC," *Journal of Engineering for Gas Turbines and Power-Transactions of the Asme,* vol. 122, pp. 202-205, Apr 2000.

[67] M. Schmücker and H. Schneider, "Chapter 17 - WHIPOX All Oxide Ceramic Matrix Composites," in *Handbook of Ceramic Composites*, N. P. Bansal, Ed., ed: Springer US, 2005, pp. 423-435.

[68] C. G. Levi, J. Y. Yang, B. J. Dalgleish, F. W. Zok, and A. G. Evans, "Processing and performance of an all-oxide ceramic composite," *Journal of the American Ceramic Society,* vol. 81, pp. 2077-2086, Aug 1998.

[69] B. Kanka, "Patent EP 1734023 B1 - Einstellung des Faservolumengehaltes in oxidkeramischen Faser-Verbundwerkstoffen ", 2006.

[70] D. Koch, K. Tushtev, and G. Grathwohl, "Ceramic fiber composites: Experimental analysis and modeling of mechanical properties," *Composites Science and Technology,* vol. 68, pp. 1165-1172, Apr 2008.

[71] A. G. Evans, M. Y. He, and J. W. Hutchinson, "Interface Debonding and Fiber Cracking in Brittle Matrix Composites," *Journal of the American Ceramic Society,* vol. 72, pp. 2300-2303, Dec 1989.

[72] T. Furukawa and G. Yagawa, "Implicit constitutive modelling for viscoplasticity using neural networks," *International journal for Numerical Methods in Engineering,* vol. 43, pp. 195-219, Sep 30 1998.

[73] R. Haj-Ali and H. K. Kim, "Nonlinear constitutive models for FRP composites using artificial neural networks," *Mechanics of Materials,* vol. 39, pp. 1035-1042, Dec 2007.

[74] R. Piat and E. Schnack, "Hierarchical material modeling of carbon/carbon composites," *Carbon,* vol. 41, pp. 2121-2129, 2003.

[75] J. D. Eshelby, "The Determination of the Elastic Field of an Ellipsoidal Inclusion, and Related Problems," *Proceedings of the Royal Society of London. Series A, Mathematical and Physical Sciences,* vol. 241, pp. 376-396, 1957.

[76] R. Hill, "Elastic properties of reinforced solids: Some theoretical principles," *Journal of the Mechanics and Physics of Solids,* vol. 11, pp. 357-372, 1963.

[77] T. Mori and K. Tanaka, "Average Stress in Matrix and Average Elastic Energy of Materials with Misfitting Inclusions," *Acta Metallurgica,* vol. 21, pp. 571-574, 1973.

[78] R. Hill, "Theory of mechanical properties of fibre-strengthened materials—III. self-consistent model," *Journal of the Mechanics and Physics of Solids,* vol. 13, pp. 189-198, 1965.

[79] T. Sabiston, M. Mohammadi, M. Cherkaoui, J. Levesque, and K. Inal, "Micromechanics for a long fibre reinforced composite model with a functionally graded interphase," *Composites Part B-Engineering,* vol. 84, pp. 188-199, Jan 2016.

[80] H. Ismar and F. Streicher, "Modelling and simulation of the mechanical behavior of ceramic matrix composites as shown by the example of SiC/SiC," *Computational Materials Science,* vol. 16, pp. 17-24, Dec 1999.

[81] C. Fagiano, M. Genet, E. Baranger, and P. Ladevèze, "Computational geometrical and mechanical modeling of woven ceramic composites at the mesoscale," *Composite Structures,* vol. 112, pp. 146-156, Jun 2014.

[82] W. Voigt, "Über die Beziehung zwischen den beiden Elastizitätskonstanten isotroper Körper," *Annalen der Physik,* vol. 38, pp. 573-587, 1889.

[83] J. C. H. Affdl and J. L. Kardos, "The Halpin-Tsai equations: A review," *Polymer Engineering and Science,* vol. 16, pp. 344-352, 1976.

[84] C. C. Chamis, "Mechanics of Composite-Materials - Past, Present, and Future," *Journal of Composites Technology & Research,* vol. 11, pp. 3-14, Spr 1989.

[85] Y. Shi, S. Hofmann, R. Jemmali, S. Hackemann, and D. Koch, "Ermittlung der elastischen Eigenschaften gewickelter oxidischer Faserverbundkeramiken," in *Tagungsband zum 19. Symposium Verbundwerkstoffe und Werkstoffverbunde*, A. Wanner, Ed., ed Karlsruhe, Germany: Deutsche Gesellschaft für Materialkunde 2013, pp. 205-211.

[86] Y. Shi, S. Hofmann, S. Hackemann, and D. Koch, "Evaluation and Validation of Elastic Properties and a Failure Criterion for an Oxide Wound Ceramic Composite Material," in *High Temperature Ceramic Matrix Composites 8*, L. Zhang and D. Jiang, Eds., ed: John Wiley & Sons, Inc., 2014, pp. 433-442.

[87] Y. Shi, S. Hofmann, R. Jemmali, S. Hackemann, and D. Koch, "Determination of Elastic Properties for a Wound Oxide Ceramic Composite," *Journal of Ceramic Science and Technology* vol. 5, pp. 31-38, 2013.

[88] Y. Shi, N. Jain, R. Jemmali, S. Hofmann, D. Koch, and S. Hackemann, "Prediction of Elastic Properties for a Wound Oxide Ceramic Matrix Composite Material," *International Journal of Applied Ceramic Technology,* vol. 12, pp. E99-E110, 2015.

[89] M. J. Hinton, A. S. Kaddour, and P. D. Soden, *Failure criteria in fibre reinforced polymer composites: The World-Wide Failure Exercise*. Oxford, UK: Elsevier Science Ltd., 2004.

[90] M. J. Hinton and A. S. Kaddour, "The background to the Second World-Wide Failure Exercise," *Journal of Composite Materials,* vol. 46, pp. 2283-2294, Sep 2012.

[91] A. S. Kaddour, M. J. Hinton, P. A. Smith, and S. Li, "The background to the third world-wide failure exercise," *Journal of Composite Materials,* vol. 47, pp. 2417-2426, Sep 2013.

[92] K. L. Reifsnider, G. P. Sendeckyj, S. S. Wang, W. S. Johnson, W. W. Stinchcomb, N. J. Pagano, *et al.*, "Survey of Failure and Post-Failure Theories of Laminated Fiber-Renforced Composites," *Journal of Composites Technology and Research,* vol. 8, p. 138, 1986.

[93] H. Thom, "A review of the biaxial strength of fibre-reinforced plastics," *Composites Part a-Applied Science and Manufacturing,* vol. 29, pp. 869-886, 1998.

[94] K. Rohwer, "Predicting fiber composite damage and failure," *Journal of Composite Materials,* vol. 49, pp. 2673-2683, Sep 2015.

[95] O. Mohr, "Welche Umstände bedingen die Elastizitätsgrenze und den Bruch eines Materials?," *Zeitschrift des Vereins deutscher Ingenieure,* vol. 24, pp. 1524-1530, 1572-1577, 1900.

[96] R. v. Mises, "Mechanik der festen Körper im plastisch - deformablen Zustand," *Nachrichten von der Gesellschaft der Wissenschaften zu Göttingen, Mathematisch-Physikalische Klasse,* vol. 1913, pp. 582-592, 1913.

[97] R. Hill, "A Theory of the Yielding and Plastic Flow of Anisotropic Metals," *Proceedings of the Royal Society of London A: Mathematical, Physical and Engineering Sciences,* vol. 193, pp. 281-297, 1948.

[98] I. I. Goldenblat and W. A. Kopnow, "Festigkeitsverhalten von Glasfaserlaminaten bei überlagerten Beanspruchungszustäden," *Mechanika Polimerow* vol. 2, pp. 70-78, 1965.

[99] O. Hoffman, "The Brittle Strength of Orthotropic Materials," *Journal of Composite Materials,* vol. 1, pp. 200-206, 1967.

[100] S. W. Tsai, "Strength Theories of Filamentary Structures," in *Fundamental Aspects of Fiber Reinforced Plastic Composites*, R. T. Schwartz and H. T. Schwartz, Eds., ed New York: Wiley Interscience, 1968, pp. 3-11.

[101] E. M. Wu and J. K. Scheublein, "Laminate Strength—A Direct Characterization Procedure," *Composite Materials: Testing and Design (3rd Conference), ASTM STP 546,* pp. 188-206, 1974.

[102] T. Becker, C. Dresbach, and S. Reh, "Adaption of a material model and development of a stochastic failure criterion for ceramic matrix composite structures," *Proceedings of the Institution of Mechanical Engineers, Part L: Journal of Materials: Design and Applications,* vol. 230, pp. 813-824, 2016.

[103] VDI, "Guideline VDI 2014 Part 3: Development of Fibre Reinforced Plastics Components, Analysis," *Aircraft Engineering and Aerospace Technology,* vol. 79, 2006.

[104] H. Dong, J. Wang, and B. L. Karihaloo, "An improved Puck's failure theory for fibre-reinforced composite laminates including the in situ strength effect," *Composites Science and Technology,* vol. 98, pp. 86-92, Jun 27 2014.

[105] R. G. Cuntze and A. Freund, "The predictive capability of failure mode concept-based strength criteria for multidirectional laminates," *Composites Science and Technology,* vol. 64, pp. 343-377, 2004.

[106] A. Puck, J. Kopp, and M. Knops, "Guidelines for the determination of the parameters in Puck's action plane strength criterion," *Composites Science and Technology,* vol. 62, pp. 371-378, 2002.

[107] T. Behnisch and M. Gude, "Schädigungsphänomenologie vonTextilverbundkeramiken unter Druckbeanspruchung in Verbunddickenrichtung," in *Arbeitskreis Verstärkung Keramischer Werkstoffe*, Stuttgart, Germany, 2016.

[108] R. Stößel, "Air-Coupled Ultrasound Inspection as a New Non-Destructuctive Testing Tool for Quality Assurance," Doctoral Thesis, University of Stuttgart, Stuttgart, Germany, 2004.

[109] T. Ullmann, Y. Shi, and R. Aoki, "Capabilities of Lock-in Thermography for Non-destructive Inspection of Fibre Reinforced Composites," in *11th International Conference on Quantitative InfraRed Thermography*, G. Gardone, Ed., ed. Naples, Italy, 2012.

[110] "DIN EN 1389: Advanced technical ceramics - Ceramic composites - Physical properties - Determination of density and apparent porosity," 2004.

[111] S. Hackemann, T. Behrendt, T. Aumeier, T. Richter, Y. Shi, S. Hofmann*, et al.*, "Development and Testing of a Low NOx Oxide Ceramic Combustor for Aero-Engines," in *39th International Conference and Expo on Advanced Ceramics and Composites*, Daytona Beach, USA, 2015.

[112] B. J. Kanka, M. Schmücker, W. Luxem, and H. Schneider, "Processing and Microstructure of WHIPOX™," in *High Temperature Ceramic Matrix Composites*, W. Krenkel, R. Naslain, and H. Schneider, Eds., ed Munich, Germany: Wiley-VCH, Weinheim, Cambridge, 2001, pp. 610-615.

[113] M. Schmücker, A. Grafmüller, and H. Schneider, "Mesostructure of WHIPOX all oxide CMCs," *Composites Part A: Applied Science and Manufacturing,* vol. 34, pp. 613-622, 2003.

[114] A. K. Kaw, *Mechanics of Composite Materials, Second Edition*: CRC Press, 2005.

[115] R. M. Jones, *Mechanics of Composite Materials, Second Edition*: Taylor & Francis Inc., 1998.

[116] S. W. Tsai and H. T. Hahn, *Introduction to Composite Materials*: Technomic Publishing Company, Inc., 1980.

[117] R. B. Pipes and B. W. Cole, "On the Off-Axis Strength Test for Anisotropic Materials," *Journal of Composite Materials,* vol. 7, pp. 246-256, 1973.

[118] K. S. Liu and S. W. Tsai, "A progressive quadratic failure criterion for a laminate," *Composites Science and Technology,* vol. 58, pp. 1023-1032, 1998.

[119] A. Kuraishi, S. W. Tsai, and K. K. S. Liu, "A progressive quadratic failure criterion, part B," *Composites Science and Technology,* vol. 62, pp. 1683-1695, 2002.

[120] S. W. Tsai and J. D. D. Melo, *Composite Materials Design and Testing*: Composites Design Group, 2015.

[121] E. M. Wu, "Optimal Experimental Measurements of Anisotropic Failure Tensors," *Journal of Composite Materials,* vol. 6, pp. 472-489, 1972.

[122] R. Narayanaswami and H. M. Adelman, "Evaluation of the Tensor Polynomial and Hoffman Strength Theories for Composite Materials," *Journal of Composite Materials,* vol. 11, pp. 366-377, 1977.

[123] W.-P. Lin and H.-T. Hu, "Parametric Study on the Failure of Fiber-Reinforced Composite Laminates under Biaxial Tensile Load," *Journal of Composite Materials,* vol. 38, pp. 1481-1503, 2002.

[124] M. R. Garnich and G. Karami, "Finite Element Micromechanics for Stiffness and Strength of Wavy Fiber Composites," *Journal of Composite Materials,* vol. 38, pp. 273-292, 2004.

[125] B. Ellul, D. Camilleri, and J. C. Betts, "A Progressive Failure Analysis Applied to Fiber-Reinforced Composite Plates Subject to Out-of-Plane Bending," *Mechanics of Composite Materials,* vol. 49, pp. 605-620, Jan 2014.

[126] S. W. Tsai, *Composites design - 1985 United States Air Force Materials Laboratory*. USA: Think Composites, 1985.

[127] W. Van Paepegem, "Development and finite element implementation of a damage model for fatigue of fibre-reinforced polymers," PhD Thesis, , Ghent University, Ghent, 2002.

[128] M. Gerendás, C. Wilhelmi, T. Machry, R. Knoche, E. Werth, T. Behrendt*, et al.*, "Development and Validation of Oxide/Oxide CMC Combustors Within the HiPOC Program," *ASME Turbo Expo 2013: Turbine Technical Conference and Exposition,* vol. 4, 2013.

[129] K. Tushtev, D. Koch, and G. Grathwohl, "Elastic properties of braided ceramic matrix composites," *International Journal of Materials Research,* vol. 99, pp. 1262-1267, Nov 2008.

[130] F. Breede, S. Hofmann, N. Jain, and R. Jemmali, "Design, Manufacture, and Characterization of a Carbon Fiber-Reinforced Silicon Carbide Nozzle Extension," *International Journal of Applied Ceramic Technology,* vol. 13, pp. 3-16, Jan-Feb 2016.

[131] S. Hofmann, F. Breede, N. Jain, and D. Koch, "Finite element analysis of a carbon fibre reinforced SiC nozzle under internal pressure load," in *90th DKG Annual Conference & Symposium on High-Performance Ceramics 2015*, Bayreuth, Germany, Mar. 16-18. 2015.

[132] F. Breede, "Entwicklung neuartiger faserkeramischer C/C-SiC Verbundwerkstoffe auf Basis der Wickeltechnik für Raketendüsen," Dissertation University Stuttgart, Stuttgart, Germany, 2017.

[133] S. Geinitz, "Ermittlung des Schubmoduls von Faserverstärkter Keramik," Studienarbeit, Institut für Flugzeugbau der Universität Stuttgart und Institut für Bauweisen- und Konstruktionsforschung des DLR, 2006.

[134] K. Tushtev. Charakterisierung von Keramikblech Typ FW12 [Online]. Available: http://www.keramikblech.com/fileadmin/user_upload/pdf/Bericht_Pritzkow_10_2012.pdf

Liste of publications

- **Peer reviewed publications**

Y. Shi, B. Heidenreich, P. K. Dileep, and D. Koch, "Characterization and simulation of bending properties of continuous fiber reinforced C/C-SiC sandwich structures," *Key Engineering Materials,* vol. 742, pp. 215-222, 2017.

Y. Li, P. Xiao, **Y. Shi**, R. S. M. Almeida, W. Zhou, Z. Li, H. Luo, F. Reichert, N. Langhof, and W. Krenkel, "Mechanical behavior of LSI based C/C-SiC composites subjected to flexural loadings," *Composites Part A: Applied Science and Manufacturing,* vol. 95, pp. 315-324, 2017.

Y. Shi, J. M. Hausherr, H. Hoffmann, and D. Koch, "Inspection of geometry influence and fiber orientation to characteristic value for short fiber reinforced ceramic matrix composite under bending load," *Journal of the European Ceramic Society,* vol. 37, pp. 1291-1303, 2017.

T. Behrendt, S. Hackemann, P. Mechnich, **Y. Shi**, S. Hönig, S. Hofmann, and D. Koch, "Development and Test of Oxide/Oxide Ceramic Matrix Composites Combustor Liner Demonstrators for Aero-engines," *Journal of Engineering for Gas Turbines and Power,* vol. 139, pp. 1-12, 2016.

Y. Shi, K. Tushtev, and D. Koch, "Characterization of Mechanical Properties under Shear Load of a Short-Carbon-Fiber-Reinforced C/SiC Ceramic," *Journal of Ceramic Science and Technology* vol. 6, pp. 183-190, 2015.

Y. Shi, D. Koch, J. M. Hausherr, and A. Neubrand, "Influence of Specimen Geometry and Surface Quality on the Bending Strength of Short Fiber-Reinforced C/SiC," *Materials Science Forum,* vol. 825-826, pp. 249-255, 2015.

Y. Shi, N. Jain, R. Jemmali, S. Hofmann, D. Koch, and S. Hackemann, "Prediction of Elastic Properties for a Wound Oxide Ceramic Matrix Composite Material," *International Journal of Applied Ceramic Technology,* vol. 12, pp. E99-E110, 2015.

Y. Shi, K. Tushtev, J.-M. Hausherr, D. Koch, and K. Rezwan, "Oxidation Kinetics and Its Impact on the Strength of Carbon Short Fiber Reinforced C/SiC Ceramics," *Advanced Engineering Materials,* vol. 15, pp. 19-26, 2013.

Y. Shi, S. Hofmann, R. Jemmali, S. Hackemann, and D. Koch, "Determination of Elastic Properties for a Wound Oxide Ceramic Composite," *Journal of Ceramic Science and Technology* vol. 5, pp. 31-38, 2013.

- **Publications in proceedings**

T. Behrendt, T. Aumeier, S. Hackemann, P. Mechnich, and **Y. Shi**, "Entwicklung und Test eines Brennkammerdemonstrators aus oxidischer Faserverbundkeramik für Flugtriebwerke," in *Deutscher Luft- und Raumfahrtkongress* ed. Rostock, Germany, 2015.

Y. Shi, S. Hofmann, S. Hackemann, and D. Koch, "Evaluation and Validation of Elastic Properties and a Failure Criterion for an Oxide Wound Ceramic Composite Material," in *High Temperature Ceramic Matrix Composites 8*, L. Zhang and D. Jiang, Eds., ed: John Wiley & Sons, Inc., 2014, pp. 433-442.

Y. Shi, S. Hofmann, R. Jemmali, S. Hackemann, and D. Koch, "Ermittlung der elastischen Eigenschaften gewickelter oxidischer Faserverbundkeramiken," in *Tagungsband zum 19. Symposium Verbundwerkstoffe und Werkstoffverbunde*, A. Wanner, Ed., ed Karlsruhe, Germany: Deutsche Gesellschaft für Materialkunde 2013, pp. 205-211.

T. Ullmann, **Y. Shi**, N. Rahner, M. Schmücker, P. Fey, G. Busse, and S. Becker, "Quality Assurance for the Manufacturing of Oxide Fiber Reinforced Ceramic Composites for Aerospace Applications " in *4th International Symposium on NDT in Aerospace* ed. Augsburg, Germany: Deutsche Gesellschaft für Zerstörungsfreie Prüfung e.V., 2012.

T. Ullmann, **Y. Shi**, and R. Aoki, "Capabilities of Lock-in Thermography for Non-destructive Inspection of Fibre Reinforced Composites," in *11th International Conference on Quantitative InfraRed Thermography*, G. Gardone, Ed., ed. Naples, Italy, 2012.

Y. Shi, K. Tushtev, D. Koch, and K. Rezwan, "Mechanische Charakterisierung und nichtlineare Modellierung anisotroper, kurzfaserverstärkter Keramiken," in *Tagungsband zum 18. Symposium Verbundwerkstoffe und Werkstoffverbunde* B. Wielage, Ed., ed Chemnitz, Germany: Deutsche Gesellschaft für Materialkunde 2011, pp. 178-183.